

# Charge exchange recombination in X-ray spectra of He-like argon measured at the tokamak TEXTOR

Inaugural-Dissertation

zur Erlangung des Doktorgrades  
der Mathematisch-Naturwissenschaftlichen Fakultät  
der Heinrich-Heine-Universität Düsseldorf

vorgelegt von

Tobias Schlummer  
aus Hamm (Westf.)

Düsseldorf, März 2014

aus dem Institut für Laser- und Plasmaphysik  
der Heinrich-Heine Universität Düsseldorf

Ich versichere an Eides Statt, dass die Dissertation von mir selbständig und ohne unzulässige fremde Hilfe unter Beachtung der „Grundsätze zur Sicherung guter wissenschaftlicher Praxis an der Heinrich-Heine-Universität Düsseldorf“ erstellt worden ist.

Tobias Schlummer

Gedruckt mit Genehmigung der  
Mathematisch-Naturwissenschaftlichen Fakultät der  
Heinrich-Heine-Universität Düsseldorf

Referent: Prof. Dr. Detlev Reiter

Korreferent: Prof. Dr. Georg Pretzler

Tag der mündlichen Prüfung: 16.06.2014

# Contents

<b>Zusammenfassung</b>	<b>5</b>
<b>Abstract</b>	<b>7</b>
<b>1 Introduction</b>	<b>9</b>
<b>2 Motivation</b>	<b>12</b>
<b>3 Theoretical Background</b>	<b>14</b>
3.1 Principles of plasma spectroscopy . . . . .	14
3.1.1 Atomic processes in fusion plasmas . . . . .	15
3.1.2 Population densities of ion stages and excited states . . . . .	21
3.1.3 The concept of effective rate coefficients . . . . .	24
3.2 Radial impurity transport . . . . .	26
3.3 X-ray spectroscopy . . . . .	27
3.3.1 The $K_{\alpha}$ -spectrum of He-like argon . . . . .	28
<b>4 Experimental setup</b>	<b>38</b>
4.1 The tokamak TEXTOR . . . . .	38
4.2 The X-ray spectrometers . . . . .	39
4.2.1 Johann-type X-ray spectrometers . . . . .	40
4.2.2 The <b>H</b> igh <b>R</b> esolution X-ray <b>S</b> pectrometer (HRS) . . . . .	41
4.2.3 The compact imaging Bragg spectrometer . . . . .	43
4.2.4 Calibration of the W7-X imaging spectrometer . . . . .	43
<b>5 Charge exchange and impurity transport studies based on radially resolved <math>K_{\alpha}</math>-spectra of He-like argon</b>	<b>49</b>
5.1 Experimental data . . . . .	49
5.2 Data analysis . . . . .	53
5.2.1 Effects of charge exchange and transport on the argon spectrum . . . . .	55
5.2.2 The impurity transport model . . . . .	56
5.2.3 The neutral particle transport model . . . . .	59
5.3 Results . . . . .	59
5.3.1 The radial impurity transport coefficient . . . . .	60
5.3.2 Neutral particle density . . . . .	66
5.3.3 Current limitations of the method . . . . .	66
5.3.4 Evaluation of the absolute line intensities . . . . .	69

5.4	Conclusion . . . . .	70
<b>6</b>	<b>Plasma temperature profiles from X-ray imaging at TEXTOR</b>	<b>73</b>
<b>7</b>	<b>Charge exchange contributions to the Rydberg series of He-like argon</b>	<b>79</b>
7.1	Determination of the argon ion ratio $\text{Ar XVIII}/\text{Ar XVII}$ . . . . .	81
7.2	Charge exchange on the Rydberg states of He-like argon . . . . .	81
<b>8</b>	<b>The effective rate coefficients for charge exchange on the Rydberg series of He-like argon</b>	<b>93</b>
8.1	Hydrogenic approximation of the Rydberg series of He-like argon . . . . .	93
8.2	The collisional radiative model NOMAD . . . . .	94
8.3	Results . . . . .	95
	<b>Conclusions</b>	<b>102</b>
	<b>Danksagung</b>	<b>105</b>

# Zusammenfassung

Der Ladungsaustausch zwischen Ionen und atomarem Wasserstoff ist ein wichtiger Reaktionskanal in magnetisch eingeschlossenen Fusionsplasmen. Einerseits erhöht der Ladungsaustausch die Strahlungsverluste und führt daher zur Abkühlung der Plasmarandschicht. Andererseits verschiebt er als zusätzlicher Rekombinationskanal das Ionisationsgleichgewicht im Plasma hin zu niedrigeren Ionisierungsstufen. Zudem ist das rekombinierende Ion in der Regel in einem hoch angeregten Zustand, der durch spontane Photoemission in den Grundzustand zerfällt. Über die Änderungen des Ionisationsgleichgewichtes und der Besetzungsdichten der angeregten Ionenzustände beeinflusst der Ladungsaustausch die in einem Fusionsplasma gemessenen Spektren.

Zentrales Ziel dieser Arbeit ist die röntgenspektroskopische Untersuchung von Ladungsaustauscheffekten am Tokamak TEXTOR. Unlängst wurde ein für den Stellarator W7-X entwickeltes, bildgebendes Röntgenspektrometer an TEXTOR installiert. Das Spektrometer ist für die Messung des  $K_\alpha$ -Spektrums von He-ähnlichem Argon ( $1s2l - 1s^2$ , ca. 4 Å) optimiert. Die  $K_\alpha$ -Spektroskopie an He-ähnlichen Plasmaverunreinigungen ist als Diagnostik für Elektronen- und Iontemperaturmessungen etabliert. Dennoch sind die beobachteten Intensitätsverhältnisse der  $K_\alpha$ -Linien und der zugehörigen Satelliten bisher nicht vollständig verstanden. Diese zeigen deutliche, zum Plasmarand hin zunehmende Abweichungen von den Vorhersagen des Koronamodells. Als wahrscheinlichste Gründe wurden in der Vergangenheit Verunreinigungstransport und Ladungsaustausch mit dem Neutralteilchenhintergrund diskutiert. Eine exakte Beschreibung der Spektren ist jedoch trotz detaillierter Analysen bisher nicht gelungen.

Zur Beschreibung der an TEXTOR gemessenen Spektren wird die radiale Argonionenverteilung mit einem eindimensionalen Transport-Code berechnet. Das Modell berücksichtigt Ladungsaustauschrekombination und radialen Teilchentransport auf Basis gegebener Profile der Neutralteilchendichte  $n_0(r)$  und des Diffusionskoeffizienten  $D_\perp(r)$ . Aus den erhaltenen Argonionenprofilen werden dann mit Hilfe der entsprechenden Emissionskoeffizienten die theoretischen Spektren produziert. In einer iterativen Prozedur wird dabei unter Anpassung von  $n_0(r)$  und  $D_\perp(r)$  Konsistenz zwischen den experimentellen und den theoretischen Spektren erzielt. Die radial aufgelösten  $K_\alpha$ -Spektren erlauben eine klare Trennung von Ladungsaustausch- und Transporteffekten, so dass die Eindeutigkeit der Lösungen sichergestellt ist. In den meisten Fällen lassen sich die Linienverhältnisse entlang des gesamten radialen Sichtfeldes mit hoher Genauigkeit modellieren, wobei die abgeleiteten  $n_0(r)$  und  $D_\perp(r)$  gut mit Ergebnissen früherer Experimente bzw. Simulationen übereinstimmen. Die vorgelegte Analyse klärt die seit langem offene Frage nach den Mechanismen hinter den experimentell beobachteten  $K_\alpha$ -Linienverhältnissen. Zudem erweitert sie die diagnostischen Möglichkeiten der bildgebenden  $K_\alpha$ -Spektroskopie, sodass nun neben der Elektronen- und Iontemperatur gleichzeitig radiale Profile der

Neutralteilchendichte und des Transportkoeffizienten bestimmt werden können. Zusätzlich werden die aus den  $K_\alpha$ -Spektren gewonnenen radialen Profile der Elektronen- und Ionentemperatur diskutiert und mit Ergebnissen anderer Diagnostiken verglichen.

Der Ladungsaustausch ist nicht nur in Bezug auf den thermischen Neutralteilchenhintergrund relevant. Er spielt zudem eine Schlüsselrolle in der aktiven Ladungsaustauschspektroskopie (CXRS). Neben der Messung von Ionentemperaturen ist eine Hauptanwendung der CXRS die Bestimmung absoluter Dichten von Verunreinigungen im Plasma. Für Dichtemessungen mittels CXRS sind die partiellen Wirkungsquerschnitte für den Ladungsaustausch von großer Bedeutung. Diese wurden jedoch bisher nicht experimentell überprüft. Dies gilt insbesondere für den Ladungsaustausch auf hoch ionisierte Verunreinigungen bei hohen Kollisionsenergien. Gleichzeitig zeigen die verfügbaren theoretischen Datensätze erhebliche Diskrepanzen.

In dieser Arbeit werden die einzigartigen diagnostischen Möglichkeiten an TEXTOR genutzt, um die Rydberg-Serie von He-ähnlichem Argon ( $1snp - 1s^2$ , ca. 3 Å) unter direktem Einfluss eines Neutralteilchenheizstrahls (50 keV) zu messen. Die durch die Strahlteilchen verursachten charakteristischen Linienerhöhungen stimmen gut mit den Vorhersagen einer der theoretischen Datensätze überein. Sowohl die Abhängigkeit von der Hauptquantenzahl  $n$  als auch die absoluten Werte können bestätigt werden. Die Experimente liefern die erste experimentelle Verifizierung der Querschnitte für Ladungsaustausch bei CXRS-relevanten Energien.

# Abstract

Charge exchange recombination between ions and atomic hydrogen is an important atomic process in magnetically confined fusion plasmas. Besides radiative cooling of the plasma edge, charge exchange causes modifications of the ionization balance and the population densities of excited ion states.

The central goal of this work is to investigate the influence of charge exchange on X-ray spectra measured at the tokamak TEXTOR. A new 2D X-ray spectrometer developed for future use at the stellarator W7-X was recently installed at TEXTOR. The spectrometer is optimized for measuring the  $K_\alpha$ -spectrum of He-like argon ( $1s2l - 1s^2$ ) at wavelengths close to 4 Å.  $K_\alpha$ -spectroscopy on He-like impurity ions is an established diagnostic for electron and ion temperature measurements in fusion plasmas. Still, up to now the observed intensity ratios of the  $K_\alpha$ -lines and their associated satellites are not fully understood. They show significant deviations from the predictions made by basic corona models. In the past charge exchange with the neutral particle background and radial impurity transport have been discussed as likely explanations. Yet a detailed description of the experimental spectra still has not been achieved.

To reconstruct the 2D  $K_\alpha$ -spectra measured at TEXTOR the radial argon ion distribution is modeled using an impurity transport code. The model accounts for charge exchange and transport on basis of given radial profiles of the neutral particle density  $n_0(r)$  and the diffusion coefficient  $D_\perp(r)$ . The theoretical spectrum is then constructed based on the processes relevant for line emission. Within an iterative procedure  $n_0(r)$  and  $D_\perp(r)$  are varied until consistency between the theoretical and the experimental spectra is achieved. It is shown that the 2D  $K_\alpha$ -spectra allow a clear distinction of charge exchange and transport effects, ensuring unique solutions for  $n_0(r)$  and  $D_\perp(r)$ . In most cases the spectra can be reconstructed with high accuracy along the entire radial field of view. The deduced  $D_\perp(r)$  and  $n_0(r)$  are in good agreement with earlier experimental and modeling results. The presented analysis not only resolves the long-standing issues concerning the intensity ratios in the  $K_\alpha$ -spectra of He-like ions. It also introduces imaging  $K_\alpha$ -spectroscopy as suitable diagnostic for the neutral particle density and the impurity transport behavior in fusion plasmas. Additionally, the radial profiles of the electron and the ion temperature obtained from the  $K_\alpha$ -spectra are presented and compared to results from other diagnostics.

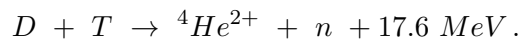
Charge exchange is not only relevant in regard to the thermal background neutrals. It also plays a key role in charge exchange recombination spectroscopy (CXRS). For impurity density measurements based on CXRS the accuracy of the charge exchange cross sections are of crucial importance. However, so far no experimental verification of the fine-structure resolved cross sections for charge exchange on highly ionized impurity ions

has been performed, whereat the available theoretical data sets show significant deviations.

In this work the unique diagnostic opportunities at TEXTOR are used to measure the Rydberg series of He-like argon ( $1snp - 1s^2$ , ca.  $3 \text{ \AA}$ ) under direct influence of a neutral particle heating beam ( $50 \text{ keV}$ ). The characteristic line enhancement caused by the beam particles is consistent with one set of the theoretical charge exchange cross sections. Both, the absolute values as well as the dependence on the principle and the orbital quantum numbers can be confirmed. The results represent the first experimental verification of the fine-structure resolved cross sections for charge exchange at CXRS relevant collision energies and give confidence in the quality of the theoretical data.

# 1 Introduction

Controlled nuclear fusion is a promising future alternative to fossil energy sources and nuclear fission. Similar to the basic heating mechanism of stars, in a fusion reactor the hydrogen isotopes deuterium and tritium are fused to helium:



The products of this, known as the DT reaction, include a helium nucleus and a neutron. Additionally a total kinetic energy of 17.6 *MeV* is released, of which about 80% is carried by the neutron. By converting this kinetic energy into heat, nuclear fusion devices can be integrated into conventional power plant concepts.

Though also based on nuclear energy, fusion power plants offer several advantages compared to fission power plants. As the DT reaction is not a chain reaction, an equivalent to the core meltdown in fission reactors is not possible. Furthermore, the DT reaction does not produce any long-lived radioactive products. The unstable tritium does not naturally exist on earth. Therefore, it is transiently bred from lithium. As a consequence, the fuels for nuclear fusion - deuterium and lithium - are abundantly available on earth, unlike the fossil combustibles coal, oil and gas, or uranium for nuclear fission. DT reaction rates sufficient for an economic operation of a fusion reactor are only achieved at very high temperatures of several keV, at which the fuel gas is in the plasma state. To create the necessary plasma conditions, two different concepts of plasma confinement are applied. In inertial confinement, solid fuel pellets are heated by intense laser pulses. These cause shock waves that compress the fuel, so that for a short time a confined plasma state is achieved. In magnetic confinement the plasma particles are guided by magnetic field lines that keep them from touching the surrounding vessel wall.

**The tokamak** The tokamak<sup>1</sup> is the most well-established magnetic confinement concept. A tokamak consists of a toroidal plasma chamber that is surrounded by a set of poloidal magnetic field coils. The field coils induce a strong, toroidal magnetic field that forces the charged plasma particles into narrow helical orbits along the field lines. To compensate for plasma drifts due to the toroidal curvature of the field lines, a toroidal plasma current is induced that creates an additional poloidal magnetic field. The plasma current is induced with the help of a transformer that utilizes the toroidally shaped plasma as its secondary winding. The superposed toroidal and poloidal magnetic fields form helical field lines (figure 1.1(a)). These form nested flux surfaces of constant plasma pressure (figure 1.1(b)). Due to the high particle mobility along the field lines the plasma parameters are approximately constant within one flux surface. The plasma current drive

---

<sup>1</sup>Russ.: toroidalnaya kamera s magnitnymi katushkami, (toroidal chamber with magnetic coils)

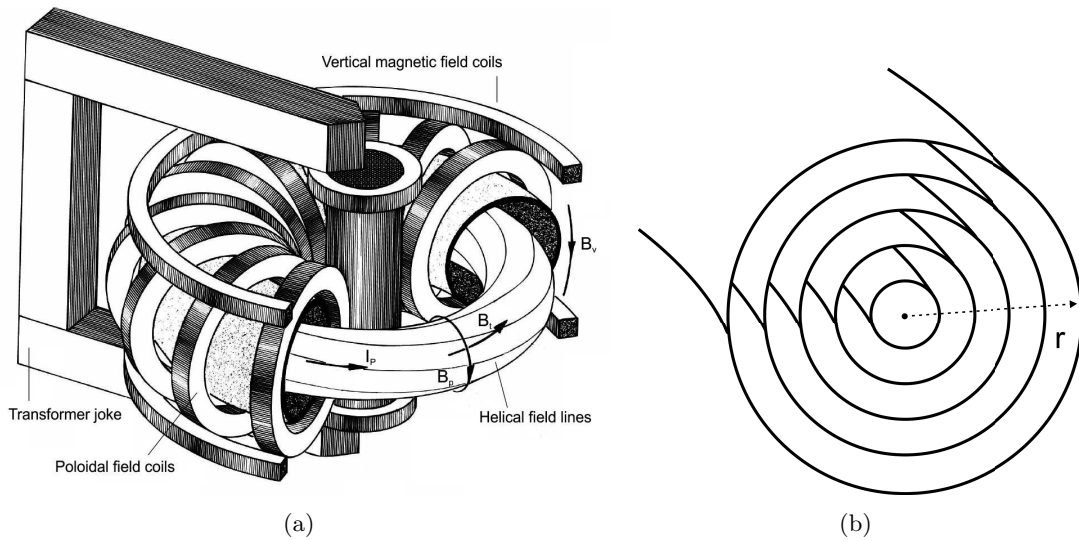


Figure 1.1: **a)** Principles of a tokamak (rearranged from [1]). **b)** Nested magnetic flux surfaces without Shafranov shift (compare [2] p.108).

not only contributes to the confinement, but also acts as an ohmic heating mechanism. Yet the plasma temperatures accessible via ohmic heating are limited. To achieve higher temperatures external heating techniques can be applied. Additional energy is then fed into the plasma by injecting high energy neutral particles or with the help of electromagnetic waves.

**Plasma-wall interaction** A critical issue for magnetic fusion devices is the interaction of the plasma with the vessel walls. On the one hand the first wall elements have to withstand very high particle and heat loads for long time periods. Therefore, the wall materials have to meet high requirements in regard to durability. On the other hand the erosion of the wall surface always leads to a contamination of the plasma with the wall material. These 'intrinsic' impurities have higher core charges than the main plasma ions (usually hydrogen) and therefore degrade the energy confinement by increasing the radiation losses. In this context the search for feasible wall materials is a key issue on the way to economic fusion reactors.

Another important consequence of plasma-wall interaction is the creation of atomic or molecular hydrogen due to recombination at the wall surface or retention and recycling processes. The neutral particles are not affected by the magnetic field and can penetrate deeply into the plasma, where they cause radiation cooling by charge exchange reactions with the plasma ions. Charge exchange with the neutral particle background also influences the spectral emission from the plasma ions, as will be discussed in this thesis.

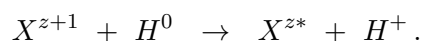
**Plasma spectroscopy** Detailed knowledge about the confined plasma is of crucial importance for safe and efficient operation of a tokamak. Therefore, various diagnostic

tools have been developed that enable determination of a variety of plasma parameters. Many of the diagnostic methods are based on different kinds of plasma spectroscopy, performed on a wide range of frequencies ranging from the infra-red through the visible and VUV to the X-ray region. Spectroscopic measurements can involve emissions from the main plasma ions or from heavier impurity elements.

The field of plasma spectroscopy can be divided into active and passive techniques. In active spectroscopy the desired line radiation is specifically initiated from outside using particle or laser beams. The variable intersection of the spectrometer's line of sight and the beam line allows for spatially resolved measurements. In passive methods, the spectral information is always integrated along the entire plasma cross section and must be interpreted with respect to the emission profiles or with the help of tomographic techniques.

## 2 Motivation

The neutral particle background in controlled fusion plasmas is not only relevant for the energy confinement. It can also significantly affect spectroscopic measurements via charge exchange collisions with the plasma ions. The process of charge exchange recombination (CX) describes the transfer of a bound electron from an atom to an ion. In case of a hydrogen atom and an ion  $X$  in the charge state  $z + 1$ , the reaction equation is as follows:



For one thing, charge exchange represents an additional recombination channel for ions and therefore affects the ionization balance in the plasma. Also, the recombining ion  $X^z$  is preferably highly excited, which can have a significant influence on the population densities of the excited ion states. Both effects are important for the interpretation of the spectral emission from the ion species  $X^z$ .

The central goal of this work is to study the process of charge exchange recombination with the help of X-ray spectroscopy. A new imaging X-ray spectrometer at the TEXTOR tokamak allows measurement of the  $K_\alpha$ -emission of He-like argon ( $1snp - 1s^2$ ) including the associated satellite spectrum in spatial resolution. The  $K_\alpha$ -spectra of He-like mid  $z$  impurity ions (e.g. argon, iron, titanium) are widely used in plasma temperature diagnostics. However, the line ratios observed within the  $K_\alpha$ -spectrum cannot be described within the corona model and are still not fully understood today. In order to resolve the issues regarding the observed  $K_\alpha$ -line ratios, a quantitative study of the influence of charge exchange with thermal background neutrals and impurity transport is performed on basis of the radially resolved spectral data measured at TEXTOR. At the same time, the analysis aims to contribute to resolving a long-standing controversy concerning the impurity transport behavior in TEXTOR.

Charge exchange is not only relevant with respect to the neutral particle background. It is furthermore of primary importance in active, beam-induced spectroscopy (charge exchange recombination spectroscopy, CXRS). In CXRS fast hydrogen atoms (ca. 20 – 100 keV) are injected into the plasma to populate highly excited states of impurity ions via charge exchange. The consecutive line emission is then used for ion temperature measurements, but also to determine the absolute densities of the emitting impurity elements. The line intensity corresponding to a transition in the impurity ion  $X^z$  induced by charge exchange is given by:

$$I_{cx} = Q_{cx} \cdot n_b \cdot X^{z+1} \cdot \hbar\omega,$$

where  $n_b$  is the density of hydrogen atoms provided by the neutral particle injectors. The effective rate coefficient for charge exchange  $Q_{cx}$  is a measure for the number of photons emitted per  $n_b$  and  $X^{z+1}$  and therefore is important for absolute density measurements. It crucially depends on the fine-structure resolved cross sections for charge exchange. However, the two sets of theoretical CX cross sections available disagree significantly in absolute values as well as in the dependence on the orbital quantum number.

This work aims to provide a first experimental verification of the fine-structure resolved cross sections for charge exchange on H-like argon at CXRS-relevant energies. For this purpose the Rydberg series of He-like argon is measured under the direct influence of a neutral particle heating beam (50 keV). The observed contributions to the Rydberg lines then allow attribution of the relevant partial charge exchange cross sections. This will contribute to assessing the quality of the theoretical atomic data for charge exchange and with this the reliability of absolute density measurements based on CXRS.

# 3 Theoretical Background

## 3.1 Principles of plasma spectroscopy

In this section the theoretical principles of plasma spectroscopy are discussed. The presentation is inspired by [3–5].

As any plasma, controlled fusion plasmas emit electromagnetic radiation over a wide spectral range, depending on the composition, temperature and density. One distinguishes between continuous radiation, continuous radiation with edges and line radiation. These three types of radiation correspond to free-free, free-bound and bound-bound electron transitions, respectively. Free-free transitions include all kinds of acceleration of charged particles, which are always accompanied by the emission of bremsstrahlung. The bound-free transitions are non resonant recombination processes, leading from a free state of arbitrary energy to a certain bound state. Finally, the bound-bound transitions between two energy states of an ion system lead to characteristic line emission. (compare [3] p.86) For the spectroscopic purposes discussed in this thesis, only the discrete line emission due to bound-bound transitions is of interest and will be considered in more detail.

An excited ion will always return into its ground state via radiative decay. This can happen directly or in intermediate steps (cascades). Consider a radiative transition  $i \rightarrow j$  between two quantum states  $i$  and  $j$  of an ion, which have the energies  $E_i$  and  $E_j$  ( $E_i > E_j$ ). The energy of the photon emitted during the transition is  $\Delta E_{ij} = E_i - E_j$ . The corresponding spectral line is observed at the frequency  $\omega_{ij} = \Delta E_{ij}/\hbar$ . Its intensity  $I_{ij}$  is given by:

$$I_{ij} = N_i \cdot A_{ij} \cdot \hbar \omega_{ij}, \quad (3.1)$$

where  $N_i$  is the population density of the upper state  $i$  and  $A_{ij}$  is the transition probability or Einstein coefficient. From equation 3.1 is clear that a discrete spectrum mirrors the population densities of the excited states of the emitting ions. Understanding spectral line intensities therefore means understanding the atomic processes leading to the population of excited ion states.

The Einstein coefficient  $A_{ij}$  depends on the core charge  $z$  and the quantum numbers of initial and final state. The highest transition probabilities are found for dipole transitions with  $\Delta L_{ij} = \pm 1$  and  $\Delta S_{ij} = 0$  (dipole selection rule), where  $L$  and  $S$  are the orbital and the spin quantum numbers, respectively. The lifetime  $\tau_i$  of the of the excited state  $i$  follows from the total transition probability  $A_i = \sum_{j < i} A_{ij}$ . It is defined as  $\tau_i = A_i^{-1}$ . The  $A_i$  can be estimated by the following scaling law ([6], p.146):

$$A_i \approx 1.6 \cdot 10^{10} \cdot z^4 \cdot n_i^{-\frac{9}{2}} [s^{-1}], \quad (3.2)$$

where  $n_i$  is the principle quantum number of the state  $i$ .

### 3.1.1 Atomic processes in fusion plasmas

In a plasma environment several atomic processes lead to ion excitation or redistribution of excited ion states. In addition to the above-mentioned radiative decay, these include several kinds of recombination, ionization and de-/excitation processes.

The rate of any collisional atomic process between target ion  $z$  and projectile particle  $p$  that transfers  $z$  from state  $i$  into state  $j$  is given by:

$$R_{ij} = -\left. \frac{dN_{z,i}}{dt} \right|_{ij} = \sigma_{ij}(v) \cdot v \cdot N_{z,i} \cdot N_p, \quad (3.3)$$

where  $N_p$  and  $N_{z,i}$  are the densities of the projectile particles and the target particles in state  $i$ , respectively, while the total density of the ion species  $z$  is defined as  $N_z = \sum_i N_{z-i}$ . Furthermore,  $v = |\vec{v}_p - \vec{v}_z|$  is the relative particle velocity and  $\sigma_{ij}(v)$  is the cross section giving the reaction probability for the particular process. In case of non-monoenergetic particles, equation 3.3 needs to be convoluted with the velocity distributions of the target and the projectile species  $f_z(\vec{v}_z)$  and  $f_p(\vec{v}_p)$ , respectively:

$$\begin{aligned} R_{ij} &= -\left. \frac{dN_{z,i}}{dt} \right|_{ij} \\ &= N_p \cdot N_{z,i} \cdot \int_{\vec{v}_z} \int_{\vec{v}_p} \sigma_{ij}(v) \cdot v \cdot f_z(\vec{v}_z) \cdot f_p(\vec{v}_p) \cdot d^3\vec{v}_z \cdot d^3\vec{v}_p \\ &= N_p \cdot N_{z,i} \cdot \langle \sigma_{ij} \cdot v \rangle. \end{aligned} \quad (3.4)$$

The double integral is combined to the rate coefficient  $\langle \sigma_{ij} \cdot v \rangle$ . The velocity distribution functions  $f(\vec{v})$  of plasma particles usually are given by the Maxwell distribution. (compare [3] p.115) However, in case of fast monoenergetic particles  $p$  where  $v_p \gg v_z$  the rate coefficient can be approximated by  $\langle \sigma_{ij} \cdot v \rangle \approx \sigma_{ij} \cdot v_p$ .

For each atomic process, there is an inverse process. The cross sections or rates of direct and reverse process are related by the principle of detailed balance. It requires that in thermodynamic equilibrium the rates of direct and reverse reactions are equal:

$$\begin{aligned} R_{ij} &= R_{ji} \\ \langle \sigma_{ij} \cdot v \rangle \cdot N_i &= \langle \sigma_{ji} \cdot v \rangle \cdot N_j \\ \langle \sigma_{ij} \cdot v \rangle \cdot g_i \cdot e^{-E_i/T_e} &= \langle \sigma_{ji} \cdot v \rangle \cdot g_j \cdot e^{-E_j/T_e} \\ \Leftrightarrow \langle \sigma_{ij} \cdot v \rangle &= \frac{g_j}{g_i} \cdot e^{-\Delta E_{ij}/T_e} \cdot \langle \sigma_{ji} \cdot v \rangle. \end{aligned} \quad (3.5)$$

Here the states  $i$  and  $j$  are assumed to be populated according to the Boltzmann distribution (see equation 3.20).

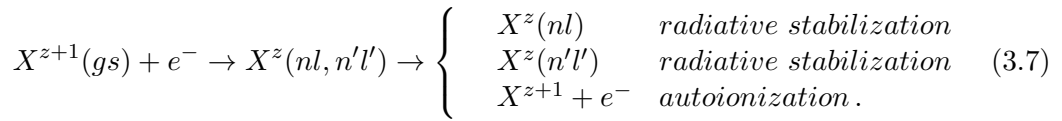
The inverse process of radiative decay is called photon absorption. However, in optically thin plasmas photo-induced processes are negligible due to the high photon loss rates. The following pages introduce the atomic processes most relevant for spectroscopy on magnetically confined fusion plasmas.

**Radiative recombination**  $\leftrightarrow$  **photoionization** An unbound electron can recombine with an ion  $X$  of charge  $z + 1$  via radiative recombination ( $rr$ ):



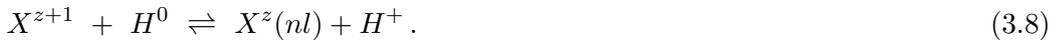
Here the emitted photon carries the exceeding energy of the recombining electron. The cross sections for radiative recombination depend on the ion charge as well as on the principle quantum number  $n$  and the angular momentum quantum number  $l$ . The inverse process is called photoionization, which in optically thin fusion plasmas is negligible.

**Dielectronic recombination**  $\leftrightarrow$  **autoionization** In dielectronic recombination ( $dr$ ) the exceeding energy of the recombining electron is transferred to an already bound electron. Dielectronic recombination is a resonant process resulting in a doubly excited state:



Once the doubly excited state is formed, the ion can stabilize itself by radiative decay into a singly excited state. Alternatively, it can disintegrate by autoionization - the reversed process. Dielectronic recombination with consecutive autoionization leads to resonances in the excitation cross sections [7]. Dielectronic recombination followed by radiative decay plays an important role in the emission of so-called satellite lines [8]. Satellites are transitions from doubly excited states into the ground state or a singly excited state. Their wavelengths are always close to those of ground state transitions in the adjacent, higher ionization stage. In this respect the latter are also called parent lines, as they usually are much brighter. Further details are discussed in section 3.3.1.

**Charge exchange recombination** The focus of this work is the process of charge exchange recombination ( $cx$ ). It describes ion-atom collisions that result in an electron transfer from the projectile atom to the target ion. Within the context of charge exchange, the colliding particles are also referred to as donor atom and acceptor ion. Although charge exchange takes place between many different collision partners, in fusion plasmas only the charge transfer from neutral hydrogen to the main plasma ions or to highly ionized impurity elements is relevant:



For charge exchange on highly ionized argon at high collision energies, two sets of fine-structure resolved cross sections exist to date - one provided by Schultz et al. [9, 10] and one provided by Errea et al. [11]. Both are based on Classical Trajectory Monte Carlo (CTMC) calculations. Figure 3.1(a) compares the total cross sections as function of the collision energy. For low energies the two sets disagree by almost a factor of two, but converge towards higher energies. With respect to the  $l$ -dependencies the deviations are even stronger, as shown in figure 3.1(b). In this work the data sets from Schultz

et al. are used, since they are freely available. Charge exchange at thermal energies is considered on basis of the cross sections from Janev [12].

Charge exchange preferably populates excited states of the recombining ion. Figure 3.2 illustrates the fine-structure resolved cross sections for charge exchange from atomic hydrogen on fully ionized argon at a collision energy of  $35 \text{ keV}$ . The data is plotted for  $H(1s)$  (figure 3.2(a)) as well as for  $H(2s)$  excited donor atoms (figure 3.2(b)). The cross sections show a strong dependence on the principle and orbital quantum numbers ( $nl$ ) of the populated level. On the one hand, high  $l$ -states are strongly preferred. With respect to the principle quantum number  $n$ , a resonance occurs. This resonance can be understood qualitatively from a simple consideration (compare [5] p.76). As the two ion core potentials approach during the collision, the coulomb barrier between them decreases. As a consequence, a certain probability exists for the electron to tunnel from the donor into the acceptor potential. In this picture the charge exchange cross sections become resonant, when the coulomb barrier falls below the energy of the bound electron. The energy  $E_{cx}$  of the final state, for which the resonance occurs is given by ([5] p.76):

$$E_{cx} = I_D + \frac{z}{R_{cb}} \quad \text{with} \quad R_{cb} = \frac{2 \cdot \sqrt{z+1} + 1}{I_D}, \quad (3.9)$$

where  $z+1$  is the charge of the capturing ion,  $I_D$  is the ionization potential of the donor atom and  $R_{cb}$  is the inter nuclear distance. All quantities are in atomic units. In case of charge exchange between ground state hydrogen ( $H(1s)$ ) and fully ionized argon ( $z=18$ ), equation 3.9 gives  $E_{cx} = 38 \text{ eV}$  corresponding to a resonance at  $n_{cx} \approx 10$ . This is in good agreement with figure 3.2(a). For charge exchange from  $H(2s)$ , the scaling law gives  $E_{cx} = 9.5 \text{ eV}$  or  $n_{cx} \approx 21$ , which is confirmed by figure 3.2(b). Finally, figure 3.3 shows the energy dependence of the  $n$ -resolved charge exchange cross sections from Schultz. It is clearly visible that the resonance described by equation 3.9 smears out towards higher  $n$  quantum numbers when the collision energy increases.

In the classical treatment of the charge exchange process, the spin of the transferred electron is not considered, so that the resulting cross sections are not spin sensitive. The  $\sigma_{cx}(nl)$  are therefore statistical in  $j$  according to  $g_j = 2 \cdot j + 1$ .

**De-/excitation by electron collisions** In hot fusion plasmas, collisional excitation (*exc*) from the ground state can generally be considered as the most important source for the population of excited ion states. Moreover, at high plasma densities, collisional de-/excitation processes redistribute the population densities of excited ion states according to their statistical weights (see section 3.1.2). In case of electron collisions the reaction equation is given by:



As any other many-body problem, this system cannot be described exactly, so that approximations need to be applied for calculating the cross sections. In the Born approximation the system is simplified by describing the free electron as a plain wave. Among the more sophisticated methods is the distorted wave approximation. Here the

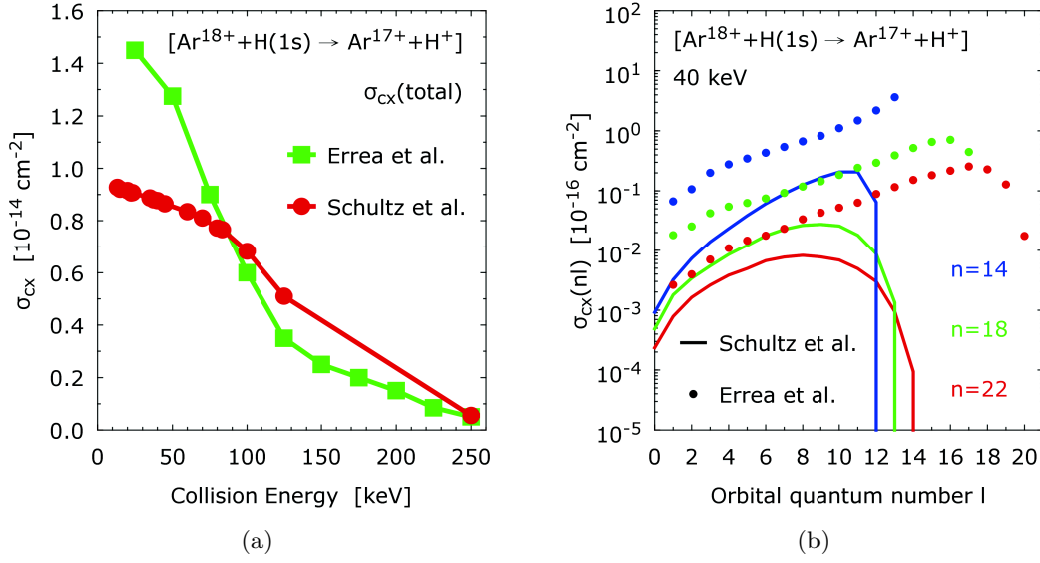


Figure 3.1: Comparison of CX-cross section data from Schultz et al. [9, 10] and from Errea et al. (rearranged from [11]). **a)** Total cross sections as a function of the collision energy. **b)** Fine structure resolved cross sections for  $E = 40 \text{ keV}$  from Schultz et al. (lines) and from Errea et al. (points).

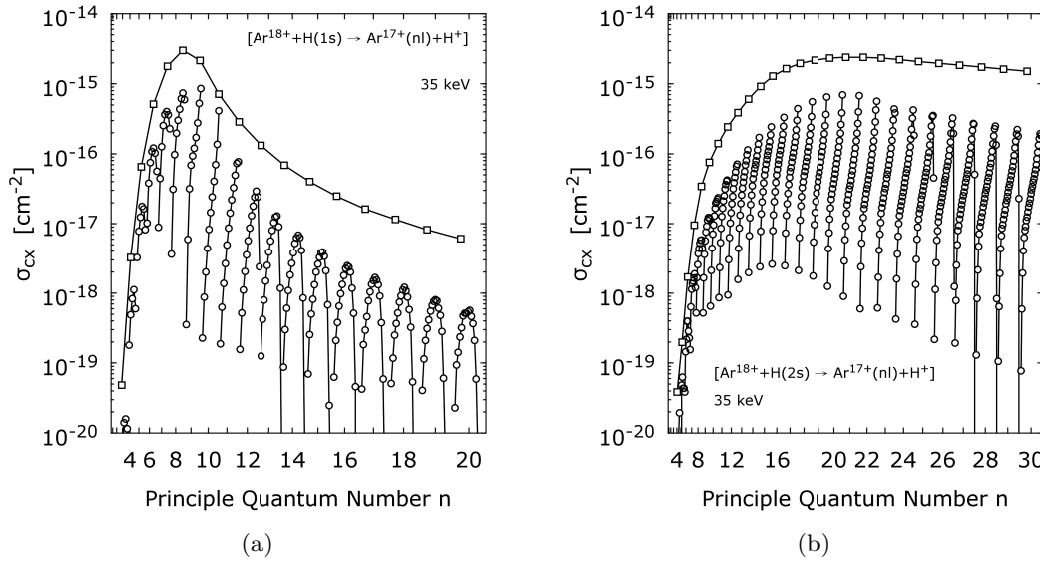


Figure 3.2: Fine structure resolved cross sections for charge exchange recombination on fully ionized argon from  $H(1s)$  **(a)** and  $H(2s)$  **(b)** donor atoms at a collision energy of  $E_b = 35 \text{ keV}$  (Schultz et al. [9, 10]).

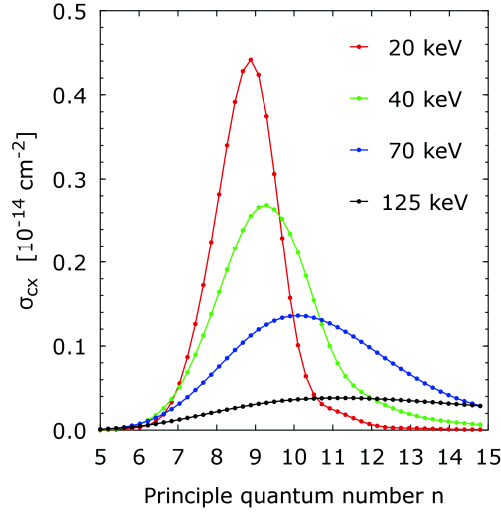


Figure 3.3: Energy dependence of the  $n$ -resolved cross sections for charge exchange from  $H(1s)$  on fully ionized argon (Schultz et al. [9, 10]).

incident and the scattered electron are described by individual wave functions. The close-coupling approximation resolves individual bound electrons and takes into account their scattering potentials. Atomic codes like FAC [13] or AUTOSTRUCTURE [14] are based on the distorted wave approximation.

A widely used semi-empirical formula for the excitation cross sections was given by van Regemorter [15]:

$$\sigma_{ij}(u) = \frac{8}{\sqrt{3}} \cdot \pi^2 a_0^2 \cdot \left( \frac{\Delta E_{ij}}{E_R} \right)^{-2} \cdot f_{ij} \cdot \frac{\bar{G}(u)}{u} \quad \text{with} \quad u = \frac{E}{\Delta E_{ij}}, \quad (3.11)$$

where  $E_R$  is the Rydberg energy ( $E_R = 13.6 \text{ eV}$ ),  $a_0$  is the Bohr radius and  $f_{ij}$  is the oscillator strength. Equation 3.11 is only valid for dipole transitions. The so-called effective Gaunt factor  $\bar{G}(u)$  can take the following values [4, 16]:

$$\bar{G}(u) = \begin{cases} \frac{\sqrt{3}}{2\pi} \cdot \ln(1+u) & \text{for } \Delta n \neq 0 \\ \left(1 - \frac{1}{z}\right) \cdot \left(0.7 + \frac{1}{n}\right) \cdot (0.6 + 0.25 \cdot \ln u) & \text{for } \Delta n = 0. \end{cases} \quad (3.12)$$

Finally, it shall be mentioned that excitation of inner shell electrons leads to doubly excited states and is therefore relevant for the emission of satellite lines (see section 3.3.1).

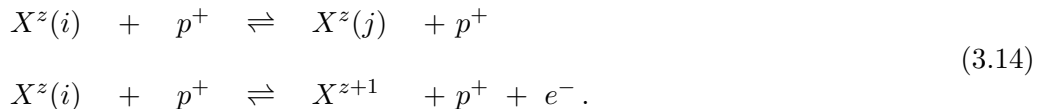
**Ionization by electron collisions  $\leftrightarrow$  three body recombination** When the energy transferred in electron collisions exceeds the ionization potential  $E_i$ , the target ion is ionized:



Although the principles of ionization (*ion*) are the same as those of excitation, the calculation of the cross sections is more complicated due to the two continuum electrons in the ionized system. The cross sections for collisional ionization increase with the principle quantum number  $n$  of the initial level  $X_z(nl)$ , but are insensitive to the angular momentum quantum number  $l$ .

The inverse process of electron ionization is called three body recombination. Here the exceeding energy of the recombining electron is transferred to another free electron. Therefore, the primary process of three body recombination is radiationless. It follows from the principle of detailed balance that three body recombination preferentially populates highly excited states. However, as the reaction rate scales with  $n_e^2$ , three body recombination is of minor importance at typical fusion plasma densities. Yet it can become relevant at higher densities and low temperatures as e.g. in the divertor region of a tokamak.

**Ion-ion-collisions** De-/excitation and ionization of ions can also occur in ion-ion-collisions. In this respect, one usually only considers collisions with the main plasma ions. For an ion  $X^z$  in a hydrogen plasma these collisions are described by:



Due to the mass ratio of  $m_e : m_{ion} \leq 1 : 1800$  the transferred energy during ion-ion collisions is generally lower than during electron-ion collisions, where the mass ratio  $m_e : m_e = 1 : 1$ . The relevance of electron or ion induced processes depends on the plasma temperature and the threshold energies. At collision energies of  $1 - 2 \text{ keV}$ , corresponding to the plasma temperatures in TEXTOR, the ionization of hydrogen is dominated by electron collisions. For the excitation of hydrogen atoms, both electron and ion collisions have to be considered. However, at energies of  $10 - 100 \text{ keV}$  ionization and excitation of hydrogen atoms are mainly induced by ion collisions<sup>1</sup>. Such high particle energies are for example produced by neutral particle injectors (see section 4.1). Yet also future tokamak reactors are planned to operate at plasma temperatures of  $10 \text{ keV}$  and higher. The above considerations are based on cross section data from Janev and Smith [17]. For highly charged mid  $z$  plasma impurities like argon, the picture is different. Here ionization by the main plasma ions is not relevant at all. With respect to excitation processes it has to be distinguished between  $\Delta n = 0$  and  $\Delta n \neq 0$  transitions. In case of  $\Delta n = 0$ , ion collisions are most important, while  $\Delta n \neq 0$  transitions are mainly induced by electrons.

The inverse process of ionization by ion collisions is three body recombination with an electron and a proton. As in case of normal three body recombination, the process is negligible at fusion relevant densities.

---

<sup>1</sup>For the ionization of fast neutrals, also charge exchange with the main plasma ions plays an important role.

### 3.1.2 Population densities of ion stages and excited states

The abundance of ion stages and the population of their excited states can be described in two different approximations. The corona or low density approximation applies for low plasma densities. The concept of local thermodynamic equilibrium (LTE) on the other hand describes the situation at high plasma densities. Both approximations allow significant simplifications and reduction of complexity of any modeled ion system. However, in magnetic fusion devices the plasma densities mostly lie in between the validity ranges of the two limits. In these cases neither of the approximations apply and detailed calculations are necessary to determine the population distributions.

#### Low density limit

In low density limit, the abundance of the ion stages of a given element is determined by the equilibrium of all ionization and recombination processes discussed in section 3.1.1, except charge exchange ([3], p.144):

$$\frac{N_z}{N_{z+1}} = \frac{\langle \sigma_{rr} \cdot v \rangle + \langle \sigma_{dr} \cdot v \rangle}{\langle \sigma_{ion} \cdot v \rangle}, \quad (3.15)$$

where  $N_z$  and  $N_{z+1}$  are the densities of the ion stages  $z$  and  $z+1$ , respectively. The term corona refers to the conditions of the solar corona, that are characterized by a very low density. All rate coefficients are functions of the electron temperature  $T_e$ . Therefore, the ionization balance of a given element is a sole function of  $T_e$ . Figure 3.4(a) shows the coronal ion balance of argon for a fusion relevant temperature range. The Ne-like ( $Ar\ IX$ ) and the He-like ( $Ar\ XVII$ ) stages both represent stable noble gas configurations and are predominant within broad  $T_e$ -intervals. In a tokamak, the coronal ion distribution is a function of the minor radius  $r$ , determined by the radial temperature profile  $T_e(r)$ . Figure 3.4(b) illustrates the argon ion balance for a typical  $T_e$ -profile in TEXTOR.

In corona limit, the population density of an excited state ( $i$ ) relative to the ground state ( $gs$ ) is determined by the rate of the populating processes and the lifetime  $\tau_i = 1/A_i$ . If excitation from the ground state is the dominating source, the corona equilibrium is given by:

$$\frac{N_{z,i}}{N_{z,gs}} = \frac{n_e \cdot \langle \sigma_{exc} \cdot v \rangle}{A_i}. \quad (3.16)$$

Here  $N_{z,i}$  and  $N_{z,gs}$  are the population densities of the state  $i$  and the ground state, respectively. Please note that equation 3.16 neglects cascade contributions from higher energy levels. In corona limit, the population density of the excited states is obviously proportional to the electron density. Equation 3.16 can readily be extended by the rates of additional populating processes like charge exchange recombination.

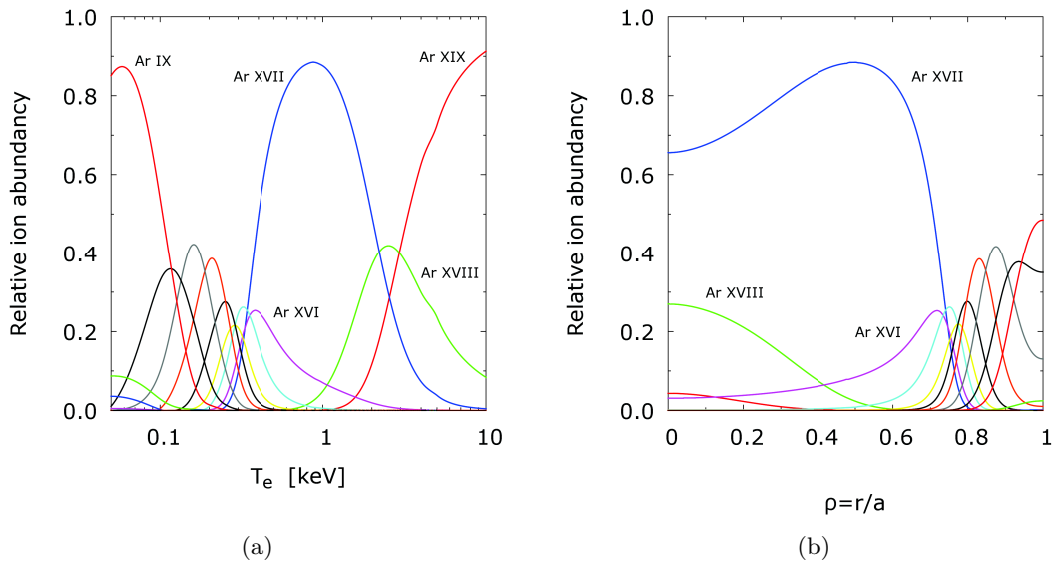


Figure 3.4: **a)** Corona distribution of the argon ion stages as a function of the electron temperature  $T_e$ . The ion stages are labeled in spectroscopic notation. **b)** Corona distribution of the argon ion stages as a function of the minor radius of the tokamak TEXTOR calculated for a typical  $T_e$ -profile with a central temperature of  $1.65 \text{ keV}$ . The minor radius of TEXTOR is  $a = 47 \text{ cm}$ .

### High density limit

A plasma and its radiation field is in thermodynamic equilibrium (TE), when the following conditions are met. The radiation field of the plasma is given by Planck's law:

$$I_\lambda(\lambda, T) \cdot d\lambda = \frac{2 \cdot h \cdot c^2}{\lambda^5} \cdot \frac{1}{e^{hc/T} - 1} [W \cdot m^{-2} \cdot sr^{-1}], \quad (3.17)$$

where  $\lambda$  is the wavelength,  $c$  is the speed of light. With respect to the plasma particles, the kinetic energy is distributed according to Maxwell:

$$f(E)dE = 2 \cdot \sqrt{\frac{E}{\pi}} \cdot T^{-3/2} \cdot e^{-E/T} dE. \quad (3.18)$$

Furthermore, the ion balance of a given element is described by the Saha equation:

$$\frac{N_{z+1}}{N_z} \cdot n_e = 2 \left( \frac{m \cdot T_e}{2\pi\hbar^2} \right)^{\frac{3}{2}} \cdot \frac{g_{z+1}}{g_z} \cdot e^{-I_z/T_e}, \quad (3.19)$$

where  $I_z$  is the ionization energy of the ion stage  $z$ . The excited states of an ion  $z$  are populated according to the Boltzmann distribution:

$$\frac{N_{z,i}}{N_{z,j}} = \frac{g_{z,i}}{g_{z,j}} \cdot e^{-\Delta E_{ij}/T_e}, \quad (3.20)$$

where  $g_{z,i}$  and  $g_{z,j}$  are the statistical weights of the states  $i$  and  $j$ . Finally, each atomic process is in balance with its inverse process (principle of detailed balance, see equation 3.5). (compare [3] p.136)

However, in fusion plasmas full thermodynamic equilibrium is never reached. Although the Maxwell distribution in most cases is well fulfilled, the principle of detailed balance is not. In optically thin plasmas, where photons readily escape the plasma volume, radiative decay is never balanced by photon absorption. Anyway, at sufficiently high plasma densities the rates of the pairwise balanced collisional processes will exceed those of unbalanced spontaneous radiative decay, so that equations 3.20 and 3.19 are still valid. This situation is defined as local thermodynamic equilibrium (LTE). The LTE conditions are not the same for all plasma ion species and excited states and therefore are usually not fulfilled in all cases. This is because all rate coefficients  $\langle \sigma \cdot v \rangle$  and radiative transition probabilities  $A_{ij}$  depend on the ion charge and the quantum numbers  $n$ ,  $l$  and  $j$  of the considered energy states. With increasing plasma density, LTE is first achieved among the fine-structure levels of a given principle quantum number  $n$ , starting from high  $n$  and proceeding towards lower  $n$ . This situation is called partial local thermodynamic equilibrium or PLTE. In PLTE the fine-structure levels of a given  $n$  are populated according to their statistical weights  $g_j = 2 \cdot j + 1$  or  $g_l = 2 \cdot (2 \cdot l + 1)$ . At even higher collision rates PLTE will arrange also among the principle quantum numbers  $n$ , so that the energy levels of a given ion stage are populated according to their statistical weights  $g_n = 2 \cdot n^2$ .

There are several criteria helping to estimate the minimal conditions for  $l$ - or  $n$ -statistical

population. These are given in terms of scaling laws for a critical principle quantum number  $n_{cr}$ , above which PLTE is valid. A criterion for the  $l$ -statistical population of the fine-structure levels was given by Sampson [18]. A pendant for  $n$ -statistical population of the main energy levels was proposed by Griem [19]. Both criteria are based on rough estimates of the ratio of radiative and collisional processes. A more detailed criterion for PLTE among the principle quantum numbers was given by Fujimoto [20]. Basing on collisional radiative modeling, his criterion requests higher plasma densities for PLTE than claimed by Griem. Detailed, fine-structure resolved collisional radiative modeling [21] also revealed significantly stronger conditions for fine-structure PLTE than those proposed by Sampson.

### Population distribution in fusion plasmas

In magnetic fusion plasmas usually neither high nor low density limit are completely valid. With respect to the principle quantum numbers  $n$ , the low density limit is generally well fulfilled. This leads to very small fractions of excited ions  $N_z(nlj)$  relative to the total ion density  $N_z$ , so that any ion stage can in good approximation be considered completely in the ground state ( $N_z \approx N_z(gs)$ ). This is especially true for highly charged impurity elements.

Also for the distribution of ion stages the low density limit applies. Yet the initial radial ion distribution obtained from corona modeling can be significantly changed by radial particle transport and charge exchange recombination with neutral background gas.

With respect to the fine-structure levels the situation can vary from corona up to LTE conditions. The fine-structure population distribution within of a given ion stage  $z$  can be in corona limit for low  $n$  and in PLTE at high  $n$ , depending on the ion charge  $z$  and the plasma density. For the intermediate  $n$  neither of the limits will hold, so that detailed collisional radiative modeling will be required to describe the population distribution.

#### 3.1.3 The concept of effective rate coefficients

In corona limit, the population density of the excited ion state  $i$  caused by a certain atomic process - for example charge exchange - can be approximated by:

$$N_{z,i}^{cx} = \frac{\langle \sigma_{cx}(i) \cdot v \rangle \cdot n_0 \cdot N_{z+1}}{A_i}, \quad (3.21)$$

with  $\sigma_{cx}(i)$  being the cross section for charge exchange into the final state  $i$ . Together with equation 3.1 on page 14, the line intensity for the transition  $i \rightarrow j$  is then given by:

$$\begin{aligned} I_{ij}(cx) &= A_{ij} \cdot N_{z,i}^{cx} \cdot \hbar\omega_{ij} \\ &= \frac{\langle \sigma_{cx}(i) \cdot v \rangle \cdot A_{ij}}{A_i} \cdot n_0 \cdot N_{z+1} \cdot \hbar\omega_{ij}. \end{aligned} \quad (3.22)$$

The line intensity induced by charge exchange is obviously proportional to the rate coefficient  $\langle \sigma_{cx}(i) \cdot v \rangle$ . However, in equation 3.22 cascade contributions from higher energy levels and possible collisional redistribution are not considered. To take them

into account, collisional radiative modeling of the population densities  $N_{z,k}$  of all relevant energy states  $k$  is required. A collisional radiative model consists of a set of coupled rate equations, which balance all de-/populating processes for each level  $k$ . In steady state, each rate equation is given by:

$$\frac{dN_{z,k}}{dt} = 0 = R_{z,k}^{in}(N_{z,\neq k}) - R_{z,k}^{out}(N_{z,k}), \quad (3.23)$$

where the outflow  $R_{z,k}^{out}$  is proportional to  $N_{z,k}$  and the inflow  $R_{z,k}^{in}$  is a function of  $N_{z,\neq k}$ . The detailed modeling of the population densities  $N_{z,k}$  allows to define an effective rate coefficient for line emission. In case of the transition  $i \rightarrow j$  in the ion  $z$ , the effective rate coefficient for charge exchange  $Q_{cx}(ij)$  is given by:

$$Q_{cx}(ij) = \frac{N_{z,i}^{cx} \cdot A_{ij}}{N_{z+1} \cdot n_0}. \quad (3.24)$$

Within the concept of effective rate coefficients, processes directly connected to the ground state of an ion stage  $z$  are defined as source processes. As in fusion plasmas  $N_{z,gs} \approx N_z$  always holds, the ground states can be considered as 'reservoirs'. Besides excitation from the ground state, the source processes include all recombination processes. All other channels (radiative cascades, collisional de-/excitation, ionization) that emerge from excited states  $N_{z,k}$  are considered as 'secondary' effects, changing the initial population distribution caused by one of the source processes. The effective rate coefficient is specific for each source process and depends on the considered transitions.

A precondition for the concept of effective rate coefficients is the quasi steady state relation between the excited states  $N_{z,k}$  and the ground state  $N_{z,gs}$ . Due to their very short lifetimes, the excited states equilibrate with the ground state almost instantaneously. This ensures that the  $N_{z,k}$  follow the ion density  $N_z$  at any time. In case of meta stable states the quasi steady state relation is violated and an effective rate coefficient according to equation 3.24 cannot be deduced or will at least be time dependent.

With the effective rate coefficient  $Q_{cx}(ij)$ , the line intensity  $I_{ij}(cx)$  induced by charge exchange is now given by:

$$I_{cx}(ij) = Q_{cx}(ij) \cdot N_{z+1} \cdot n_0 \cdot \hbar\omega_{ij}. \quad (3.25)$$

This is analog to equation 3.22. The effective rate coefficient is a measure for the number of photons produced per pair of source particles ( $N_{z+1}$ ,  $n_0$ ). It gives a simple scalar relation between the measured line intensities and the physically relevant density of the involved ion stage  $N_z$  or  $N_{z+1}$ . Therefore, the effective rate coefficients are of crucial importance for absolute ion density measurements, as for example performed in charge exchange recombination spectroscopy.

Depending of the spectroscopic problem at hand, collisional radiative modeling in  $n$ -,  $nl$ - or  $nlj$ -resolution can be required. In case of multiple, spectroscopically unresolved upper levels  $k$ , equation 3.24 becomes:

$$Q_{cx}(ij) = \frac{\sum_k N_{z,ik}^{cx} \cdot A_{kj}}{N_{z+1} \cdot n_0}. \quad (3.26)$$

Effective rate coefficients of different source processes can simply be added. Some examples are listed below:

$$\begin{aligned}
Q_{exc}(ij) &= \frac{N_{z,i} \cdot A_{ij}}{N_z \cdot n_e} && \text{ground state excitation} \\
Q_{cx}(ij) &= \frac{N_{z,i} \cdot A_{ij}}{N_{z+1} \cdot n_0} && \text{charge exchange recombination} \\
Q_{rr}(ij) &= \frac{N_{z,i} \cdot A_{ij}}{N_{z+1} \cdot n_e} && \text{radiative recombination.}
\end{aligned} \tag{3.27}$$

### 3.2 Radial impurity transport

In any magnetically confined plasma, energy and particle transport mechanisms occur. It is distinguished between parallel transport along the magnetic field lines and radial transport perpendicular to the magnetic field lines. Parallel transport is generally much stronger than radial transport. This allows to handle a tokamak plasma within a 2D-model of the poloidal cross section, assuming toroidal symmetry. In case of circular cross sections, the plasma can be further reduced to a 1D-model of the minor radius.

The radial ion distribution in a tokamak plasma is influenced by perpendicular particle transport. Consider a trace impurity species of charge  $z$ . The radial continuity equation including perpendicular transport is given by [22]:

$$\frac{\partial N_z(r)}{\partial t} = \frac{1}{r} \cdot \frac{\partial}{\partial r} \left( r \cdot \Gamma_{\perp}^z(r) \right) + S_z(r), \tag{3.28}$$

where the source term  $S_z$  includes all ionization and recombination channels that connect  $N_z$  with  $N_{z+1}$  and  $N_{z-1}$ , respectively. The radial transport coefficient  $\Gamma_{\perp}(r)$  is generally expressed by a diffusive and a convective part [22]:

$$\Gamma_{\perp}(r) = -D_{\perp}(r) \cdot \frac{\partial N_z(r)}{\partial r} + v_{\perp}(r) \cdot N_z(r). \tag{3.29}$$

In the neoclassical treatment, the transport mechanisms are deduced from coulomb collisions between the plasma particles. The theoretical framework distinguishes between three different types of transport: The classical flux, the Pfirsch-Schlüter flux and the Banana-plateau flux. The classical flux arises from the perpendicular friction forces due to collisions between the gyrating ions. The Pfirsch-Schlüter flux is related to varying parallel friction forces due to deviations of temperature and pressure within a flux surface. It is dominant at high collision rates. The banana-plateau flux is caused by pressure anisotropies and is dominant at low collision rates. Each of the three mechanisms has individual diffusive and convective terms according to equation 3.29. The convective terms depend on the temperature and density gradients of the main plasma ions. They can be directed inwards or outwards, depending on the plasma parameters. This means convection can change orientation along the radius. For the radial impurity flux the overall transport including all three terms is relevant. (compare [23, 24])

The neoclassical theory predicts diffusion coefficients for plasma impurities in the order

of  $10^{-1} m^2/s$  ([2], p.196). However, experiments generally show much higher diffusivities in the order of 1 – 10 times of the neoclassical expectations ([25] p.497). This is referred to as anomalous transport. Anomalous transport is driven by turbulence, that goes back on micro instabilities. Up to now it is not fully understood. Yet for experimentally observed impurity transport, an empirical formula has proven to be adequate in many cases [2, 22]:

$$\Gamma_{\perp} = D_{\perp} \cdot \left( \frac{dN_z}{dr} - \alpha_v \cdot \frac{r}{a^2} \cdot N_z \right). \quad (3.30)$$

Here  $a$  is the minor radius of the tokamak and  $\alpha_v$  is a positive scalar factor. According to equation 3.30, the convective transport term is directed inwards and scales with the diffusion coefficient  $D_{\perp}$  and the radial position.

Experimentally determined diffusion coefficients for impurity elements are typically divided into two radial zones. In the plasma center the diffusivity tends to be low and  $D_{\perp}$  can approach neoclassical values. Towards the edge the diffusivity strongly increases to highly anomalous values of up to  $D_{\perp} = 6 m^2/s$  ([2] p.221). The transition between both regions is usually quite sharp and in some cases spatially coincides with the rational  $q$ -surfaces<sup>2</sup>. Experimental results from different tokamaks and different impurities can for example be found in [26–32]. In some cases also narrow dips in  $D_{\perp}(r)$  (transport barriers) have been observed [33, 34].

### 3.3 X-ray spectroscopy

High resolution X-ray spectroscopy on plasma impurities is a well established, powerful diagnostic method. It can generally be applied on high and medium  $z$  elements. These include inherent impurities like for example tungsten or iron coming from plasma facing components, but also injected species like argon or krypton. The latter are used for radiative cooling or are seeded especially for diagnostic purposes. For several reasons, the He-like ion stages of these elements are favored for spectroscopy. Due to the stable noble gas configuration, the He-like ion stage is dominant within a broad temperature range. According to figure 3.4(a) on page 22,  $Ar\ xVII$  is dominant for  $0.4 keV \leq T_e \leq 2.0 keV$ . This ensures that  $Ar\ xVII$  is abundant within a major part of the poloidal plasma cross section of many mid size tokamaks like TEXTOR. At higher plasma temperatures, heavier elements will be preferred. For example the He-like stage of iron is most relevant around  $T_e = 3 keV$ , in case of krypton around  $T_e = 10 keV$  [12].

Furthermore, the level of complexity of the He-like spectra is optimal for diagnostic applications. On the one hand, the line structure is simple enough to be modeled in detail, but at the same time is complex enough to reveal various information about the plasma environment. This is especially true in case of the  $K_{\alpha}$ -spectrum, where the well

---

<sup>2</sup>The safety factor  $q$  gives the ratio of the toroidal angle  $\Delta\Phi$  covered by an helical magnetic field line within one complete poloidal rotation ( $\Delta\Theta = 2\pi$ ). For large aspect ratio tokamaks ( $R \gg a$ ), it can be approximated by  $q = r \cdot B_{\Phi} / R \cdot B_{\Theta}$ , where  $B_{\Phi}$  and  $B_{\Theta}$  are the toroidal and the poloidal magnetic fields, respectively. (compare [2] p.111 and p.222)

resolved satellite lines from the adjacent Li-like state can be included in the analysis. A further advantage is, that the  $K_\alpha$ -lines and their satellites are emitted within a very narrow wavelength interval. Therefore, a detailed relative calibration of the spectrometer can be omitted.

The first high resolution He-like X-ray spectra from fusion plasmas have been reported from iron seeding experiments at the PLT tokamak in 1979 by Bitter et al. [35]. Almost simultaneously the X-ray emission of chromium ions was measured at the TFR tokamak [36]. Since then,  $K_\alpha$ -spectroscopy has been developed to a high precision diagnostic tool, that allows to measure the electron and ion temperature, the density ratios of the involved ion stages as well as the plasma rotation. It is not only widely used on controlled nuclear fusion plasmas, like for example at TORESUPRA [37], TEXTOR [38, 39] or ALCATOR [40], but also on astrophysical plasmas [41]. Nowadays, the advent of imaging X-ray spectrometers allows 2D-scans of the  $K_\alpha$ -emission, as presented in [42] or in [43]. (compare [3, 39])

### 3.3.1 The $K_\alpha$ -spectrum of He-like argon

In this chapter the  $K_\alpha$ -transitions in He-like argon and the corresponding satellite spectrum is introduced. After a description of the line structure and the related diagnostic possibilities, some open questions in literature are reviewed. Throughout this thesis the  $K_\alpha$ -transitions in the He-like system and the associated Li-like satellite lines are together referred to as the  $K_\alpha$ -spectrum.

As mentioned above, argon is a common trace impurity in controlled fusion plasmas. It is either seeded in minimal amounts for different diagnostic purposes, or is injected in higher amounts for radiative cooling.

#### The level structure

With excitation energies of ca.  $3.1 \text{ keV}$ , the  $K_\alpha$ -spectrum of He-like argon is emitted at wavelengths close to  $4 \text{ \AA}$ . The spectrum is dominated by the  $K$ -shell transitions ( $1s2l - 1s^2$ ). These include from the high to the low energy end the resonance line **w** ( $1s2p(^1P_1) - 1s^2(^1S_0)$ ), the magnetic quadrupole line **x** ( $1s2p(^3P_2) - 1s^2(^1S_0)$ ), the intercombination line **y** ( $1s2p(^3P_1) - 1s^2(^1S_0)$ ) and the forbidden line **z** ( $1s2s(^3S_1) - 1s^2(^1S_0)$ ). All lines are labeled according to Gabriel [44]. Between **w** and **z** additionally several weaker satellites occur, which correspond to transitions from doubly excited states in the Li-like ion stage ( $1s2pnl - 1s^2nl$ ). The satellites are mainly due to dielectronic recombination of *Ar XVII*, though some also feature strong contributions from inner shell excitation of *Ar XVI*. According to the principle quantum number of the second excited electron in the upper state, all satellites can be assigned to the groups **n<sub>2</sub>** ( $1s2p2l$ ), **n<sub>3</sub>** ( $1s2p3l$ ) and **n<sub>≥4</sub>** ( $1s2pnl$ ,  $n \geq 4$ ), respectively. Only in **n<sub>2</sub>** individual lines are resolved (**k**, **j**, **q**, **r**, **s**, **a**, **t**). Among these the strongest satellites are **k** and **j**, which are both purely driven by dielectronic recombination. While **k** is well isolated, **j** is superposed by the **z**-line. Also the satellites **q** and **r** are important. Here the contributions from inner shell excitation are dominant. The groups **n<sub>3</sub>** and **n<sub>≥4</sub>** are found at the high energy end

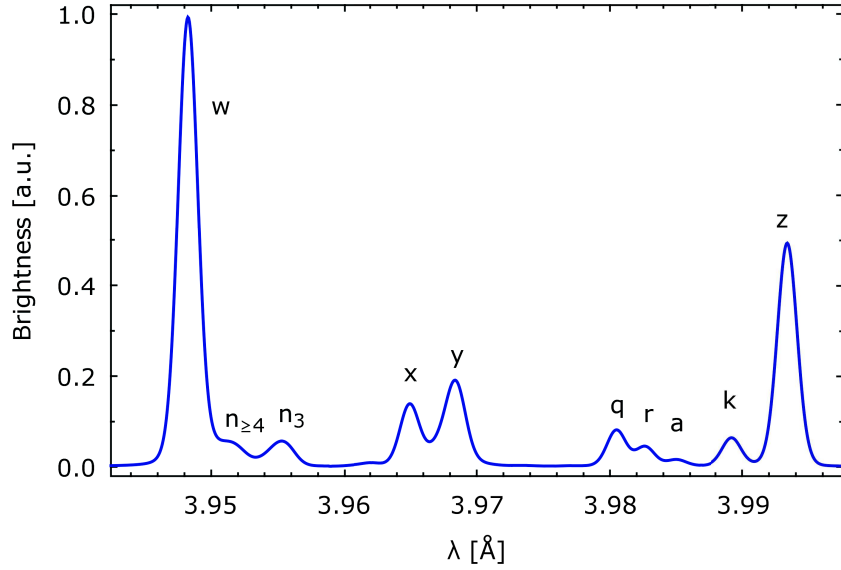


Figure 3.5: The  $K_\alpha$ -transitions and the associated satellite spectrum of He-like argon measured along a central chord in TEXTOR. The most relevant lines are labeled according to Gabriel [44].

of the spectrum, while  $\mathbf{n}_{\geq 4}$  is partly blending with the resonance line  $\mathbf{w}$ .

The He-like lines are mainly supplied by excitation from the ground state. Additionally, they feature cascade contributions from recombination processes of the H-like stage. These include radiative, dielectronic and charge exchange recombination, while the latter depends on the neutral particle density. According to the cascade matrix of the He-like system, the recombination contributions mainly affect the triplet lines ( $\mathbf{x}$ ,  $\mathbf{y}$ ,  $\mathbf{z}$ ) and have only weak impact on the strong singlet line  $\mathbf{w}$ . The  $\mathbf{z}$ -line additionally receives contributions from inner shell ionization of the Li-like ground state ( $1s^22s$ ).

Figure 3.5 shows an example spectrum measured at TEXTOR. All relevant transitions are listed in table 3.1. Finally, the level structure and the population mechanisms are illustrated in figure 3.6.

### Plasma diagnostics based on the $K_\alpha$ -spectrum

The  $K_\alpha$ -spectrum of He-like argon is widely used for temperature diagnostics in hot fusion plasmas. It readily gives access to the ion temperature  $T_i$  and the plasma velocity  $v_t$  from Doppler broadening and Doppler shift, respectively. The line intensity ratios within the spectrum further allow to determine the electron temperature  $T_e$  as well as the argon ion ratios  $Ar\text{ XVI} / Ar\text{ XVII}$  and  $Ar\text{ XVIII} / Ar\text{ XVII}$ . In the following the diagnostic opportunities are discussed. Further details can for example be found in [12, 39, 45].

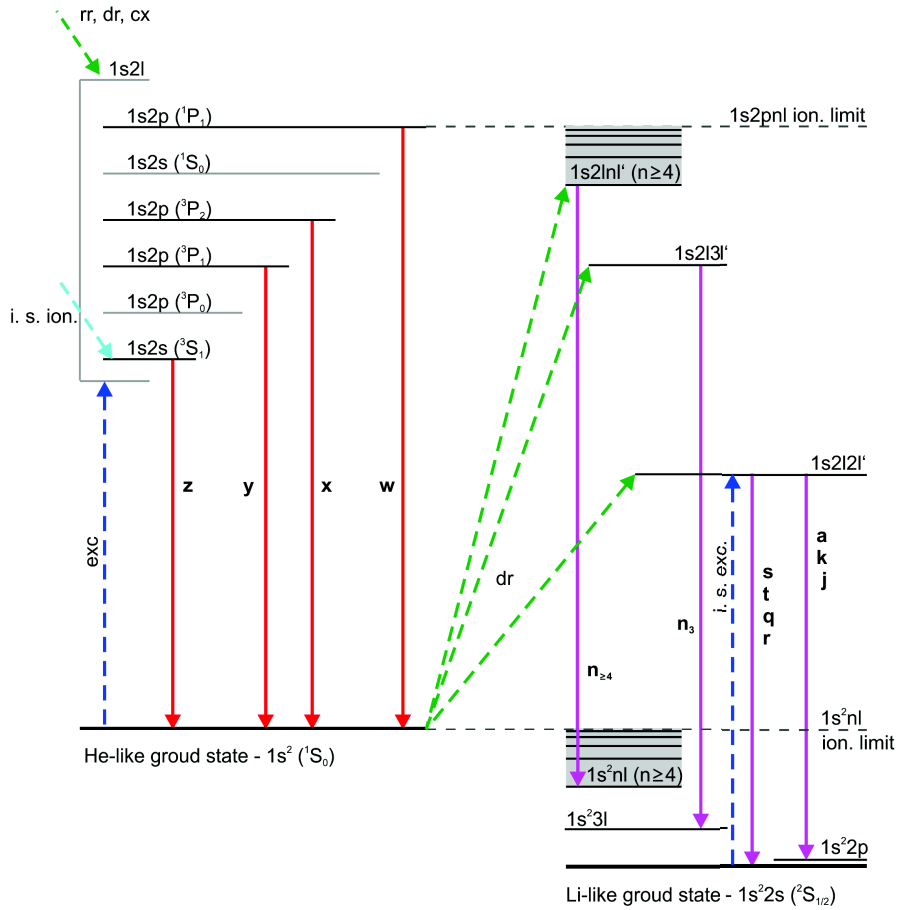


Figure 3.6: Grotrian diagram of the He-like and Li-like argon stages. Only energy levels directly relevant for the emission of the  $K_{\alpha}$ -lines and the associated satellite spectrum are shown. The energy differences are not displayed in true scale. The dashed arrows indicate the most important population mechanisms: excitation (exc.), radiative recombination (rr), dielectronic recombination (dr), charge exchange recombination (cx), inner shell excitation (i. sh. exc.) and inner shell ionization (i. sh. ion.).

Label [44]	$\lambda$ [Å] [12]	Lower state	-	Upper state
<b>w</b>	3.9492	$1s^2(^1S_0)$	-	$1s2p(^1P_1)$
<b>x</b>	3.9660	$1s^2(^1S_0)$	-	$1s2p(^3P_2)$
<b>y</b>	3.9695	$1s^2(^1S_0)$	-	$1s2p(^3P_1)$
<b>z</b>	3.9943	$1s^2(^1S_0)$	-	$1s2s(^3S_1)$
<b>s</b>	3.9678	$1s^22s(^2S_{\frac{1}{2}})$	-	$1s2s2p(^2P_{\frac{3}{2}})$
<b>t</b>	3.9687	$1s^22s(^2S_{\frac{1}{2}})$	-	$1s2s2p(^2P_{\frac{1}{2}})$
<b>q</b>	3.9815	$1s^22s(^2S_{\frac{1}{2}})$	-	$1s2s2p(^2P_{\frac{3}{2}})$
<b>r</b>	3.9836	$1s^22s(^2S_{\frac{1}{2}})$	-	$1s2s2p(^2P_{\frac{1}{2}})$
<b>a</b>	3.9860	$1s^22p(^2P_{\frac{3}{2}})$	-	$1s2p^2(^2P_{\frac{3}{2}})$
<b>k</b>	3.9900	$1s^22p(^2P_{\frac{1}{2}})$	-	$1s2p^2(^2D_{\frac{3}{2}})$
<b>j</b>	3.9941	$1s^22p(^2P_{\frac{3}{2}})$	-	$1s2p^2(^2D_{\frac{5}{2}})$
<b>n<sub>3</sub></b>		$1s^23l$	-	$1s2p3l$
<b>n<sub>4</sub></b>		$1s^2nl, n \geq 4$	-	$1s2pnl, n \geq 4$

Table 3.1: List of the most prominent transitions in the  $K_\alpha$ -spectrum of He-like argon including the associated satellite lines.

**The ion temperature and the plasma velocity** The profile of a spectral line is Doppler-broadened due to the thermal velocity distribution of the emitting ion species. In case of a Maxwellian velocity distribution, the width of the Gaussian Doppler profile is given by:

$$\Delta\lambda_{FWHM} = \lambda \cdot \sqrt{8 \cdot \ln(2) \cdot \frac{k_b \cdot T_i}{m_i \cdot c^2}}, \quad (3.31)$$

where  $k_b$  is the Boltzman constant,  $T_i$  is the ion temperature,  $m_i$  is the ion mass,  $c$  is the speed of light and  $\lambda$  is the wavelength. For the analysis of a measured spectral line, also the natural and the instrumental line width have to be taken into account. The natural line width is generally smaller than the Doppler width. According to the uncertainty principle, it is related to the life time  $\tau$  of the decaying state and has a Lorentzian profile shape ( $\Gamma = \hbar/\tau$ ). The convolution of the Gaussian and the Lorentzian profiles leads to a Voigt profile. The instrumental line width is discussed in section 4.

The Doppler shift of the spectral lines is related to the plasma velocity in direction of the line of sight. For the shift of the original wavelength  $\lambda$  holds:

$$\Delta\lambda_v = \lambda \cdot \left(1 - \frac{v \cdot \cos(\alpha)}{c}\right), \quad (3.32)$$

with  $v$  being the plasma velocity and  $\alpha$  being the angle between the line-of-sight and the direction of plasma rotation.

**The electron temperature** The relative brightness of the resonance line **w** and the dielectronic satellites are monotonic functions of the electron temperature. In both cases

the population of the upper levels is mainly supplied by the ground state of  $Ar\ XVII$ , so that the intensity ratio does not depend on the argon ion balance. This allows a distinct determination of  $T_e$ . The only well isolated pure dielectronic satellites are  $\mathbf{k}$  and the unresolved group  $\mathbf{n}_3$ . For the intensity ratio of  $\mathbf{k}$  and  $\mathbf{w}$  holds:

$$\frac{I_k}{I_w} \approx \frac{Q_{dr,k}(T_e) \cdot N(Ar\ XVII) \cdot n_e}{Q_{exc,w}(T_e) \cdot N(Ar\ XVII) \cdot n_e} = \frac{Q_{dr,k}(T_e)}{Q_{exc,w}(T_e)} = f_{kw}(T_e), \quad (3.33)$$

where the  $Q_{dr,k}$  and  $Q_{exc,w}$  are the effective rate coefficients for dielectronic recombination and excitation from the ground state, respectively, and  $N(Ar\ XVII)$  is the density of the He-like argon stage. In equation 3.33 recombination contributions to  $I_w$  were neglected for the sake of simplicity.

The intensity ratios  $f_{kw}(T_e)$  and the equivalent  $f_{n_3w}(T_e)$  are plotted in figure 3.7(a). Obviously,  $f_{kw}(T_e)$  has a stronger  $T_e$ -gradient than  $f_{n_3w}(T_e)$ . Moreover,  $\mathbf{k}$  is a single line and has a simpler structure than the group of unresolved satellite lines in  $\mathbf{n}_3$ . Therefore, usually  $\mathbf{k}$  is preferred for electron temperature measurements.

The comparison of the dielectronic satellites and the resonance line corresponds to a two-point measurement of the Maxwellian energy distribution of the electrons. The excitation of the  $\mathbf{w}$ -line can only be induced by the high energy tail of the Maxwell distribution with  $E \geq E_w$ . In contrast to this, the resonant dielectronic capture populating the upper level of  $\mathbf{k}$  is only possible for electrons from a very narrow energy region. This allows an absolute electron temperature measurement, which of course requires a Maxwellian plasma. The principles are illustrated in figure 3.7(b).

**The argon ion ratio  $Ar\ XVI / Ar\ XVII$**  The inner shell excitation part of the satellite spectrum is supplied by the ground state of the Li-like argon ion stage. Therefore, the ion ratio  $Ar\ XVI / Ar\ XVII$  can be determined from the intensities of the satellites  $\mathbf{q}$  and  $\mathbf{r}$  relative to the  $\mathbf{w}$ -line. The intensity ratio of  $\mathbf{q}$  and  $\mathbf{w}$  is given by:

$$\frac{I_q}{I_w} = \frac{Q_{iexc,q}(T_e) \cdot N(Ar\ XVI) \cdot n_e}{Q_{exc,w}(T_e) \cdot N(Ar\ XVII) \cdot n_e} = \frac{Q_{iexc,q}(T_e)}{Q_{exc,w}(T_e)} \cdot \frac{N(Ar\ XVI)}{N(Ar\ XVII)}, \quad (3.34)$$

with  $Q_{iexc,q}$  being the effective rate coefficient for inner shell excitation. Provided that the electron temperature is known, this allows a measurement of the relative abundance of the Li-like and the He-like argon ion stages.

In equation 3.34 the dielectronic component of  $\mathbf{q}$  is neglected. It is supplied by the He-like ion stage and needs to be subtracted from the total intensity of  $\mathbf{q}$ . This is possible, as the entire dielectronic satellite pattern can be identified in relation to the well isolated pure dielectronic satellites  $\mathbf{k}$  or  $\mathbf{n}_3$ .

**The argon ion ratio  $Ar\ XVIII / Ar\ XVII$**  The  $K_\alpha$ -transitions  $\mathbf{w}$ ,  $\mathbf{x}$ ,  $\mathbf{y}$  and  $\mathbf{z}$  are primarily induced by excitation from the ground state of  $Ar\ XVII$ . However, the  $K_\alpha$ -line intensities

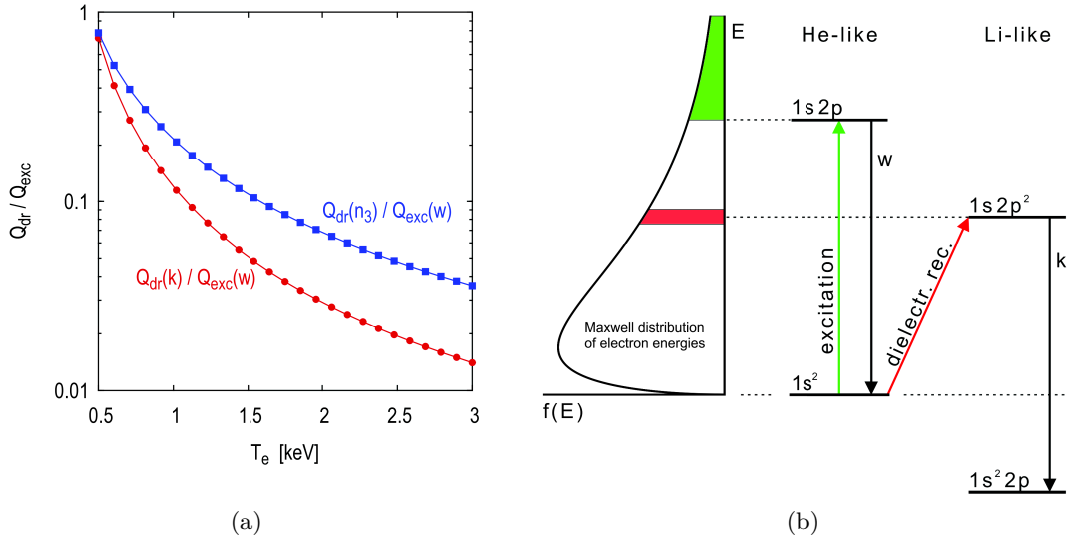


Figure 3.7: **a)** Theoretical intensity of the dielectronic satellites  $\mathbf{k}$  and  $\mathbf{n}_3$  relative to the resonance line  $\mathbf{w}$  according to data from [12]. **b)** Grotrian diagram illustrating the principles of population by dielectronic recombination and excitation (compare [3] p. 183.)

can also contain significant recombination parts. For the intensity of any  $K_\alpha$ -line  $\mathbf{i}$  holds<sup>3</sup>:

$$I_i \propto N(\text{Ar } XVII) \cdot n_e \cdot Q_{exc,i}(T_e) + N(\text{Ar } XVIII) \cdot \left[ n_e \cdot \left( Q_{rr,i}(T_e) + Q_{dr,i}(T_e) \right) + n_0 \cdot Q_{cx,i}(T_e) \right]. \quad (3.35)$$

Here  $Q_{rr,dr,cx}$  are the effective rate coefficients for radiative, dielectronic and charge exchange recombination, respectively. According to the cascade matrix of the He-like system, the recombination contributions have stronger impact on the triplet lines  $\mathbf{x}$ ,  $\mathbf{y}$  and  $\mathbf{z}$ , than on the singlet  $\mathbf{w}$ . From their population characteristics for the different lines the excitation and recombination parts can be separated. This allows a determination of the argon ion ratio  $\text{Ar } XVIII/\text{Ar } XVII$ . Due to the charge exchange contributions, the obtained  $\text{Ar } XVIII/\text{Ar } XVII$  depends on the neutral particle density  $n_0$ .

It shall be mentioned, that for a correct interpretation of the  $K_\alpha$ -intensities the blended dielectronic satellite spectrum needs to be subtracted. As mentioned above, the entire satellite pattern can be identified with the help of the well isolated  $\mathbf{k}$  or  $\mathbf{n}_3$ . For the analysis presented in chapter 5, the argon ion ratio  $\text{Ar } XVIII/\text{Ar } XVII$  is determined from the intensities of the lines  $\mathbf{x}$  and  $\mathbf{y}$  relative to  $\mathbf{w}$ .

**Forward modeling of the line integrated signals** In passive spectroscopy the observed spectral information is integrated along the line-of-sight and can contain contributions

<sup>3</sup>In case of the  $\mathbf{z}$ -line also the contributions from inner shell ionization have to be included.

from the entire plasma cross section. In case of a radially symmetric plasma, the intensity of an  $Ar\ xVII$  excitation line observed along a central, radial chord is given by:

$$I_{exc} \propto \int_0^1 N(Ar\ xVII)(\rho) \cdot n_e(\rho) \cdot Q_{exc}(T_e(\rho)) \cdot d\rho', \quad (3.36)$$

where  $\rho$  is the normalized minor plasma radius. The radial emission profile (the integrand on the right hand side of equation 3.36) can be determined by tomographic methods like an Abel-inversion. Alternatively, a forward integration can be performed. Here the measurable projection of the spectral emission is reconstructed according to equation 3.36. However, the forward modeling of the line integrated signals requires radial profiles of the ion densities ( $N(Ar\ xVII)(\rho)$ ) and other relevant quantities like the plasma temperature or the neutral particle density. In contrast to tomographic inversion, this method can also be applied to 1D spectral data, though it then does not necessarily give unique results.

The analysis of the  $K_\alpha$ -spectrum presented in this work is based on forward integration, while the argon ion balance is either considered to be coronal or is calculated using a 1D-transport model (see section 5.2). The total argon ion density is assumed to be proportional to the electron density ( $N(Ar_{tot})(r) = \sum_q N(Ar^{q+})(r) \propto n_e(r)$ ). Furthermore, the plasma cross section in TEXTOR is assumed to be radially symmetric.

**The fitting of the spectral lines** For modeling a measured  $K_\alpha$ -spectrum, the following theoretical spectrum is fitted to the experimental data:

$$\begin{aligned} I(\lambda) = 2 \cdot \int_0^1 d\rho' n_e(\rho) \cdot \tilde{N}(Ar_{tot})(\rho) \cdot \tilde{N}(Ar\ xVII)(\rho) \cdot \left[ \alpha_{he}(\lambda, T_e(\rho)) \right. \\ \left. + \frac{N(Ar\ xVIII)}{N(Ar\ xVII)}(\rho) \cdot \left( \alpha_h(\lambda, T_e(\rho)) + \frac{n_0}{n_e}(\rho) \cdot \alpha_0(T_e(\rho)) \right) \right. \\ \left. + \frac{N(Ar\ xVI)}{N(Ar\ xVII)}(\rho) \cdot \alpha_{li}(\lambda, T_e(\rho)) \right]. \end{aligned} \quad (3.37)$$

Here the  $\alpha_{li}$ ,  $\alpha_{he}$  and  $\alpha_h$  include the effective rate coefficients of all relevant processes connected to the ion stages  $Ar\ xVI$ ,  $Ar\ xVII$  and  $Ar\ xVIII$ , respectively. The argon ion density profiles are separated into the total argon density profile  $\tilde{N}(Ar_{tot})(\rho)$  and the relative ion fractions  $\tilde{N}(Ar\ xVI, xVII, xVIII)(\rho)$ , so that for example  $N(Ar\ xVII)(\rho) = \tilde{N}(Ar_{tot})(\rho) \cdot \tilde{N}(Ar\ xVII)(\rho)$ . As mentioned above, the total argon density is assumed to be proportional to the electron density.

The fit parameters are the electron temperature  $T_e$ , the ion temperature  $T_i$  as well as the argon ion density ratios  $N(Ar\ xVI)/N(Ar\ xVII)$  and  $N(Ar\ xVIII)/N(Ar\ xVII)$ . During the fit procedure, the ion density profile shapes needed for the forward integration are kept constant and only the central values are varied. The same holds for the temperature profiles of  $T_e(r)$  and  $T_i(r)$ .

In order to fit equation 3.37 to the experimental data, the spectrum is divided into several wavelength intervals that are fitted independently. These intervals are illustrated in figure 3.8, they include **w**, **n<sub>3</sub>**, **x+y**, **q+r**, **k** and **z**. The spectrum is fitted in an iterative procedure:

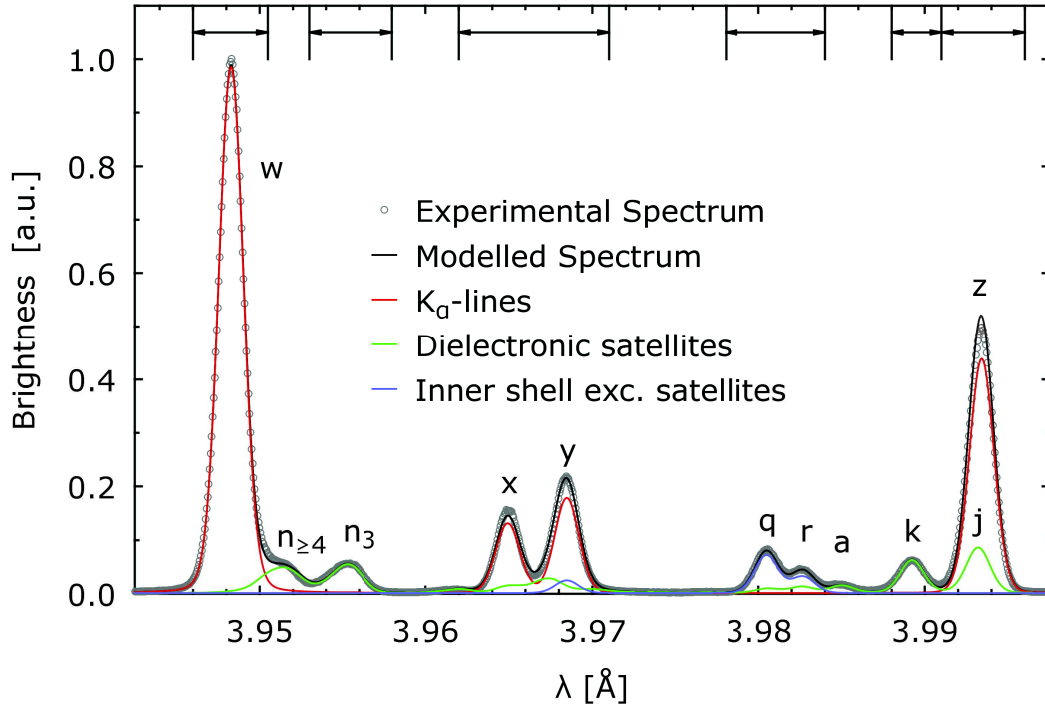


Figure 3.8: Theoretical  $K_\alpha$ -spectrum of He-like argon fitted to experimental data measured at TEXTOR. The  $K_\alpha$ -lines and the satellites are illustrated individually.

1. The background is fitted based on a parabolic function at three positions free of spectral lines.
2. The ion temperature  $T_i$  is determined from the Doppler width of **w** or **z**.
3. The electron temperature  $T_e$  is determined from the intensity of **k** or **n<sub>3</sub>** relative to **w**.
4. The argon ion ratio  $Ar\text{ XVIII}/Ar\text{ XVII}$  is determined from the recombination contributions on the triplet lines using the relative intensities of **x+y** and **w**. Due to charge exchange contributions, the result depends on the value of  $n_0/n_e$ .
5. The argon ion ratio  $Ar\text{ XVI}/Ar\text{ XVII}$  is determined from the intensity of **q+r** relative to **w**.

This procedure is repeated until best consistency is reached. The atomic data used for the  $K_\alpha$ -lines and the most prominent satellites are shown in figure 3.9. Further details about the applied routine and the atomic data can be found in [12].

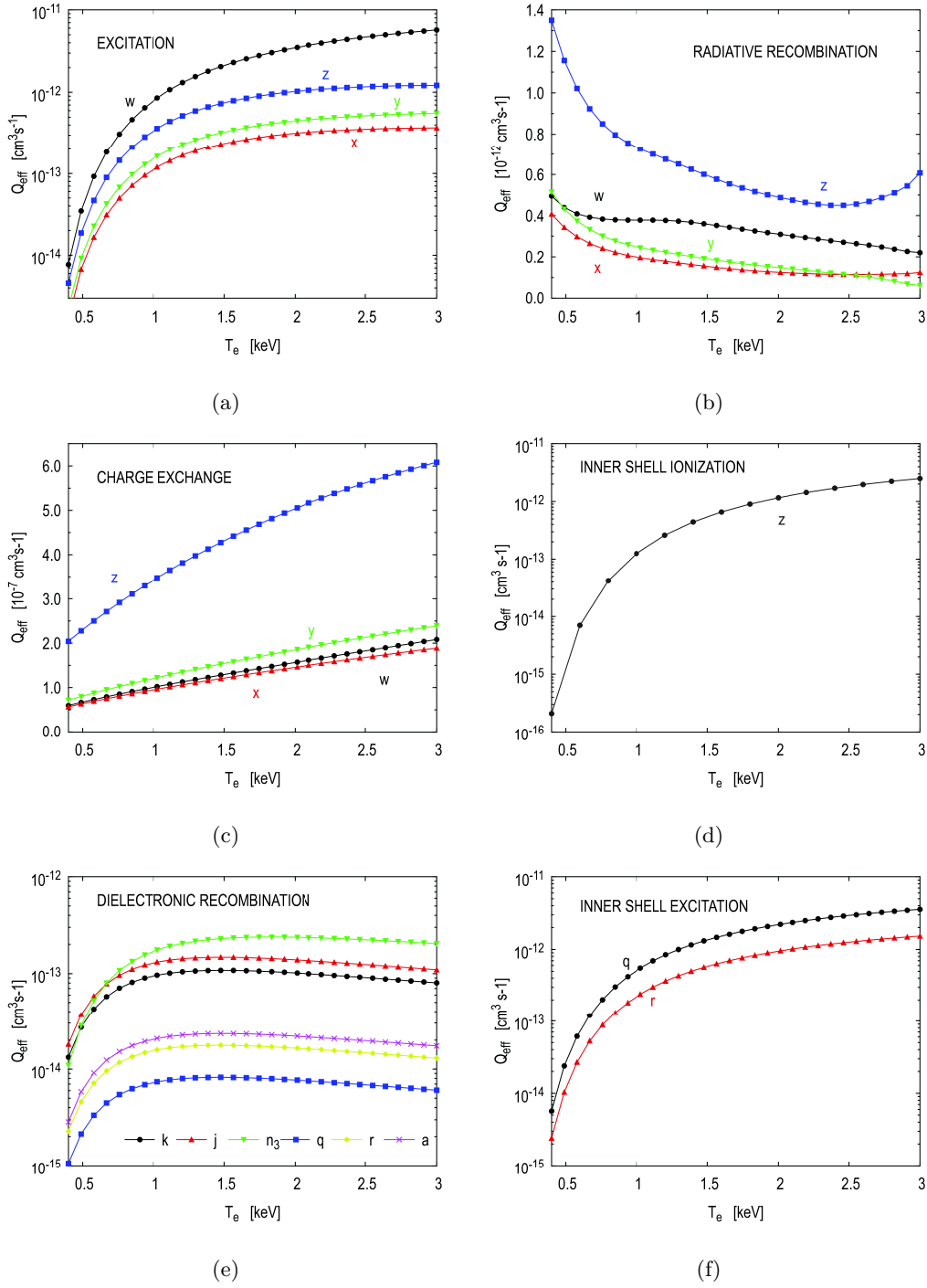


Figure 3.9: Effective rate coefficients used for modeling the  $K_{\alpha}$ -lines and the associated satellite spectrum. Only data for the most prominent lines are shown. All data is taken from [12], except the effective rates for radiative recombination [46].

## The $K_\alpha$ -spectrum in literature

Although widely used in plasma temperature and velocity diagnostics, the  $K_\alpha$ -spectrum has been in the scope of controversial discussions in the past. The open questions are in widest sense related to the relevance of charge exchange recombination for the observed line ratios.

Independent experiments at TEXTOR produced contradicting results concerning the radial impurity transport. As discussed in the previous sections, the spectral emission of heavy impurity elements can be influenced by radial particle transport as well as by charge exchange recombination with neutral particles. Both processes cause changes in the ideal coronal ion balance, while charge exchange additionally affects the population densities of the excited ion states. Also the  $K_\alpha$ -spectra of He-like argon measured at TEXTOR show systematic deviations from the line intensity ratios expected from corona calculations. These deviations appear as increased Li-like satellites **q** and **r** and also as increased He-like triplet lines **x**, **y** and **z**. In 1999 Rosmej et al. [47] modeled the  $K_\alpha$ -emission measured in the plasma center of TEXTOR (no radial resolution). He described the deviations from the corona values mainly based on charge exchange effects, while only low (neoclassical) radial diffusion coefficients were needed. In contradiction to this Biel et al. [30, 31] could only reconstruct the temporal evolution of argon spectra with the help of clearly anomalous transport coefficients. The experiment was based on the emission of several argon ion stages in the VUV and the soft X-ray region measured along a central chord in TEXTOR. A sharply bordered region of high diffusivity was deduced. This discrepancy has not been resolved up to now.

Already before X-ray imaging spectrometers allowed an easy monitoring of emission profiles a radial scan of the argon emission in ALCATOR plasmas was achieved in 1987 by Rice et al. [40]. On a shot to shot basis the spectrometers line of sight was shifted stepwise from the plasma center towards the edge. The radially resolved measurements revealed inverting intensity ratios of the singlet and the triplet lines in the  $K_\alpha$ -spectrum. This behavior of the line intensity ratios has not entirely been explained. A detailed discussion of the ALCATOR results is given in chapter 5.

These long standing open questions involving the  $K_\alpha$ -spectrum of He-like argon can be addressed with the new diagnostic opportunities at TEXTOR provided by the W7-X imaging X-ray spectrometer. The spatially resolved measurements will especially contribute to resolve the controversy concerning the impurity transport in TEXTOR.

## 4 Experimental setup

The results presented in this thesis are based on X-ray spectra measured in argon seeded plasmas at the tokamak TEXTOR. Two different Bragg-spectrometers were involved in the experiments. This part gives an overview of the tokamak TEXTOR and the two spectrometers.

### 4.1 The tokamak TEXTOR

The tokamak TEXTOR (**T**orus **E**xperiment for **T**echnology-**O**riented **R**esearch) is a medium sized limiter machine with a major radius of  $R = 1.75 \text{ m}$  and a minor radius of  $a = 0.47 \text{ m}$  [48]. The plasma cross section is circular. TEXTOR has a total of 16 main field coils inducing a toroidal magnetic field  $B_T$  of up to  $2.8 \text{ T}$ , while the plasma current  $I_P$  is typically  $300 - 400 \text{ kA}$ . In ohmic operation TEXTOR reaches electron temperatures  $T_e$  of  $1 - 2 \text{ keV}$  at averaged electron densities  $\bar{n}_e$  of  $1 - 4 \cdot 10^{13} \text{ cm}^{-3}$ . Two tangential neutral particle injectors NBI-1 and NBI-2 provide additional heating power. In the beam heated mode electron temperatures of  $T_e \approx 2.5 \text{ keV}$  are possible and also slightly higher plasma densities can be reached. The duration of one discharge is typically  $5 - 6 \text{ s}$  including a  $3 - 4 \text{ s}$  flat top phase with constant density and temperature. In the normal configuration the plasma current in TEXTOR is oriented anticlockwise. By inverting the magnetic fields, it is possible to operate TEXTOR with reversed plasma current. This allows to realize mirrored plasma scenarios as used for the experiments presented in section 7.2.

The plasma is shaped by different limiter elements (see figure 4.1(b)). First to mention is the adjustable ALT-limiter that is located at the low field side below the equatorial plane. On the high field side the plasma is limited by the graphite tiles covering the vessel walls (bumper limiter). In addition, two smaller limiter elements are installed at the top and the bottom side of the vessel, respectively. Their toroidal position is marked in figure 4.1(a). The ALT-limiter normally defines the last closed flux surface (LCFS) and provides the largest, most relevant surface for plasma-wall interaction.

The two neutral particle injectors are oriented in opposite tangential directions (see figure 4.1(a)). In normal field mode the direction of NBI-1 matches the direction of the toroidal plasma rotation (co-beam). Due to the reversible plasma current each beam can be used as co- or counter-beam. Each beam has a rectangular cross section of  $50 \text{ cm} \times 50 \text{ cm}$  that can be stagelessly narrowed down to zero in vertical direction to reduce the amount of particles entering the plasma. The fast neutral particles are produced by accelerating hydrogen ions with high-voltage in the range of  $20 - 50 \text{ kV}$ . The fast ions then pass a gas chamber where they are neutralized via charge exchange reactions. Besides  $H^+$  also the molecule ions  $H_2^+$  and  $H_3^+$  are accelerated, so that the neutral beam consists

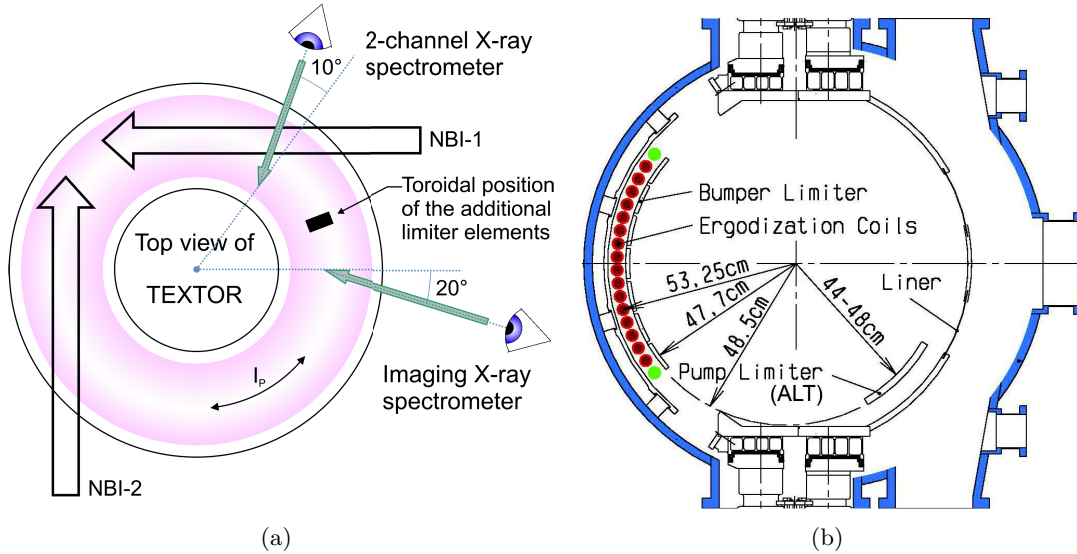


Figure 4.1: **a)** Top view of the tokamak TEXTOR illustrating the toroidal positions and orientations of the neutral beam injectors NBI-1/2, the two X-ray spectrometers involved in the experiments and the top/bottom main limiters. **b)** Poloidal cut of TEXTOR illustrating the poloidal positions of the limiter elements [49].

of three energy components ( $E_1 = E$ ,  $E_2 = E/2$ ,  $E_3 = E/3$ ). The maximal voltage of 50 kV leads to particles energies of 50 keV, 25 keV and 16.7 keV.

TEXTOR is equipped with a trace gas injection facility for impurity seeding. In the presented experiments it is used to supply the fractional argon density needed for X-ray spectroscopy. The injector is based on a piezo valve that allows to control the amount of gas injected into the plasma vessel by setting the shutter frequency as well as the ratio of opening and closing time. Also the argon pressure in the gas chamber has a strong influence on the injected number of particles. During the experiments argon was injected under a variety of different valve settings and starting times.

## 4.2 The X-ray spectrometers

Two different X-ray spectrometers specialized on measuring the line emission of He-like argon have been installed at TEXTOR. Both devices are Johann-type spectrometers observing the TEXTOR plasma along almost radial lines of sight, but at different toroidal positions (figure 4.1(a)). As the spectrometers were not operational at a time, no simultaneously measured data is available.

This section starts with a general discussion of X-ray spectrometers in the Johann-design and then shortly describes both spectrometer units.

### 4.2.1 Johann-type X-ray spectrometers

X-ray or Bragg-spectrometers use crystals as dispersive elements, which have a lattice constant comparable to the wavelengths of interest  $\lambda$ . The X-ray photons impinge on the crystal surface under an angle  $\theta$  and are reflected at different atomic layers. As a consequence, the photons carry optical path differences in the order of  $\lambda$ . These phase differences depend on the angle of observation, which due to constructive and destructive interference results in a diffraction pattern. The conditions for constructive superposition of the reflected X-rays are given by the Bragg relation:

$$n \cdot \lambda = 2d \cdot \sin(\theta), \quad (4.1)$$

where  $\theta$  is the angle of incidence and observation relative to the crystal surface, the integer  $n$  is the order of the deflection maximum (normally  $n = 1$ ) and  $2d$  is the lattice constant of the crystal.

X-ray spectrometers designed in the Johann layout use bent Bragg crystals. These combine dispersive and focusing properties, so that a sharp depiction of the diffraction pattern is possible. In case of a cylindrically bent crystal the focal line describes a circle in the plane of curvature called the Rowland circle. Its radius is given by  $R_{rw} = R_{cr}/2$  with  $R_{cr}$  being the radius of the crystal curvature. For a sharp depiction of the observed spectrum, the light source as well as the detector need to be placed on the Rowland circle. The principles of the Johann layout are illustrated in figure 4.2.

The cylindrical curvature described above only focuses perpendicularly to the cylinder axis and therefore displays no spatial information. Spherically bent crystals are not limited to one direction of incidence, due to spherical symmetry. Therefore, they allow for spatially resolved X-ray spectroscopy (imaging) based on only one crystal. Similar to a spherical mirror, a spherical crystal shows strong astigmatic depiction errors when illuminated off axis. Instead of a distinct focal point there are two perpendicular focal lines. One of them lies in the plane of incidence and observation. It is identical to the Rowland circle known from the cylindrical case and is also referred to as the meridional focus. The other focal line is oriented perpendicularly to the plane of incidence and observation and is called the sagittal focus. For the meridional and the sagittal foci  $f_m$  and  $f_s$  holds [39, 50]:

$$\begin{aligned} f_m &= \frac{R_{cr}}{2} \cdot \sin(\theta) \\ f_s &= \frac{R_{cr}}{2} \cdot \frac{1}{\sin(\theta)}. \end{aligned} \quad (4.2)$$

Together with the lens equation

$$\frac{1}{f} = \frac{1}{a} + \frac{1}{b} \quad (4.3)$$

and with a crystal-detector-distance  $a = R_{cr} \cdot \sin(\theta)$  it follows for the meridional and sagittal focal distances:

$$\begin{aligned} b_m &= R_{cr} \cdot \sin(\theta) = a \\ b_s &= -\frac{b_m}{\cos(2 \cdot \theta)} = -R_{cr} \cdot \frac{\sin(\theta)}{\cos(2 \cdot \theta)}, \end{aligned} \quad (4.4)$$

respectively. Based on these relations and with the help of several detectors a spatially resolving device can be designed according to the illustration in figure 4.3. Each detector is placed at a certain position on the Rowland sphere  $B_{rw}$  of the spherically bent crystal<sup>1</sup>. Together with the crystal the detectors then define individual Rowland circles  $C_{rw}$  with  $C_{rw} \in B_{rw}$ . As the angle of incidence equals the angle of reflection, each Rowland circle corresponds to one line of sight. If arranged in a vertical array, the detectors define lines of sight that are vertically distributed over the minor plasma radius. Instead of several single detectors a big one piece detector can be used. The dispersion information is then resolved in horizontal direction and the spatial information is resolved in vertical direction.

It shall be emphasized that this design especially benefits from the astigmatic depiction errors of spherically bent crystals. On the image side the detectors are placed on the Rowland circle that is determined by the meridional focus (perpendicular to the dispersion direction). Whereas on the object side the plasma is located close to the sagittal focal distance  $b_s$ , so that the detectors see horizontal, narrow lines of the plasma at different vertical positions. The horizontal viewing angle is determined by the degree of defocusing in the meridional plane. A further advantage of this design are significantly smaller unit dimensions, due to  $f_m < f_s$  and  $b_m < b_s$ . Spherically bent Bragg-crystals for plasma spectroscopy were introduced and discussed by Bitter et al. [51, 52].

#### 4.2.2 The High Resolution X-ray Spectrometer (HRS)

The HRS device (**H**igh **R**esolution **B**ragg **S**pectrometer) is a two channel Johann type spectrometer with a variable wavelength range. The two channels use individual Bragg crystals so that the HRS unit actually consists of two independent spectrometers. Both of them observe the plasma plasma center along almost identical chords that are tilted against the major radius of TEXTOR by an angle of  $10^\circ$ . Furthermore, the lines-of-sight cross the beam line of the neutral particle injector NBI-1 (see figure 4.1(a)).

Developed for the investigation of polarization effects in X-ray spectra, the two channels have perpendicular directions of dispersion. The dispersion plane of channel 1 is oriented horizontally, while that of channel 2 lies vertically, which means parallel to the toroidal axis of TEXTOR. A schematic of the HRS device is shown in figure 4.5(a). It shall be emphasized that the HRS device does not provide any radial resolution. Both channels are equipped with quartz crystals in 110-orientation with a lattice constant of  $2d = 4.9079 \text{ \AA}$ [53]. The radii of curvature are  $R_{cr} = 3820 \text{ mm}$  for the horizontal and  $R_{cr} = 4630 \text{ mm}$  for the vertical crystal. Both channels are equipped with 1-dimensional

<sup>1</sup>Due to axis symmetry a spherically bend crystal has a Rowland sphere  $B_{rw}$ .

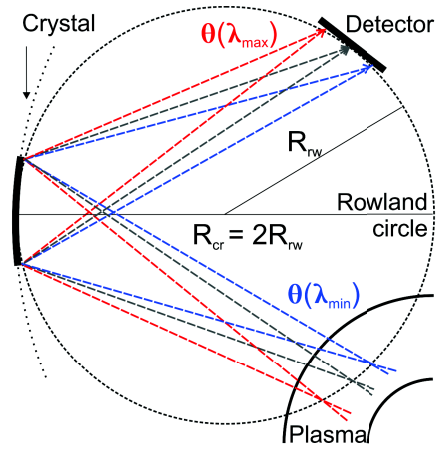


Figure 4.2: Principle of a Bragg spectrometer in Johann design based on a cylindrically bent crystal. The cylinder focuses perpendicularly to the axis of curvature. In order to achieve sharp spectral lines, the detector is placed on the Rowland circle.

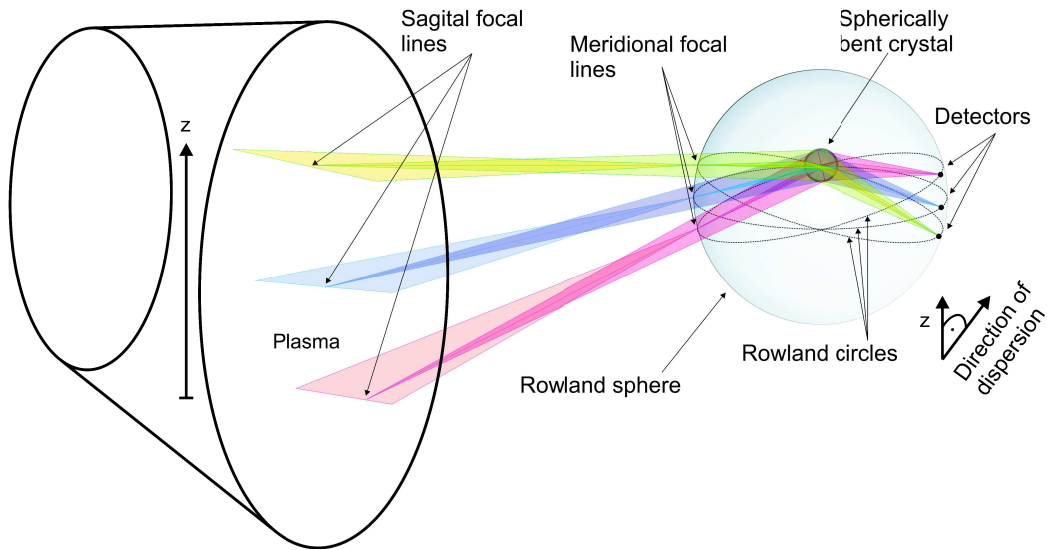


Figure 4.3: Principle of a spatially resolving Bragg spectrometer based on one spherically bent crystal. The spectral and spatial information are resolved in horizontal and vertical direction, respectively.

multiwire proportionality counters with an active area of  $180 \text{ mm} \times 90 \text{ mm}$  and a spatial resolution of about  $0.4 \text{ mm}$  in direction of dispersion. The distances between the crystals and the plasma center are  $4300 \text{ mm}$  for the horizontal channel and  $5035 \text{ mm}$  for the vertical channel, while the crystal-detector distance is  $3050 \text{ mm}$  and  $2950 \text{ mm}$ , respectively. During the experiments discussed in this thesis the horizontal channel was set to the wavelength region around  $4 \text{ \AA}$  to observe the  $K_\alpha$ -spectrum of He-like argon. The vertical channel was set to observe the ground state transitions of the high Rydberg states of He-like argon ( $1snp - 1s^2$ ) at about  $3 \text{ \AA}$ . With the above mentioned lattice constant this corresponds to a Bragg angles of ca.  $54^\circ$  and  $38^\circ$ , respectively. Further details concerning the specifications of the HRS spectrometer can be found in [54].

### 4.2.3 The compact imaging Bragg spectrometer

The imaging Bragg spectrometer [55] was developed at FZ-Jülich for ion and electron temperature measurements at the stellarator W7-X. Before delivery it was installed at TEXTOR for a short commissioning phase.

The spectrometer is designed for measuring the He-like  $K_\alpha$ -spectra of mid  $z$  impurity elements between argon and copper. In the current setting it is equipped with a circular quartz crystal cut in 110-orientation ( $2d = 4.9079 \text{ \AA}$ ) in order to observe the  $K_\alpha$ -emission of He-like argon (ca.  $4 \text{ \AA}$ ) at a Bragg angle of ca.  $54^\circ$ . The crystal has a diameter of  $d_{cr} = 80 \text{ mm}$  and is spherically bent with a curvature radius of  $R_{cr} = 1584.6 \text{ mm}$  (see figure 4.4(a)). This corresponds to a Rowland radius of  $R_{rw} = R_{cr}/2 = 792.3 \text{ mm}$ .

An array of six 2-dimensional CCD detector chips (figure 4.4(b)) is placed on the Rowland sphere at an image distance of  $a = R_{cr} \cdot \sin(54^\circ) = 1282.0 \text{ mm}$ . Their lines-of-sight are vertically distributed over the minor radius of TEXTOR and are tilted by an angle of  $20^\circ$  relative to the major radius of TEXTOR. The detectors are mounted on a curved attachment to adapt the shape of the Rowland sphere. This ensures optimal focusing for all CCDs. However, due to their flat surfaces on each chip only one wavelength can be in optimal focus at a time. One CCD has an active area of  $26.6 \text{ mm} \times 6.7 \text{ mm}$  (horizontal dispersion direction  $\times$  vertical height) hosting  $1024 \times 256$  pixels. During the commissioning phase at TEXTOR a maximum of five chips were operational at a time - during most discharges only four or less. The 2-dimensional raw data provided by the detectors is shown in figure 4.5(b). The time resolution was limited to  $700 \text{ ms}$  due to technical issues with the data acquisition system. In the presented experiments the spectra have been integrated over the whole flat top phase of a discharge to improve statistics. In some cases it was integrated over multiple discharges.

### 4.2.4 Calibration of the W7-X imaging spectrometer

For X-ray imaging experiments the exact vertical positions of the lines-of-sight are of crucial importance. Therefore, the lines-of-sight were analyzed via physical ray tracing. Another important issue is the focusing of the spectral lines, especially in regard to ion temperature measurements. Both procedures are discussed below.

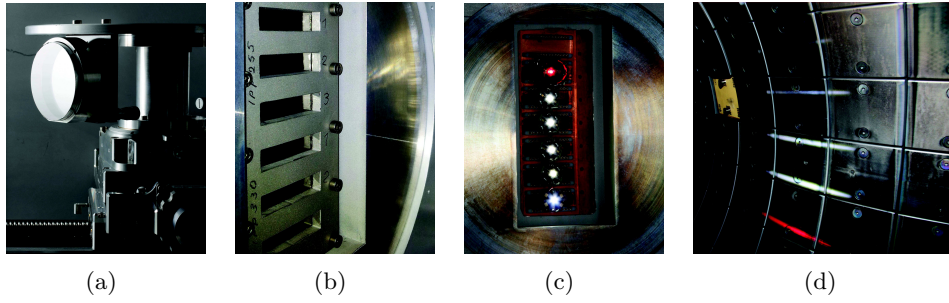


Figure 4.4: **a)** Spherically bent crystal of the W7-X imaging Bragg spectrometer (110, quartz, 80 mm diameter,  $R_{cr} = 1584.6$  mm) **b)** CCD detector array of the W7-X imaging Bragg spectrometer, consisting of 6 2-dimensional chips **c)** LED array for physical ray tracing **d)** The image of the LED array projected on the high field side wall tiles of TEXTOR.

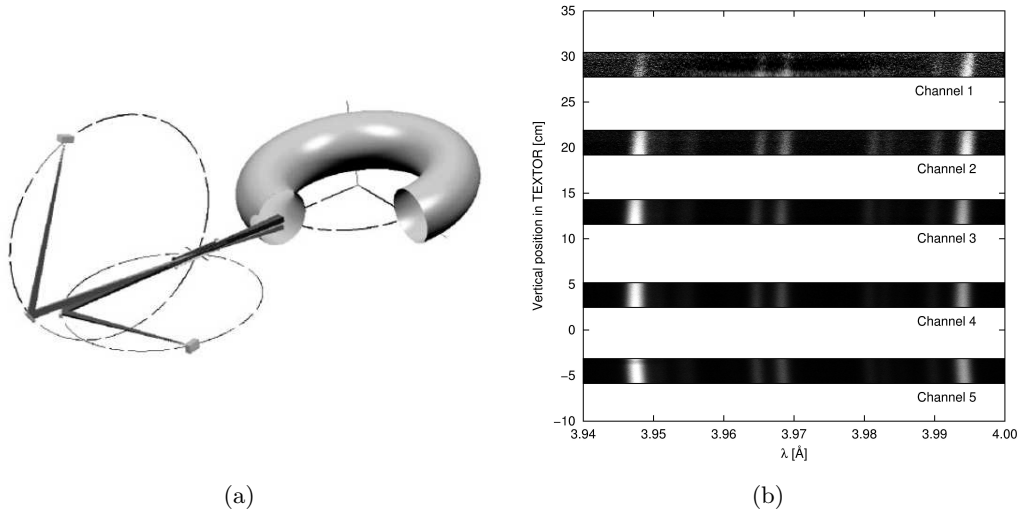


Figure 4.5: **a)** Schematic of the two channel X-ray spectrometer (HRS). Reprinted with permission from Weinheimer et al. Rev. Sci. Instrum. 72, 2566 (2001). Copyright 2014, AIP Publishing LLC. **b)** Spectral images provided by the detector array of the W7-X spectrometer during a TEXTOR discharge. The ordinate indicates the vertical coverage of the poloidal plasma cross section in true scale.

Crystal position	Ch. 1	Ch. 2	Ch. 3	Ch. 4	Ch. 5	Ch. 6
[mm]	[mm relative to equatorial plane of TEXTOR]					
0	243	160	80	-10	-90	-180
10	310	210	123	40	-40	-125
20	cut	260	180	90	10	-85

Table 4.1: Vertical positions of the spectrometer’s lines-of-sight determined by physical ray tracing for three different vertical crystal positions. The crystal was shifted in vertical height using underlayments of 10 *mm* or 20 *mm* in order to vary the vertical positions of the lines-of-sight. During the measurements presented in this thesis the spectrometer was operated with the 10 *mm* underlayment only. The listed values represent the vertical mid position of each detector.

**Vertical positioning of the lines of sight** The CCDs chips in the detector array are placed in vertical distances of  $d_i = 19 \text{ mm}$  (figure 4.4(b)). In order to determine the corresponding vertical spacing of the lines of sight in the TEXTOR vessel, a backwards ray tracing experiment is performed. For this purpose an LED-array is installed in place of the detector array. The emitted light is reflected by the crystal towards the TEXTOR vessel and according to its depiction properties the LEDs are imaged on the high field side tiles as shown in figures 4.4(c) and 4.4(d). The vertical positions determined this way are listed in table 4.1. The table includes values for three different vertical positions of the crystal. The averaged reproduction scale derived from the observed LED images is  $\gamma = 4.5$ . According to this each chip ( $h = 0.67 \text{ mm}$ ) covers 30.0 *mm* of vertical height in the plasma. The LED images at the high field side wall have a horizontal width of ca. 15 *cm*. As the LEDs can approximately be considered as point sources, these 15 *cm* correspond to the horizontal viewing angle per wavelength.

**Focusing of the spectral lines** The ion temperature  $T_i$  is deduced from the Doppler broadening of the spectral lines. Therefore, the instrumental broadening needs to be investigated in detail. Besides the minimal instrumental line width line broadening due to defocusing has to be taken into account. In the following the experimental focusing of the spectral lines and the modeling of the minimal instrumental line width are discussed.

Prior to the experiments the optimal crystal position is determined in order to achieve optimally focused spectral lines. For this purpose spectra are recorded during a series of identical ohmic discharges. On a shot to shot basis the crystal-detector distance is varied over a range of several *cm* by moving the crystal stepwise within the horizontal plane keeping the Bragg angle constant.

The **w**-line and the **z**-line represent the high and low energy end of the observed spectral interval. They are analyzed in terms of their line width for each crystal position. In figure 4.6(a) both lines show clear points of minimal line broadening. However, due to the circular focal line (Rowland circle) and the flat detector chips only one wavelength

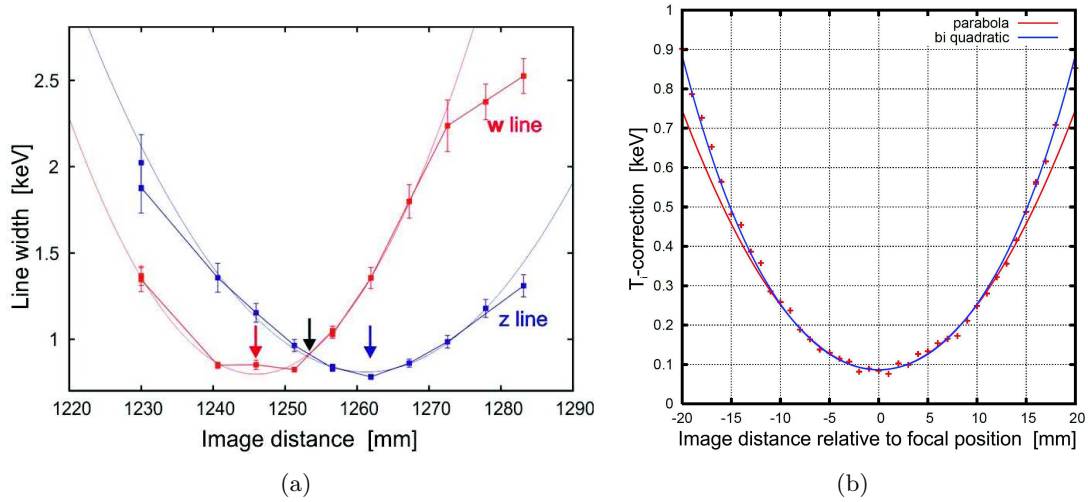


Figure 4.6: **a)** Broadening of the **w**-line and the **z**-line as a function of the crystal-detector-distance. The line widths are interpreted in terms of the ion temperature. Each data point is measured on a shot-to-shot basis during identical ohmic discharges in TEXTOR. The arrows in red and blue indicate the focal positions for **w** and **z**. For further experiments the focus is set into the center of the spectral interval marked by the black arrow. **b)** Modeled line broadening due to defocusing and depiction errors. The minimal instrumental line width corresponds to 90 eV. The plot is taken from [56].

can be in focus at a time. The optimal crystal positions for **w** and **z** differ by about 17 mm. To obtain most homogeneous line widths over the entire spectrum, the focus is set right between **w** and **z**. Thus, the lines **x** and **y** are closest to optimal focusing. According to figure 4.6(a) the line broadening due to defocusing corresponds to an offset in the ion temperature of  $\Delta T_i^{fc} = 150$  eV for **w** and **z**, respectively.

However, the minimal instrumental line width in the focal position is not resolved by the experiment discussed above. It is generally difficult to measure. Therefore, Monte Carlo ray tracing has been performed in order to model the spectrometer's depiction properties [56]. The XTRACK code [57] was used that simulates the Bragg reflection at spherically bent crystal surfaces. Within the model the ideal profile of a spectral line is defined by the rocking curve of the 110-quartz crystal (black curves in figure 4.7(a)). The simulated imaged line profiles show asymmetric depiction errors arising from the spherical curvature of the crystal surface (red points in figure 4.7(a)). These errors become more prominent when the spectral lines are out of focus, as shown in the right plot in figure 4.7(a). To determine the effective line broadening caused by the depiction errors, the simulated line images are convoluted with a Gaussian component corresponding to an argon ion temperature of 800 eV. Afterwards the resulting profile shape is fitted using a Voigt profile, while the Lorentzian component is fixed to a fit of the initial line shape (see figure 4.7(b)). For optimally focused lines the evaluation of the

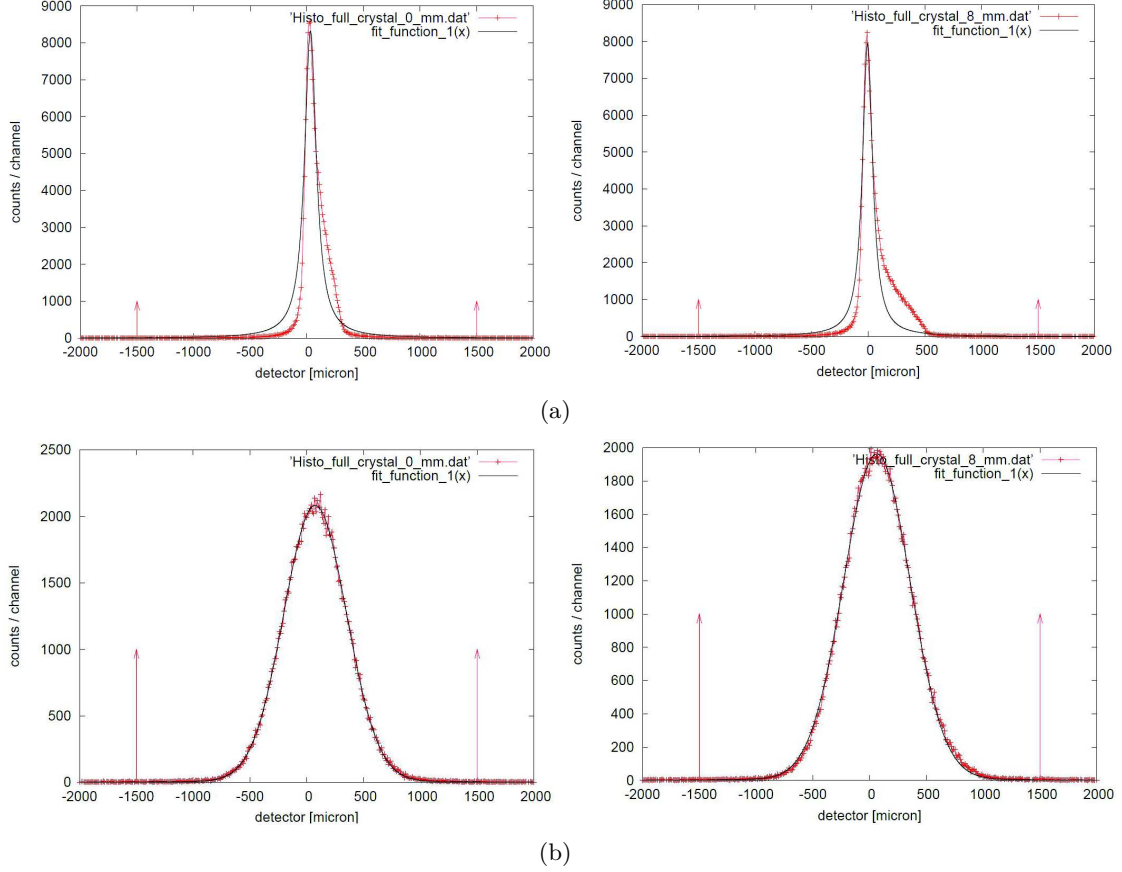


Figure 4.7: **a)** Modeled imaging quality of the spherically bent Bragg crystal for two different focal positions. (**Left:** Line in focus, **Right:** Line out of focus by 8 mm) The initial Lorentzian line profiles and their images are shown in black and red, respectively. The asymmetric depiction errors become stronger as the spectral line moves out of focus. **b)** Gaussian fit (black) of the Doppler broadened line images shown in (a) (red). All plots are taken from [56].

Voigt fit gives back an ion temperature of  $T_i \approx 890 \text{ eV}$ . Hence, the modeled instrumental line width corresponds to an offset in the ion temperature of  $\Delta T_i \approx 90 \text{ eV}$ . For lines that are out focus the modeling procedure gives higher temperature offsets, as shown in figure 4.6(b). Figure 4.6(b) shows the ion temperature offsets as a function of the image distance relative to the focal position. The plot is equivalent to the experimental data shown in figure 4.6(a). The modeled and measured line broadening due to defocusing agree within a tolerance of ca.  $10 \text{ eV}$ . The good agreement gives confidence in the modeled minimal instrumental line width ( $\Delta T_i \approx 90 \text{ eV}$ ).

For ion temperature measurements the offsets caused by the instrumental line broadening need to be subtracted. The correction function  $\Delta T_i(\lambda)$  is plotted in figure 4.8. The

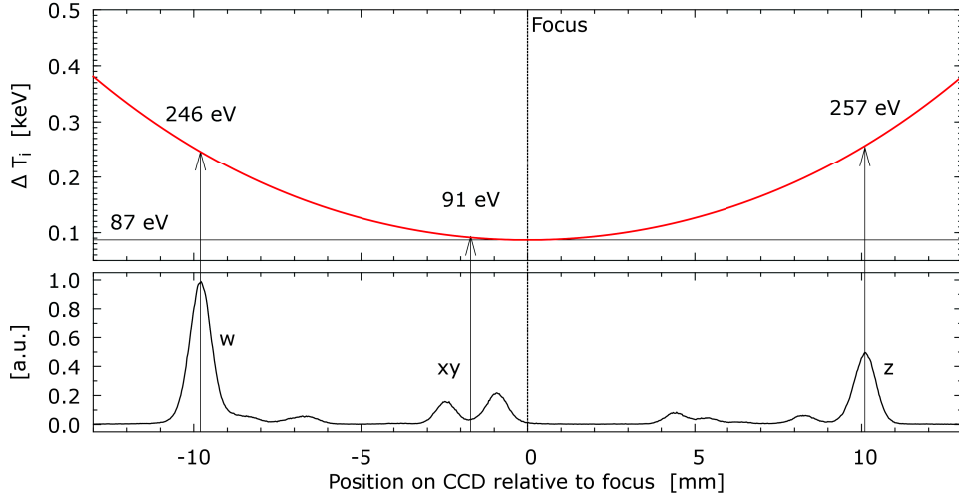


Figure 4.8: The  $\Delta T_i(\lambda)$  correction function to account for the effective instrumental broadening of the spectral lines. Shown is the bi-quadratic fit from figure 4.6(b). The minimal line width corresponds to an offset of roughly 90 eV.

correct ion temperature obtained from the line width of **w** or **z** is:

$$T_i = T_i^{raw} - 250 \text{ eV} \pm 25 \text{ eV}. \quad (4.5)$$

The accuracy in  $\Delta T_i(\lambda)$  is estimated to  $\pm 25 \text{ eV}$ .

# 5 Charge exchange and impurity transport studies based on radially resolved $K_\alpha$ -spectra of He-like argon

$K_\alpha$ -spectroscopy on mid  $z$  He-like impurity elements is an established tool for electron and ion temperature measurements in hot fusion plasmas. With new generation imaging devices spatial resolution is achieved. Yet radial scans of the  $K_\alpha$ -emission do not only provide temperature profiles, but also give access to quantities, that cannot be resolved in 1D-measurements.

In this chapter a new technique is discussed, that allows to measure the neutral particle density as well as the impurity transport based on  $K_\alpha$ -imaging. This not only pushes forwards the possibilities of X-ray spectroscopy, but also resolves a long standing discrepancy concerning the radial behavior of the  $K_\alpha$ -line ratios.

## 5.1 Experimental data

During the commissioning phase of the W7-X imaging X-ray spectrometer (described in section 4.2.3) at TEXTOR, the  $K_\alpha$ -emission of He-like argon could be measured in several ohmic and neutral beam heated discharges. The recorded spectra are the first radially resolved X-ray data from TEXTOR. In the following the experimental data are presented and discussed qualitatively. The global plasma parameters of all discharges analyzed in this chapter are listed in table 5.1.

The four plots in figure 5.1(a) show the radial scan of the  $K_\alpha$ -spectrum of He-like argon, going stepwise from the center most chord (top) at  $z = 4 \text{ cm}$  to the outer most chord (bottom) at  $z = 31 \text{ cm}$  above the equatorial plane. On the central channels the  $\mathbf{w}$ -line clearly dominates the spectrum, as it is well known from widely used 1D X-ray diagnostics observing the plasma center. However, as the lines of sight move outwards, the triplet lines  $\mathbf{x}$ ,  $\mathbf{y}$  and  $\mathbf{z}$  gain intensity relative to  $\mathbf{w}$ , so that at  $31 \text{ cm}$  off center  $\mathbf{z}$  exceeds  $\mathbf{w}$  by a factor of 2. The overall brightness strongly decreases towards the plasma edge, as shown in figure 5.1(b). This observation is in qualitative agreement with earlier findings from the tokamak ALCATOR reported by Rice et al. [40]. For comparison this data is shown in figure 5.2. Although ALCATOR is nowadays equipped with an imaging X-ray spectrometer, this data was obtained on a shot to shot basis by tilting the line of sight of a single channel device. The  $K_\alpha$ -line ratios observed at TEXTOR and ALCATOR deviate severely from the theoretical predictions from the corona approximation. As already mentioned by Rice, the increasing triplet lines indicate stronger recombination contributions at the plasma edge. However, significant recombination contributions to

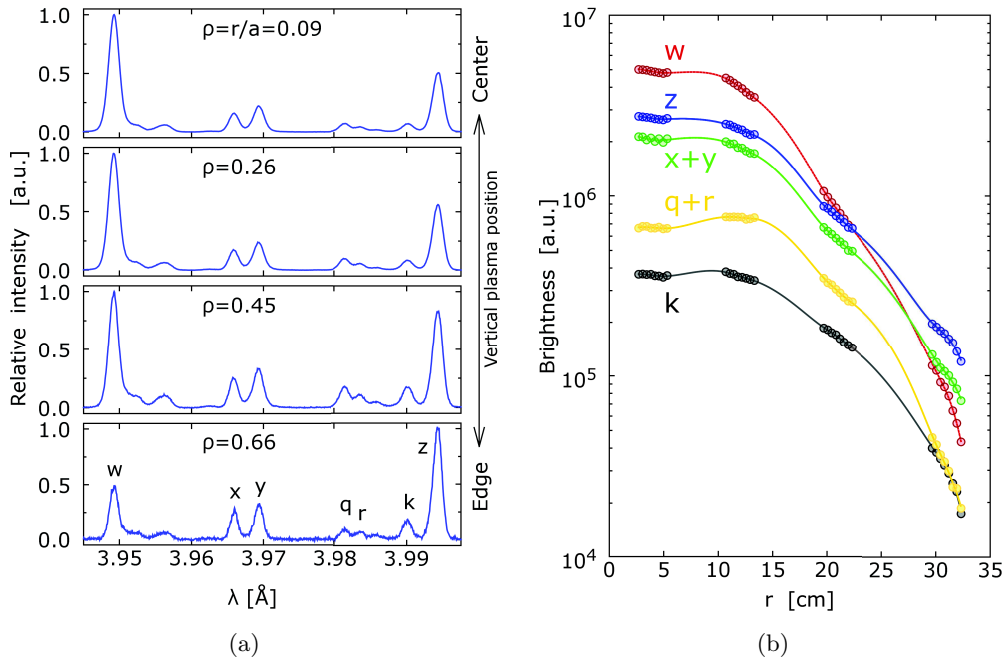


Figure 5.1: **a)** Radially resolved X-ray emission of He-like argon close to 4 Å measured during an ohmic discharge in TEXTOR (#116926,  $\bar{n}_e = 2.5 \cdot 10^{13} \text{ cm}^{-3}$ ). **b)** Radial profiles of the absolute line intensities.

the He-like argon lines necessitate the abundance of H-like argon, which under coronal conditions should not exist at the colder plasma edge, where  $T_e \leq 500 \text{ eV}$ . This means that no matter what kind of recombination processes are involved, they act in combination with substantial degrees of impurity transport, bringing H-like argon from the hot plasma center towards the edge region. Rice applied anomalous impurity transport coefficients, which strongly affected the coronal argon ion distribution profiles, to model the experimentally found line ratios. Still, it was not possible to reconstruct the data without arbitrarily increasing the rates of radiative recombination by a factor of five. Based on the ALCATOR data, Kato et al. [58] performed detailed calculations concerning the influence of charge exchange recombination on the  $K_\alpha$ -spectrum as well as on the  $1snl - 1s^2$ -transitions of He-like argon. However, the observed  $K_\alpha$ -spectra could not entirely be described.

In order to quantify the deviations from the corona values, the spectra are evaluated in terms of the argon ion ratios. The applied procedure is described in section 3.3.1. Figure 5.3(a) shows radial profiles of the ratio  $Ar \text{ XVI} / Ar \text{ XVII}$  and the ratio  $Ar \text{ XVIII} / Ar \text{ XVII}$  for several ohmic discharges with different plasma densities. For the analysis coronal conditions were assumed<sup>1</sup>, and the displayed ion density ratios are normalized on the

<sup>1</sup>The forward integration, that is performed to take into account the sight-line integrated measurement,

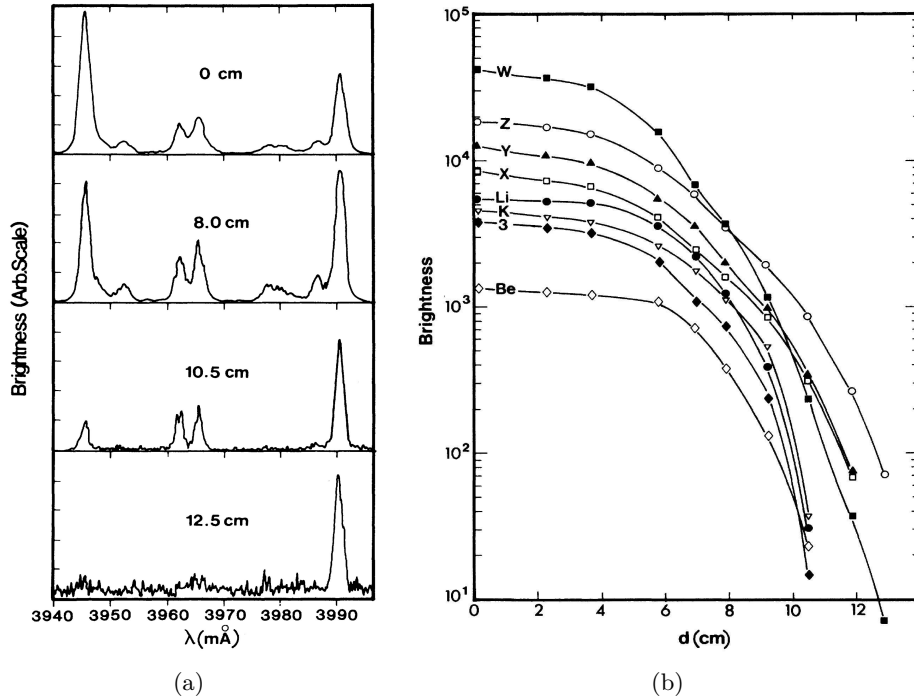


Figure 5.2: X-ray emission of He-like argon measured at different radial positions in ALCATOR. ALCATOR is a limiter tokamak with a minor plasma radius of  $a = 12.5 \text{ cm}$ . Reprinted figures with permission from Rice et al., Phys. Rev. A: At., Mol., Opt. Phys. 35, 7, 3033 (1987). Copyright (2014) by the American Physical Society.

coronal reference values. In the plasma center the observed  $Ar\text{ XVIII} / Ar\text{ XVII}$  is slightly lower than the reference, but increases dramatically towards the edge, so that it exceeds the corona value by up to a factor of 1000 on the outer most channel. This behavior mirrors the increasing triplet lines in figure 5.1(a). The discrepancies in  $Ar\text{ XVI} / Ar\text{ XVII}$  are much more moderate and for all data points below a factor of five. It is generally shifted towards the Li-like argon stage. For all discharges a similar radial behavior is observed, showing a maximum deviation around half the plasma radius that reduces towards either sides. From about  $5 \text{ cm}$  off center and further inwards the normalized ratio  $Ar\text{ XVI} / Ar\text{ XVII}$  converges to a minimum value that is always above one. The deviation from the corona values increases towards lower plasma densities.

From figure 5.3(a) it is clear that the corona approximation is strongly violated for TEXTOR plasmas. But the two plots further allow to make some qualitative conclusions concerning the possible roles of impurity transport and charge exchange in this respect. The non monotonic radial behavior of  $Ar\text{ XVI} / Ar\text{ XVII}$  cannot be caused by charge

---

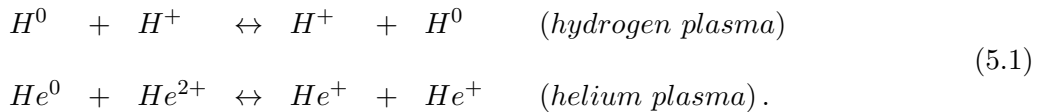
is based on the corona distribution of the argon ion stages. No charge exchange contributions are included.

TEXTOR Discharge	$\bar{n}_e$ [ $10^{13} \text{ cm}^{-3}$ ]	$\hat{T}_e$ [keV]	$\hat{T}_i$ [keV]	$B_T$ [T]	$I_p$ [kA]	Working gas
116921	1.5	1.85	0.95	2.25	350	H
116923	2.0	1.37	0.83	2.25	350	H
116924	2.0	1.70	1.04	2.25	350	H
116926	2.5	1.58	1.07	2.25	350	H
116925	3.0	1.37	0.97	2.25	350	H
116778	2.5	1.33	1.29	1.90	350	<b>He</b>
116838	2.5	1.40	1.00	2.25	350	H

Table 5.1: Main plasma parameters of all TEXTOR discharges discussed in this chapter.

exchange, as the neutral particle density has to decay monotonically towards the plasma center. Therefore, it must mainly be caused by radial transport, increasing the amount of *Ar XVI* in the center region. The same holds for the ratio *Ar XVIII* / *Ar XVII*. It is determined from the recombination part of the He-like lines (**w**, **x**, **y**, **z**) and it was already mentioned that the strongly increased values at the plasma edge must involve transport effects, which bring *Ar XVIII* from the plasma center towards the edge. It can further be concluded that the transport is mainly diffusive, as the ratio *Ar XVI* / *Ar XVII* is apparently affected by an inwards flux of *Ar XVI*, while the ratio *Ar XVIII* / *Ar XVII* clearly shows an outwards flux of *Ar XVIII*. This is in agreement with the contrarious radial gradients in the coronal ion density profiles  $N(\text{Ar XVI})(r)$  and  $N(\text{Ar XVIII})(r)$  that lead to different directions of the diffusive, radial flux (compare figure 3.4(b) on page 22). However, the gradient in  $N(\text{Ar XVI})(r)$  is not as steep as in case of  $N(\text{Ar XVIII})(r)$ . Therefore, the effect of diffusive transport is weaker, and the observed deviations are less severe. These qualitative considerations are contradictory to Rosmej et al. [47], who deduced low diffusion coefficients from X-ray spectra measured in TEXTOR (compare section 3.3).

The role of charge exchange is difficult to judge from figure 5.3(a). Instead it can be estimated by comparing spectra measured in helium and hydrogen working gas. In helium plasmas the neutral particle density arising from recycling processes at the plasma wall is generally much lower than in hydrogen plasmas. This is due to the fact that charge exchange collisions with  $\text{He}^{2+}$  ions do not result in atomic helium:



Therefore, the charge exchange interactions do no longer represent random walk collisions for neutral particles, but a loss channel. As a consequence, the penetration depth of neutral particles in helium plasmas is strongly reduced. Analogous to figure 5.3(a), figure 5.3(b) compares the argon ion ratios obtained from spectra that were measured during discharges in helium and hydrogen plasma, respectively. The ratio *Ar XVI* / *Ar XVII* measured in helium plasma shows approximately the same radial characteristics as the

equivalent measured in hydrogen plasma, but a significantly lower overall deviation from the corona values. On the one hand, the similar radial gradients speak for similar impurity transport behavior in helium and hydrogen plasmas. On the other hand, the constant offset in  $Ar\text{ XVI} / Ar\text{ XVII}$  must be connected to charge exchange, shifting the argon ion balance towards the lower ion stages. As in helium plasma the neutral particle background is reduced, the deviation from the corona values is generally smaller. In the ratio  $Ar\text{ XVIII} / Ar\text{ XVII}$  no significant differences are visible, which suggests that the deviations from the corona values are obviously dominated by impurity transport. With these findings in mind we can look back to figure 5.3(a). The density dependence of the deviations from the corona values in  $Ar\text{ XVI} / Ar\text{ XVII}$  can now be assigned to charge exchange. The deviations increase towards lower plasma densities indicating higher neutral particle densities. This is consistent with a bigger penetration depth for neutral particles at lower plasma densities.

## 5.2 Data analysis

The qualitative discussion of the experimental data already gave strong evidence that the observed deviations from the corona model can be explained by radial impurity transport and charge exchange recombination. For a quantitative analysis the corona model of the argon ion distribution needs to be extended by radial impurity transport and charge exchange recombination. The aim is to reproduce the spectral line ratios consistently along the entire plasma radius.

For this purpose a 1D-impurity-transport-model is used to reconstruct the argon ion ratios obtained from the spectra. The transport-model calculates the relative argon ion distribution ( $Ar^{q+}(r)$ ,  $0 \leq q \leq 18$ ,  $\sum_{q=0}^{18} N(Ar^{q+})(r) = 1$ ), based on given radial profiles of the plasma density ( $n_e(r)$ ) and the plasma temperature ( $T_e(r)$ ,  $T_i(r)$ ). To include charge exchange recombination further the neutral particle density profile  $n_0(r)$  is required. Radial impurity transport is considered to be mainly diffusive and scales with the radial diffusion coefficient  $D_{\perp}(r)$ , which as well is needed as input data. A convective transport component is also taken into account, while for the convection coefficient  $v_{\perp}$  the common scaling  $v_{\perp} \propto \frac{r}{a} \cdot D_{\perp}$  [2] is used. The impurity transport model is discussed in section 5.2.2.

In a manual fit process  $n_0(r)$  and  $D_{\perp}(r)$  are chosen to give the best possible agreement between the modeled argon ion ratios and their equivalents obtained from the  $K_{\alpha}$ -spectra. This means, the discrepancies in  $Ar\text{ XVIII} / Ar\text{ XVII}$  and  $Ar\text{ XVI} / Ar\text{ XVII}$  are minimized along the entire radial field of view. Once a set of  $n_0(r)$  and  $D_{\perp}(r)$  is found that adequately reproduces the argon ion ratios, the above-mentioned forward integration has to be performed again based on the modeled ion distribution and the applied neutral density profile  $n_0(r)$ . This is important to ensure consistency between the modeling and the fit of the spectra, and will result in slightly changed values for  $Ar\text{ XVI} / Ar\text{ XVII}$  and  $Ar\text{ XVIII} / Ar\text{ XVII}$ , so that in the transport calculations  $n_0(r)$  and  $D_{\perp}(r)$  have to be adapted. This leads to an iterative procedure that comes to an end as soon as self-consistency between the fitted spectra and the transport code is

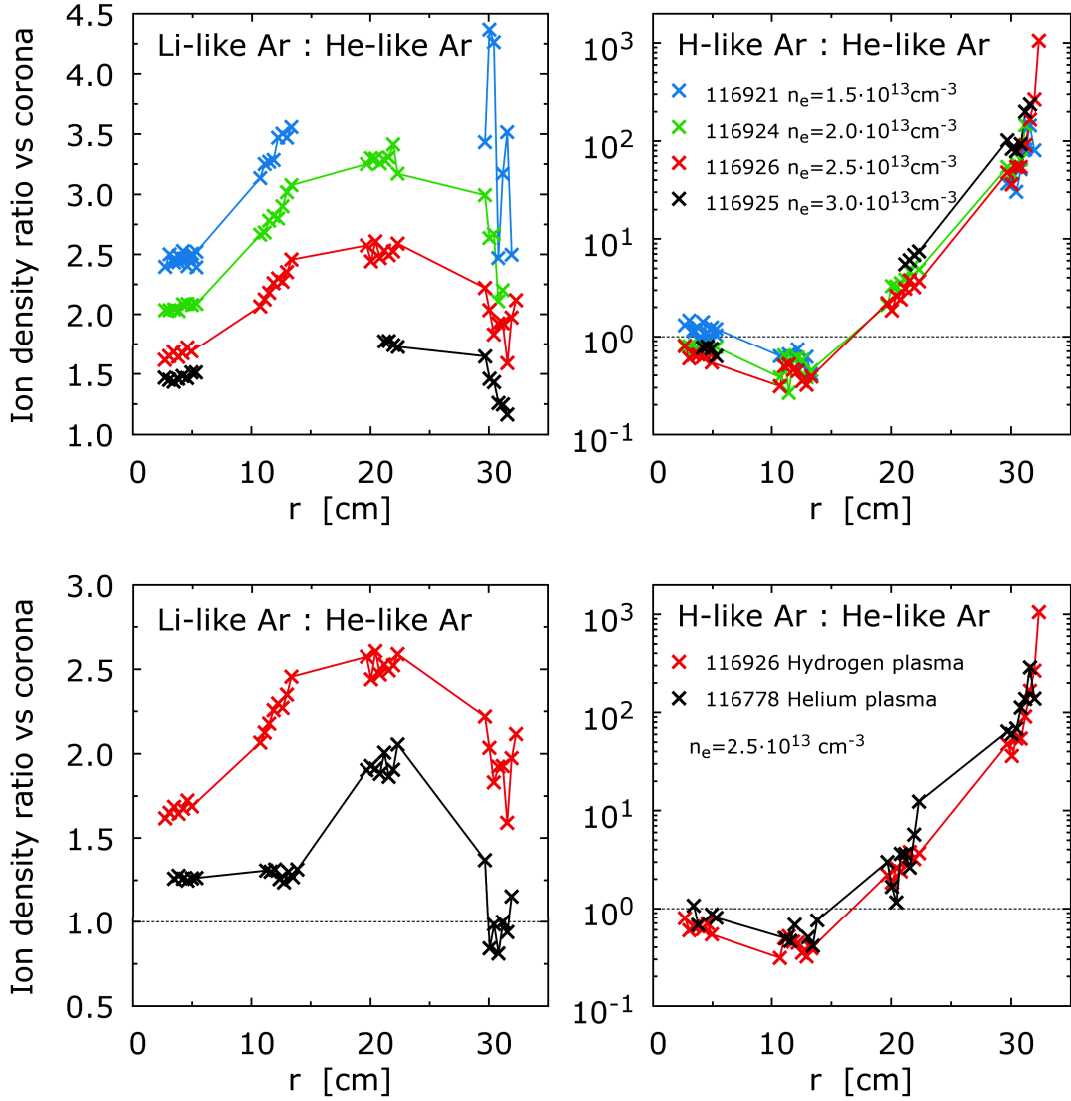


Figure 5.3: The argon ion ratios  $Ar\text{ XVI} / Ar\text{ XVII}$  and  $Ar\text{ XVIII} / Ar\text{ XVII}$  determined from the radially resolved  $K_\alpha$ -spectra under assumption of coronal conditions. The obtained ion ratios are normalized on the corona values. Missing data points are due to technical reasons. **a)** Subsequent ohmic discharges with increasing plasma density. **b)** Ohmic discharges in hydrogen and helium working gas at equal plasma density. The data points with  $r < 15$  cm in the helium discharge were measured below the equatorial plane ( $r < 0$  cm).

achieved. The argon ion ratios  $Ar\text{ XVI} / Ar\text{ XVII}(r)$  and  $Ar\text{ XVIII} / Ar\text{ XVII}(r)$ , the temperatures  $T_e(r)$  and  $T_i(r)$  as well as  $n_0(r)$  and  $D_{\perp}(r)$  are then considered as experimental results. This analysis allows for unique solutions, as the obtained  $T_{e/i}$ -values only weakly depend on the argon ion distribution, applied in the forward integration.

Inspired by earlier experimental results from TEXTOR [31] and other tokamaks, the diffusion coefficient  $D_{\perp}(r)$  is expressed by a variable number of smooth step functions of the kind

$$d(r) = \frac{1}{1 + e^{\kappa \cdot r}}, \quad (5.2)$$

where the parameter  $\kappa$  controls the steepness of the edges. Each step is variable in the absolute level and the radial position. During the manual fit procedure the number of steps in  $D_{\perp}(r)$  is kept as low as possible. Usually two or three steps are sufficient.

The neutral particle density  $n_0(r)$  is not handled as a free function. Instead a 1D-model for diffusive neutral particle transport is applied to calculate the steady state density distribution  $\tilde{n}_0(r)$  for a constant inwards flux of hydrogen coming from the plasma wall.  $\tilde{n}_0(r)$  is calculated depending on the plasma parameters  $n_e(r)$ ,  $T_e(r)$  and  $T_i(r)$  of the considered discharge and is then scaled by one scalar parameter  $N_0$ :

$$n_0(r) = N_0 \cdot \tilde{n}_0(r). \quad (5.3)$$

This on the one hand reduces complexity of the problem and on the other hand gives a physical motivation for the shape of  $n_0(r)$  and at the same time represents an experimental verification of the neutral particle transport model. The neutral particle transport model is discussed in more detail in 5.2.3.

### 5.2.1 Effects of charge exchange and transport on the argon spectrum

To analyze the  $K_{\alpha}$ -spectra in terms of charge exchange and impurity transport, the ability to distinguish both effects in the line ratios is of crucial importance. Both, charge exchange and transport affect the argon ion distribution in a similar way, which might put into question the existence of a unique solution. However, as discussed in [59], principle differences between the He-like  $1s2l - 1s^2$  transitions and their Li-like satellites allow a clear distinction of the two effects.

Charge exchange represents an additional recombination channel and shifts the argon ion balance towards the lower ionization stages. Therefore, it affects all measured line intensities indirectly by changing the ground state abundance of each ion stage:

$$\frac{N_z}{N_{z+1}} = \frac{\langle \sigma_{rr} \cdot v \rangle + \langle \sigma_{dr} \cdot v \rangle + \frac{n_0}{n_e} \cdot \langle \sigma_{cx} \cdot v \rangle}{\langle \sigma_{ion} \cdot v \rangle}. \quad (5.4)$$

At the same time, charge exchange preferably populates highly excited states of the recombining ion, and the consecutive radiative decay causes cascade contributions to the  $1s2l - 1s^2$  transitions (**w**, **x**, **y** and **z**). However, this does not hold for the satellite lines, which all correspond to transitions from doubly excited Li-like states. As the

fraction of (singly) excited ions is very small compared to the ground state densities (low density limit, see section 3.1.2), the population of doubly excited states by charge exchange is negligible. Hence, the satellites do not receive relevant cascade contributions from charge exchange recombination. For comparison the terms for the intensities of the satellites **k** and **q** and for the **w**-line are repeated here:

$$\begin{aligned}
I_k &\propto \int_0^1 N(\text{Ar } XVII)(\rho) \cdot Q_{dr,k}(\rho) \cdot n_e(\rho) \cdot d\rho' \\
I_q &\propto \int_0^1 \left( N(\text{Ar } XVI)(\rho) \cdot Q_{iexc,q}(\rho) + N(\text{Ar } XVII)(\rho) \cdot Q_{dr,q}(\rho) \right) \cdot n_e(\rho) \cdot d\rho' \\
I_w &\propto \int_0^1 \left[ N(\text{Ar } XVII)(\rho) \cdot Q_{exc,w}(\rho) \cdot n_e(\rho) \right. \\
&\quad \left. + N(\text{Ar } XVIII)(\rho) \cdot \left( Q_{rec,w}(\rho) \cdot n_e(\rho) + Q_{cx,w}(\rho) \cdot n_0 \right) \right] \cdot d\rho'.
\end{aligned} \tag{5.5}$$

Also transport changes the radial argon ion distribution. However, particle transport processes occur on much greater time scales than the decay of the excited ion states. Therefore, transport does not have direct influence on the population densities of the excited states, and only affects the radial distribution of the ground states. To illustrate this, the characteristic time of particle transport  $\tau_{\perp}$  can be estimated from the poloidal plasma dimensions in TEXTOR and the diffusion coefficient [25]. With an anomalous transport coefficient in the order of  $D_{\perp} = 1 \text{ m}^2/\text{s}$  (as generally observed) it follows:

$$\tau_{\perp} = \frac{a^2}{D_{\perp}} = \frac{(0.47 \text{ m})^2}{1 \text{ m}^2/\text{s}} \approx 0.2 \text{ s}. \tag{5.6}$$

This compares to lifetimes of excited states of highly ionized argon in the order of  $\tau = 10^{-12} \text{ s}$ .

### 5.2.2 The impurity transport model

The applied 1D-transport code [22, 60] calculates the radial argon ion distribution based on given radial profiles of the electron density  $n_e$ , the electron and ion temperature  $T_e$  and  $T_i$ , the neutral particle density  $n_0$  and the diffusion coefficient  $D_{\perp}$ . It solves a set of coupled continuity equations describing each argon ion stage  $z$  in steady state:

$$\frac{\partial N_z(r)}{\partial t} = \frac{1}{r} \frac{\partial}{\partial r} \left( r \cdot \Gamma_{\perp}^z(r) \right) + S_z(r) = 0, \quad 0 \leq z \leq 18. \tag{5.7}$$

The ion balance can be treated in steady state, as the measurements were performed under continuous argon puffing. The source term  $S_z(r)$  in equation 5.7 contains all

ionization and recombination processes that couple the adjacent argon ion stages:

$$\begin{aligned}
S_z(r) = & N_{z-1}(r) \cdot Q_{ion(z-1 \rightarrow z)}(r) \cdot n_e(r) \\
& + N_{z+1}(r) \cdot [ Q_{rec(z+1 \rightarrow z)}(r) \cdot n_e(r) \\
& \quad + Q_{cx(z+1 \rightarrow z)}(r) \cdot n_0(r) ] \\
& - N_z(r) \cdot [ Q_{ion(z \rightarrow z+1)}(r) \cdot n_e(r) \\
& \quad + Q_{rec(z \rightarrow z-1)}(r) \cdot n_e(r) \\
& \quad + Q_{cx(z \rightarrow z-1)}(r) \cdot n_0(r) ].
\end{aligned} \tag{5.8}$$

Here argon-argon collisions are neglected. The radial particle flux density  $\Gamma_{\perp}(r)$  has a diffusive and a convective term:

$$\Gamma_{\perp}(r) = -D_{\perp}(r) \cdot \frac{\partial N_z(r)}{\partial r} + v_{\perp}(r), \tag{5.9}$$

while the convective velocity  $v_{\perp}(r)$  is included according to the common empirical scaling law (see page 27):

$$v_{\perp}(r) = -\alpha_v \cdot \frac{r}{a^2} \cdot D_{\perp}(r), \tag{5.10}$$

where  $\alpha_v = 1$  following [22]. As the convective transport component is coupled to the diffusivity, it does not represent a further degree of freedom. The transport coefficients are considered to be equal for all argon ion stages.

To illustrate the model's response to charge exchange and transport, figure 5.4 compares the argon ion balance for three different ideal scenarios. These include the pure corona equilibrium ( $n_0/n_e = 0$ ,  $D_{\perp}(r) = 0 \text{ m}^2/\text{s}$ , **A**), the corona equilibrium affected by charge exchange ( $n_0/n_e = 2 \cdot 10^{-5}$ ,  $D_{\perp}(r) = 0 \text{ m}^2/\text{s}$ , **B**) and the corona equilibrium affected by transport ( $n_0/n_e = 0$ ,  $D_{\perp}(r) = 1.5 \text{ m}^2/\text{s}$ , **C**). The relevant ion stages *Ar XVI*, *Ar XVII* and *Ar XVIII* are highlighted. In **B** a significant shift towards the lower ion stages due to charge exchange recombination is recognizable. On the other hand, in **C**, the particle transport dominated by the diffusive term clearly flattens the gradients in the argon ion density profiles. Yet, in **C** a constant diffusivity is assumed. In case of an inhomogeneous  $D_{\perp}(r)$  featuring steps or dips, diffusive transport can cause kinks or steps in the ion distribution functions. This is because high radial diffusivity tends to radially average the ion abundances, which can in extreme cases lead to almost constant profiles. Given that two areas of high diffusivity are delimited by a transport barrier, the resulting ion density profiles will show steps at the position of the barrier. These steps can locally have stronger gradients than the initial distribution without transport taken into account. This is demonstrated for two examples in figure 5.5. It shall be emphasized, that diffusive transport never inverts the gradients in the argon ion density profiles. This is because the diffusive flux disappears as soon as  $\partial N_z / \partial r = 0$ .

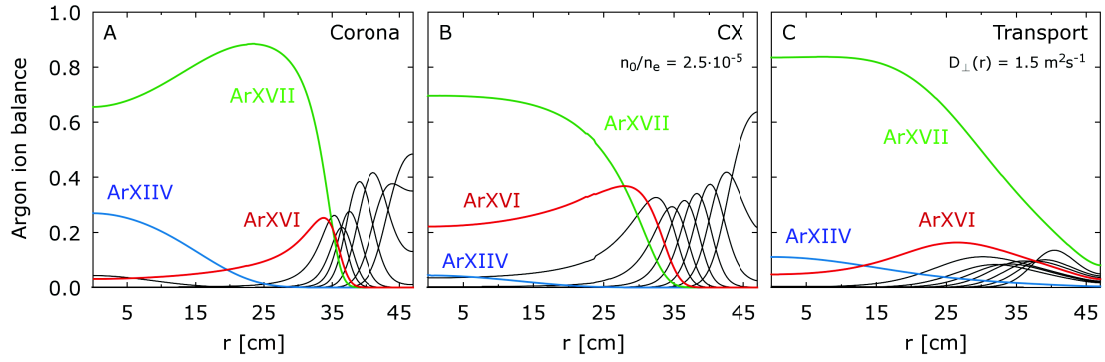


Figure 5.4: Argon ion balance modeled for a typical electron temperature profile in TEXTOR (#116924, ohmic,  $\hat{T}_e = 1.6 \text{ keV}$ ). The corona conditions (**A**) are compared to charge exchange (**B**) and transport (**C**) dominated scenarios.

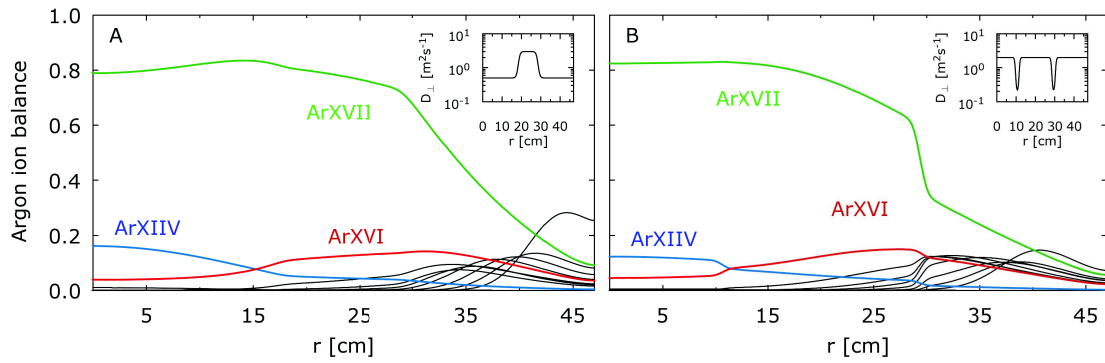
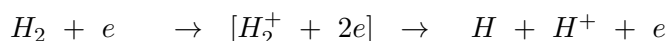


Figure 5.5: Argon ion balance modeled for two different profile shapes of  $D_{\perp}(r)$ : **a**) Zone of high diffusivity, **b**) Two narrow transport barriers.

### 5.2.3 The neutral particle transport model

The neutral particle density is calculated in the diffusion approximation using an excerpt of the RITM code [22, 60]. The model is based on a 1D-geometry and produces steady state solutions based on given profiles of the plasma density and the temperature. Molecular and atomic hydrogen originating from recycling processes at the plasma wall elements are represented by a constant influxes through the LCFS. The following processes are taken into account to describe the interaction between neutrals and plasma particles:

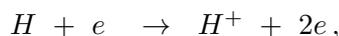
$H_2$  molecules are dissociated and ionized by electrons and by charge exchange with the main plasma ions:



Charge exchange collisions between the main plasma ions and cold first generation neutrals effectively result in an energy exchange, so that the neutral particles are thermalized:



Atomic hydrogen can be ionized by electron collisions:



and can be created by recombination of the main plasma ions with electrons:



This leads to a set of diffusion equations describing each of the neutral particle species arising from the above mentioned processes. The equation system is solved in steady state, and the resulting density profiles of the individual species are then accumulated to the normalized total neutral particle density  $\tilde{n}_0(r)$ , as shown in figure 5.6. More details can be found in [22].

## 5.3 Results

For most of the analyzed discharges good agreement between the experimental data and the model can be achieved. Both argon ion ratios can be reproduced consistently along the entire radial field of view. Figure 5.7 shows a complete set of results obtained for an ohmic discharges in TEXTOR. Furthermore, figure 5.8 compares the results for a sequence of ohmic discharges with increasing plasma density. In all cases a region of high radial transport is found to be essential for reproducing the experimental data.

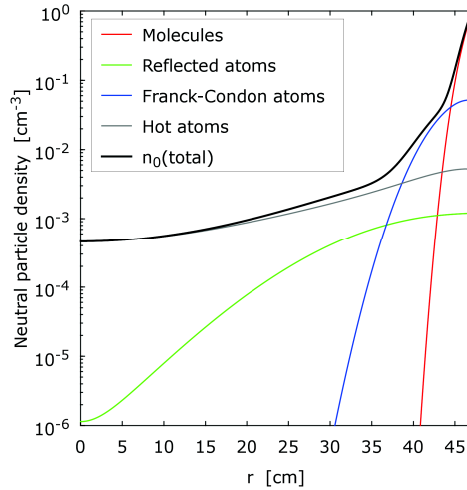


Figure 5.6: Normalized neutral particle density profile, modeled for an ohmic TEXTOR discharge according to [22, 60].

Transport is the dominant mechanism causing a majority of the discrepancies between the experiment and the predictions from corona modeling. As already mentioned above, this does not confirm the results from Rosmej et al. [47], who deduced low impurity transport coefficients from 1D X-ray spectra measured at TEXTOR. Still, significant neutral particle densities are needed to achieve a consistent description of both ion ratios. Here, the radial profile shapes  $\tilde{n}_0(r)$ , calculated with the neutral particle diffusion model, turn out to be adequate. However, for some discharges an exact reconstruction of both ion ratios is less accurate. In the following all results are discussed in detail.

### 5.3.1 The radial impurity transport coefficient

The obtained transport coefficients  $D_{\perp}(r)$  show very similar characteristics for all analyzed discharges. A region of high diffusive impurity transport is needed to describe both argon ion ratios consistently along the radius. Apart from smaller variations this high transport zone extends from about 15 cm to 30 cm off center. With clearly anomalous diffusion coefficients of  $D_{\perp} = 2 - 5 \text{ m}^2\text{s}^{-1}$  it increases the ion ratio  $Ar\text{ XVIII}/Ar\text{ XVII}$  at the edge region from practically 0% to about 1 – 5%. These amounts of H-like argon are needed to explain the dramatic increase in the normalized ion ratio in figure 5.3(a). It also explains the increased values of  $Ar\text{ XVI}/Ar\text{ XVII}$  between  $r = 10 \text{ cm}$  and  $r = 30 \text{ cm}$ , as  $Ar\text{ XVI}$  from the plasma edge can diffuse inwards.

Towards either side the high transport zone is delimited by transport barriers with considerably reduced diffusivity. Inside the inner transport barrier ( $r < 15 \text{ cm}$ ) the diffusivity stays reduced. For increasing plasma density an overall reduction of the absolute  $D_{\perp}$  values can be stated, while the edges seem to stay at fixed positions.

The region of high diffusivity spatially coincides with a slight flattening of the electron temperature obtained from the  $K_{\alpha}$ -spectra. This flattening is also visible in the  $T_e$ -

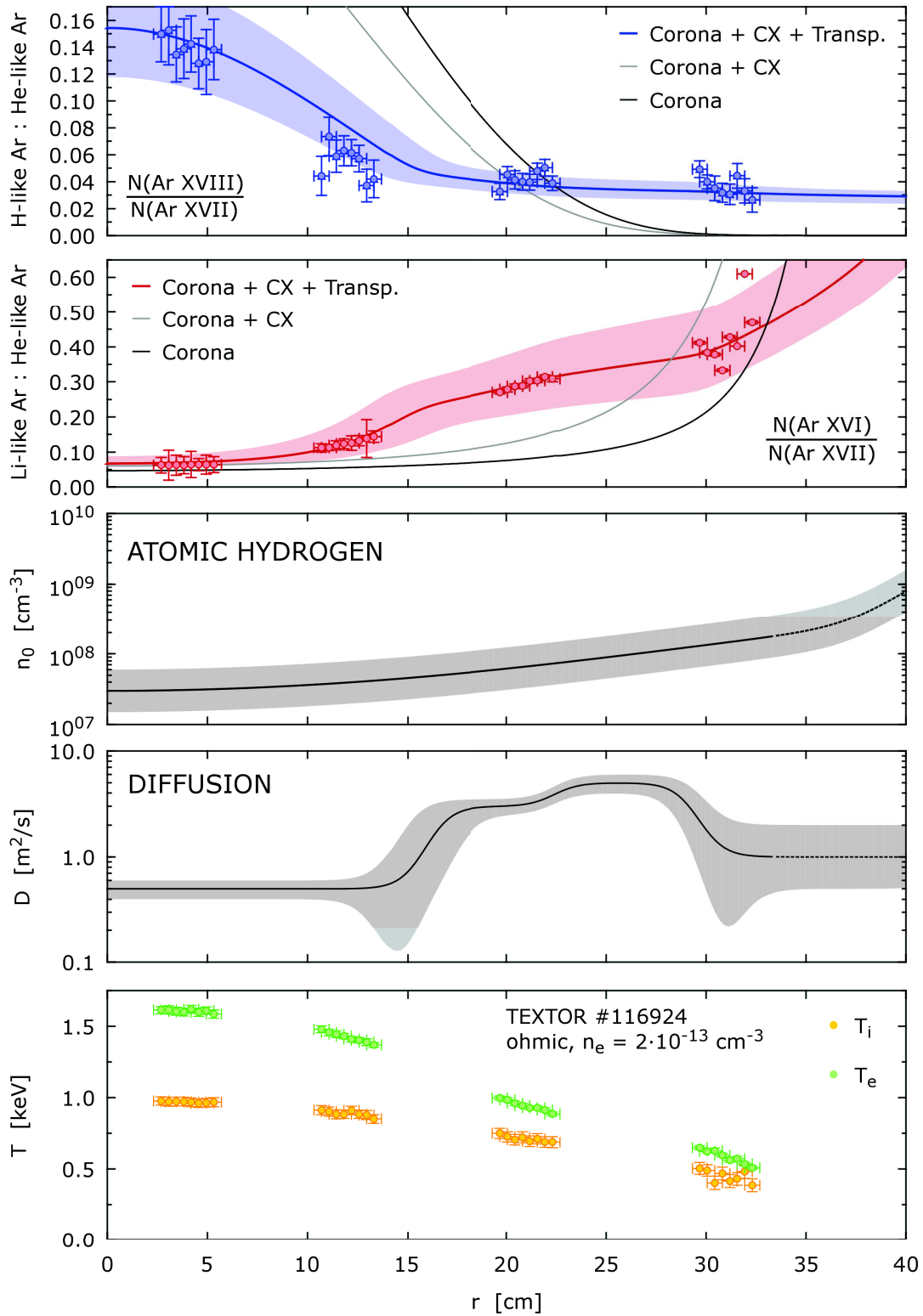


Figure 5.7: Complete set of quantities deduced from the radially resolved  $K_\alpha$ -spectra measured during an ohmic discharge in TEXTOR. The shaded areas indicate the errors.

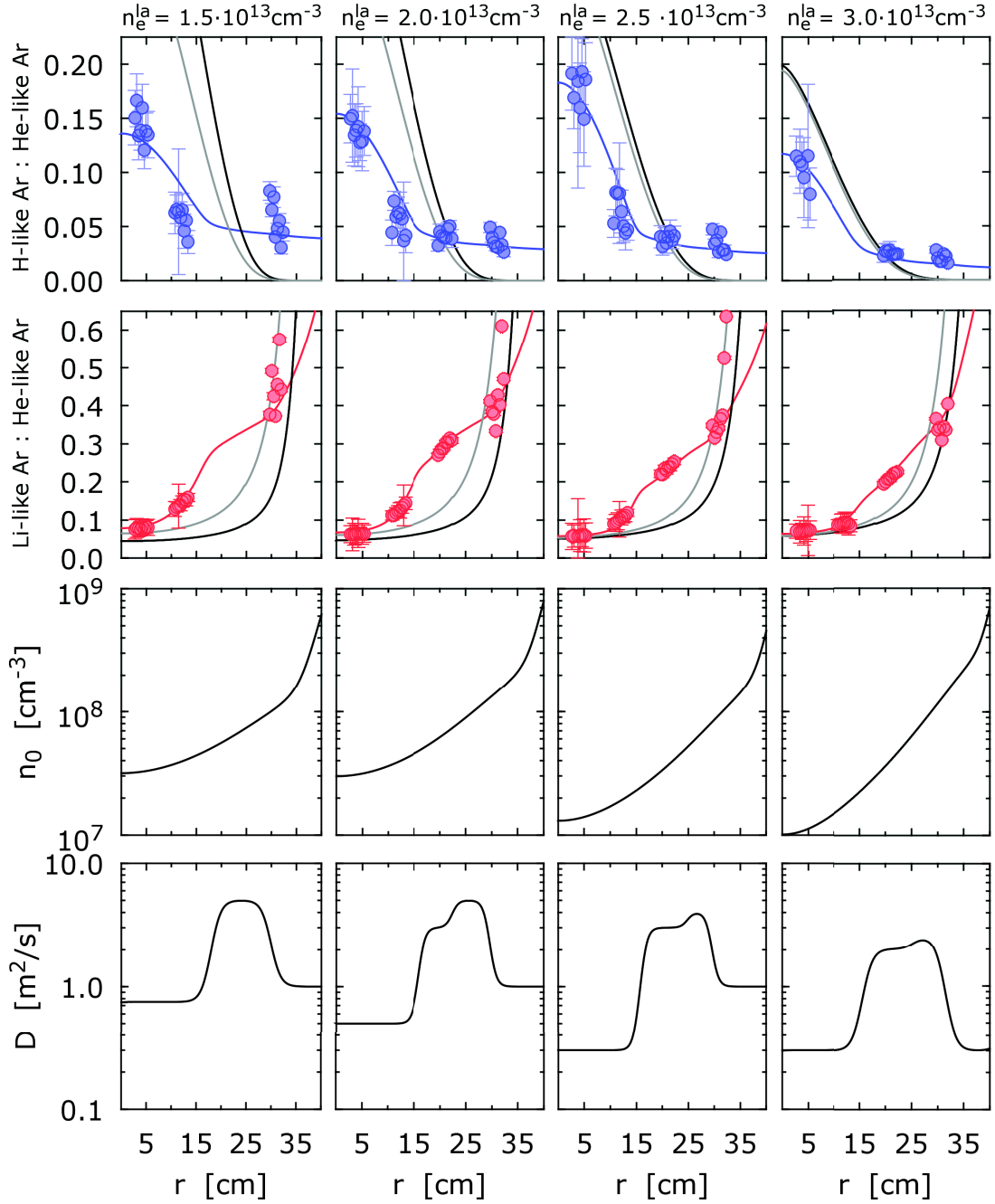


Figure 5.8: Measured and modeled argon ion ratios including the obtained transport coefficients and neutral particle densities for subsequent ohmic TEXTOR discharges with increasing plasma density (#116921  $n_e = 1.5 \cdot 10^{13} \text{cm}^{-3}$ , #116924  $n_e = 2.0 \cdot 10^{13} \text{cm}^{-3}$ , #116926  $n_e = 2.5 \cdot 10^{13} \text{cm}^{-3}$ , #116925  $n_e = 3.0 \cdot 10^{13} \text{cm}^{-3}$ ). For discharge #116921 the reconstruction of  $Ar^{17+}/Ar^{16+}$  is less accurate. This is discussed in section 5.3.3.

profiles from ECE measurements (see section 6). This speaks for an electron transport behavior that is similar to that of the argon ions.

**Accuracy in determination of  $D_{\perp}(\mathbf{r})$**  The accuracy in  $D_{\perp}(r)$  is limited by the fragmentary radial coverage of the plasma by the detector array. Within the unmonitored areas the exact gradients in the ion ratios stay unknown. This leads to an uncertainty in the position and shape of the edges in  $D_{\perp}(r)$ . Especially the steepness of the transitions between high and low transport areas is difficult to resolve. The inner transport barrier can be localized with an accuracy of  $\Delta r = \pm 2 - 3 \text{ cm}$ . The outer transport barrier can with high accuracy be localized at  $r \approx 31 \text{ cm}$ , as the inner edge is depicted by the outer most CCD. However, as beyond  $r = 32 \text{ cm}$  no further data is available, it is difficult to characterize its shape. To reconstruct the steep slope in  $Ar\text{ XVI}/Ar\text{ XVII}$  at  $r \approx 30 \text{ cm}$  a narrow and deep dip in  $D_{\perp}(r)$  is needed. A broader and less deep transport barrier gives similar results for  $r < 30 \text{ cm}$ , but cannot reconstruct the strong increase in  $Ar\text{ XVI}/Ar\text{ XVII}$  at  $r \approx 30 \text{ cm}$ . The argon ion ratio  $Ar\text{ XVIII}/Ar\text{ XVII}$  stays nearly unaffected by the outer transport barrier, as its gradient here is close to zero. A continuous radial measurement would significantly increase the accuracy in the determination of  $D_{\perp}(r)$ .

Based on the current radial resolution it cannot be excluded, that the transitions between high and low diffusivity feature deep, narrow dips (compare figure 5.7). This would be in qualitative agreement with results from Hogeweij et al. [61], who proposed narrow dips in the diffusion coefficient for electrons located at the rational  $q$ -surfaces. Dips in  $D_{\perp}$  have also been observed at JT-60 by Takenaga et al. [33]. Again, full radial coverage would resolve this.

Finally, it shall be emphasized that all spectral data and all deduced results have to be understood as time averaged over the flat top phase of the considered discharges.

**$D_{\perp}(\mathbf{r})$  in comparison to literature** The obtained profiles of the diffusion coefficient are in very good agreement with earlier results from Biel et al. [31] based on time resolved VUV and soft X-ray spectroscopy at TEXTOR. Biel modeled the temporal evolution of the emission of several argon ion species measured along a central chord in TEXTOR. The deduced  $D_{\perp}(r)$  show characteristics that are very similar to those obtained from  $K_{\alpha}$ -imaging (see figure 5.9). For the two higher density cases both methods practically give identical results, matching in absolute values as well as in the positions of the edges. The agreement is well within the estimated error bars. Only in the low density case the agreement is less good, though still reasonable. The shift of the inner transport barrier with decreasing density cannot be confirmed by X-ray imaging. For the low density case X-ray imaging also gives higher  $D_{\perp}$ -values in the plasma center. Furthermore, the slope of the outer transport barrier derived from the VUV measurements is generally not as steep as that from X-ray imaging.

The results for argon in TEXTOR are in good agreement with findings from other machines and impurity elements. Mattioli et al. measured  $D_{\perp}(r)$  for nickel [27] and titanium [28] in Tore Supra showing very similar absolute values and characteristics in

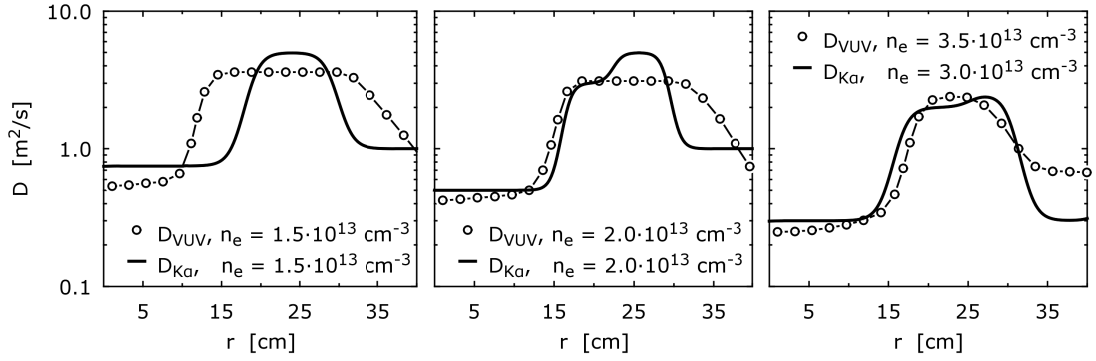


Figure 5.9: Comparison of the radial diffusion coefficient  $D_{\perp}(r)$  for argon ions in ohmic TEXTOR discharges with different plasma densities. The results from time resolved VUV spectroscopy (open dots) are rearranged from Biel et al. [31]. The solid lines show the results from spatially resolved  $K_{\alpha}$ -spectroscopy.

the radial profile. A region of high diffusivity is observed, that is stable in radial position, but alters in absolute values with time. Also from JET L-mode plasmas similar results for iron, nickel and argon have been reported by Gianella et al. [26].

**Spatial coincidence with rational q-surfaces** The prominent edges in  $D_{\perp}(r)$  appear to spatially coincide with the low order rational q-surfaces in TEXTOR. The inner edge is located at  $z \approx 15 \text{ cm}$  where  $q = 1$ , while the outer edge corresponds to  $q = 2$  at  $z \approx 30 \text{ cm}$  (see figure 5.10(a)). Also at  $r = 25 \text{ cm}$ , where  $q = 1.5$ , a step in  $D_{\perp}(r)$  slightly improves the agreement between model and experiment. The spacial coincidence of the high transport zone and the rational q-surfaces suggests a connection to MHD effects like magnetic islands. Magnetic reconnection due to island structures would indeed strongly increase the radial transport ( $D_{\perp} = D_{\parallel}$ ). However, an island structure of  $10 - 15 \text{ cm}$  in diameter is rather unlikely. In this respect two narrow peaks in  $D_{\perp}(r)$  at  $q = 1, 2$  corresponding to two individual island structures would be expected rather than one broad region extending from  $q = 1$  to  $q = 2$ . Yet two narrow peaks in  $D_{\perp}(r)$  do not recreate the observed ion distribution. Also a connection to sawtooth oscillations is possible. Figure 5.10(b) shows the electron density profile of an ohmic TEXTOR discharge, measured at ten different times within one sawtooth period. The so called inversion radius  $r \approx 15 \text{ cm}$ , where  $dn_e/dt = 0$ , coincides well with the position of the inner transport barrier observed for argon. Also for  $r \approx 30 \text{ cm}$  the oscillations in  $n_e(r)$  come down to zero. This roughly coincides with the outer edge in  $D_{\perp}(r)$  for argon. However, a detailed analysis of the mechanisms behind the observed transport coefficients is beyond the scope of this work.

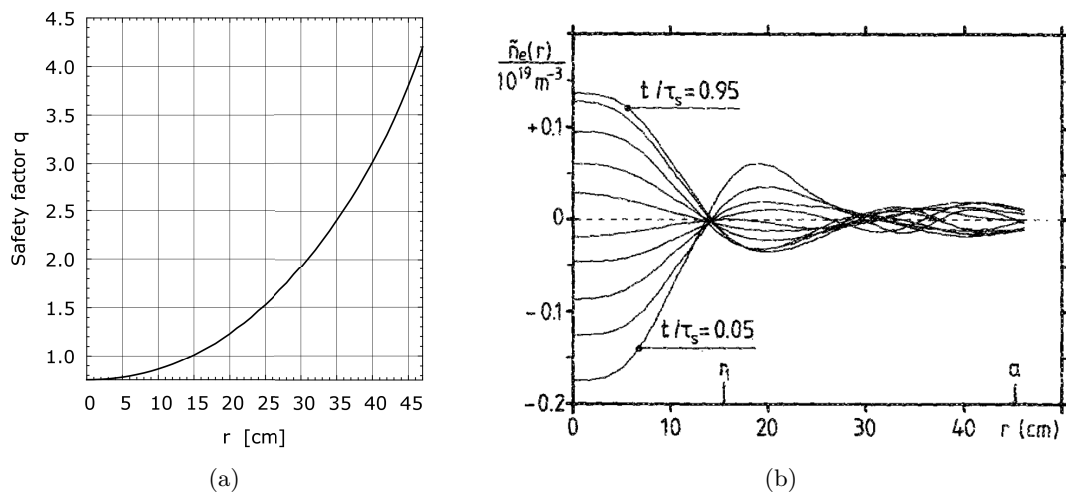


Figure 5.10: **a)** Safety factor profile for ohmic TEXTOR discharges after Soltwisch based on an experimentally obtained scaling law [62]. **b)** Oscillation of the electron density relative to the average value measured at ten different times during one sawtooth period. The inner and outer inversion radius at  $r = 15 \text{ cm}$  and  $r = 30 \text{ cm}$  coincide with the edges found in  $D_{\perp}(r)$ . Reprinted with permission from Soltwisch Rev. Sci. Instrum. 59, 1599 (1988). Copyright 2014, AIP Publishing LLC.

### 5.3.2 Neutral particle density

The neutral particle density profile shapes  $\tilde{n}_0(r)$  calculated in the diffusion model are adequate to reconstruct the measured line ratios (see figure 5.8 and 5.11(a)). The obtained central  $n_0$ -values range between  $10^7 \text{ cm}^{-3}$  and  $10^8 \text{ cm}^{-3}$  depending on the plasma density, while at lower plasma densities the central  $n_0$  is higher. At  $r \approx 30 \text{ cm}$  off-center  $n_0$  is close to  $10^8 \text{ cm}^{-3}$  for all plasma densities analyzed. Further out ( $r > 30 \text{ cm}$ ) no distinct statements can be made, due to missing data points. Yet according to the modeled profile shapes,  $n_0$  reaches values between  $10^{10} \text{ cm}^{-3}$  and  $10^{11} \text{ cm}^{-3}$  at the plasma boundary. This corresponds well with results from laser induced fluorescence (LIF) measurements that were performed earlier at TEXTOR [63]. Here the neutral density close to the LCFS ( $45.5 \text{ cm} \leq r \leq 47 \text{ cm}$ ) was found to be  $2 - 5 \cdot 10^9 \text{ cm}^{-3}$ . However, the applied LIF method is not sensitive for molecular hydrogen, so that only the atomic component can be compared. The  $H^0$ -density obtained from the diffusion model is in good agreement with the LIF results (#116926:  $n(H^0)(r = 47\text{cm}) = 3 \cdot 10^9 \text{ cm}^{-3}$ ). Within the radial field of view ( $r \leq 30 \text{ cm}$ ) the neutral particle density can be determined with an accuracy of ca. a factor of two. A slightly reduced diffusion coefficient can compensate slightly higher  $n_0$ -values, so that different pairs of  $n_0(r)$  and  $D_{\perp}(r)$  can result in similar argon ion profiles. This replaceability of transport and charge exchange can be significantly reduced by a continuous radial measurement with a big one piece detector. Based on continuous data points the exact gradients in  $Ar\text{ XVI}/Ar\text{ XVII}$  and  $Ar\text{ XVIII}/Ar\text{ XVII}$  will allow for a more precise determination of  $D_{\perp}(r)$  and with this also of  $n_0(r)$ . The lower detection limit for neutral particles is  $n_0/n_e \approx 10^{-7}$ . Finally, figure 5.11(b) compares the neutral particle profile shapes from the diffusion model and from the EIRENE code [64]. Within the radial field of view and within accuracy both profile shapes agree.

**Measurements in helium plasma** In section 5.1 the differences between the measurements in hydrogen and helium working gas have been discussed qualitatively. In helium plasma a strongly reduced neutral particle background is expected, and in agreement with this, the argon spectra measured during helium discharges showed significantly smaller deviations from the corona values than in case of hydrogen discharges.

As shown in figure 5.12, the argon ion ratios obtained from the measurements in helium can indeed be reconstructed without charge exchange contributions. At the same time, the transport coefficient is similar to those found in hydrogen plasmas. This is strong evidence for the correct interpretation of the charge exchange effects in the  $K_{\alpha}$ -spectra and the correct separation from transport effects.

### 5.3.3 Current limitations of the method

The presented interpretation of the radially resolved  $K_{\alpha}$ -spectra has shown good agreement between the experimental data and the modeled argon ion ratios. However, the applied model involves some simplifications that might limit its validity. Details are discussed below.

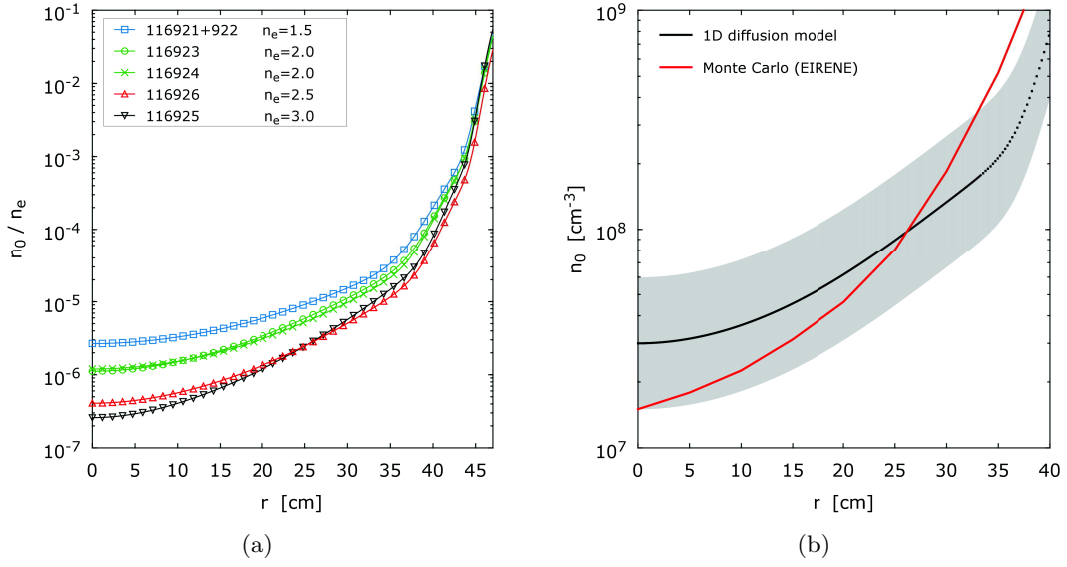


Figure 5.11: **a)** Radial profiles of the neutral particle density  $n_0$  obtained from spatially resolved  $K_\alpha$ -spectroscopy. The plot shows  $n_0(r)$  normalized to the electron density profile  $n_e(r)$ . **b)** Comparison of the neutral particle density profile shapes from 3D Monte Carlo modeling (EIRENE) and 1D diffusion modeling (RITM) for discharge #116924. The EIRENE results are poloidally and toroidally averaged. Both profile shapes agree within the accuracy of the measurement.

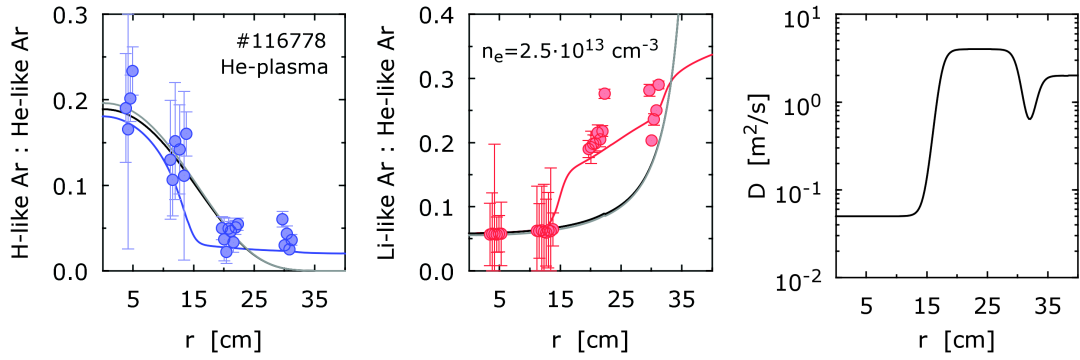


Figure 5.12: Argon ion ratios obtained from the  $K_\alpha$ -spectra measured during a discharge in helium working gas (#116778). No contributions from charge exchange with neutral background particles are needed to describe the measurement. The diffusion coefficient  $D_\perp(r)$  is similar to those found in hydrogen plasmas. The data points with  $r < 15$  cm were measured below the equatorial plane.

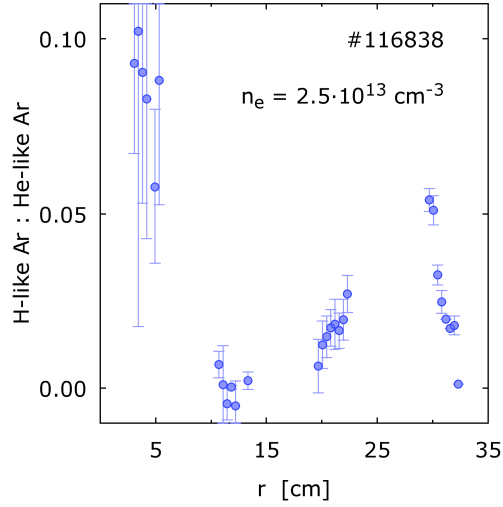


Figure 5.13: The argon ion ratio  $Ar\ xVIII/Ar\ xVII$  determined from spatially resolved  $K_\alpha$ -spectra measured in an ohmic discharge in TEXTOR (#116838). The clearly non-monotonic behavior cannot be described within the applied transport model. For this plot the spectra were interpreted on basis of the neutral particle density profile and the argon ion balance found for discharge #116926.

**Convective transport** The convective transport is handled using the semi empirical scaling formula  $v_\perp = -\alpha_v \cdot \frac{r}{a^2} \cdot D_\perp$  with  $\alpha_v = 1$ . This results in an inwards flux, that is weak compared to the diffusive flux. However, for some discharges the applied model cannot describe the observed argon ion ratios exactly. In these cases  $Ar\ xVIII/Ar\ xVII$  has a local minimum at about  $r = 15\ cm$  and a local maximum at about  $r = 25\ cm$ . An example is shown in figure 5.13. This radial behavior cannot be caused by diffusive transport, as the initially monotonic gradients in the corona distribution cannot be reversed by diffusion. Therefore, convective transport mechanisms must be involved in this. A local maximum as observed in figure 5.13, could be caused by a zero-crossing of  $v_\perp(r)$  close to  $r = 25\ cm$ , representing a transition from inwards to outwards transport. To implement such convective transport behavior, a decoupling of  $v_\perp(r)$  and  $D_\perp(r)$  is necessary. A detailed investigation of this aspect is left for future investigations. Yet it shall be noted that due to the high radial resolution, X-ray imaging most likely allows a distinction between diffusive and convective transport. This should especially be true in case of significant inhomogeneities in  $v_\perp$ .

**1D-model of TEXTOR** The presented reconstruction of the argon spectra is based on a 1D-model that assumes poloidal and toroidal symmetry<sup>2</sup> in TEXTOR. However,

<sup>2</sup>The Shafranov shift, can be ignored here, as it does not violate the up-down-symmetry in the plasma. The lines of sight are distributed vertically over the minor radius and the view angles lie in horizontal

a slight up-down-asymmetry is observed in the argon emission measured at TEXTOR. Below the equatorial plane the temperatures obtained from the  $K_\alpha$ -spectra tend to be slightly higher than above the equatorial plane. Also the argon ion balance seems to be slightly shifted towards the higher ion stages. With exception of discharge #116778 the presented analysis is only based on data points from above the equatorial plane.

Within the 1D-model also the neutral particle density profiles are considered radially symmetric. However, the neutral particles mainly originate from recycling processes at limiter elements, which do not surround the plasma surface homogeneously. Although the plasma-wall-contact at the different limiter elements is currently not well diagnosed at TEXTOR, the ALT-limiter is assumed to represent the most relevant neutral particle source. The ALT-limiter is located at the low field side below the equatorial plane. Therefore, also the neutral particle density will to some extent show an up-down asymmetry. Further poloidal or even toroidal asymmetries in  $n_0(r)$  might arise from the other limiter elements and positions. However, compared to the radial gradients in the neutral particle density the eventual poloidal and toroidal gradients will most likely be small. In case of a complete radial scan of the argon ion emission a 2D-model should be applied to account for the discussed asymmetries.

### 5.3.4 Evaluation of the absolute line intensities

So far only the line intensity ratios in the  $K_\alpha$ -spectrum were evaluated. The ratios  $(\mathbf{x}+\mathbf{y}):\mathbf{w}$ ,  $\mathbf{k}:\mathbf{w}$  and  $(\mathbf{q}+\mathbf{r}):\mathbf{w}$  lead to three linearly independent equations allowing to determine the electron temperature  $T_e$  as well as the argon ion ratios  $Ar\text{ XVI}/Ar\text{ XVII}$  and  $Ar\text{ XVIII}/Ar\text{ XVII}$ .

However, the absolute brightness profiles of the  $K_\alpha$ -lines contain further information about the individual argon ion abundances. The excitation parts of the lines  $\mathbf{w}$ ,  $\mathbf{x}$ ,  $\mathbf{y}$  and  $\mathbf{z}$  allow to trace back on the density profile of  $Ar\text{ XVII}$ . Yet the recombination parts that are proportional to the density of  $Ar\text{ XVIII}$  have to be subtracted first. In this respect it is more straightforward to consider the brightness profile of the  $\mathbf{k}$ -satellite, which is exclusively supplied by  $Ar\text{ XVII}$  via dielectronic recombination. The measured intensity  $I_k(r)$  is given by:

$$I_k(r) \propto \int_0^1 d\rho Q_{dr}(\rho) \cdot n_e(\rho) \cdot N(Ar\text{ XVII})(\rho) = \int_0^1 d\rho \xi_k(\rho), \quad (5.11)$$

where the emission profile along the line-of-sight was defined as  $\xi_k(\rho)$ . In order to extract  $\xi_k(\rho)$  equation 5.11 needs to be inverted within an Abel transformation. This inversion is performed numerically using the ABEL code [65]. Dividing the emission profile by the electron density  $n_e(r)$  and the effective rate coefficient  $Q_{dr}(r)$ , then gives the density profile of  $Ar\text{ XVII}$ . In an analogous manner the density profile of  $Ar\text{ XVI}$  can be obtained from the inner shell excitation parts of the satellites  $\mathbf{q}$  and  $\mathbf{r}$ . The intensity  $I_{q+r}(r)$  is

---

planes.

given by:

$$\begin{aligned}
 I_{q+r}(r) &\propto \int_0^1 d\rho (Q_{iexc,q}(\rho) + Q_{iexc,r}(\rho)) \cdot n_e(\rho) \cdot N(Ar\ xVI)(\rho) \\
 &= \int_0^1 d\rho \xi_{qr}(\rho),
 \end{aligned}
 \tag{5.12}$$

where the weak contributions from dielectronic recombination were neglected. They can readily be subtracted according to  $I_k$  (see section 3.3.1). The obtained density profiles of *Ar xVI* and *Ar xVII* are shown in figure 5.14(a) for one ohmic discharge.

At the temperatures present in TEXTOR the total argon density can be approximated by the dominant ion stages *Ar xVIII*, *Ar xVII* and *Ar xVI*:

$$N(Ar_{tot})(r) \approx N(Ar\ xVI)(r) + N(Ar\ xVII)(r) + N(Ar\ xVIII)(r).
 \tag{5.13}$$

The resulting total argon density profile is shown in figure 5.14(b). The density of *Ar xVIII* is included based on the ion ratio  $Ar\ xVIII/Ar\ xVII(r)$  that was determined from the line ratios. The total argon density is clearly proportional to the electron density profile. This is in agreement with recent reports from ASDEX-U [66], where the total carbon density was found to be proportional to  $n_e(r)$ .

The evaluation of the other line intensities is redundant and does not gain further information, as all line ratios have been evaluated before.

## 5.4 Conclusion

A new diagnostic method based on imaging  $K_\alpha$ -spectroscopy was presented. It allows a simultaneous measurement of the neutral particle density profile  $n_0(r)$  and the diffusion coefficient for radial impurity transport  $D_\perp(r)$ . The obtained  $n_0(r)$  profile shapes are in agreement with results from a neutral particle diffusion model. The central  $n_0$ -values range between  $10^7\text{ cm}^{-3}$  and  $10^8\text{ cm}^{-3}$  depending on the plasma density. According to the  $n_0$ -profile shapes given by the diffusion model, this corresponds to  $n_0$ -values at the plasma edge that are consistent with earlier LIF-measurements. At the same time, the obtained diffusion coefficients show very good agreement with earlier experimental results based on the time evolution of argon VUV-lines [31]. A distinct region of high radial transport is found at about half minor radius of TEXTOR, where  $D_\perp = 2 - 5\text{ m}^2/s$ . In the plasma center the diffusion coefficient drops down to  $D_\perp \leq 0.5\text{ m}^2/s$ . Finally, the evaluation of the absolute line intensities revealed that the total argon density is proportional to the electron density.

The clear distinction of charge exchange and transport effects in the  $K_\alpha$ -spectrum is based on the presence of the Li-like satellite lines that are free of cascade contributions from charge exchange [59]. Yet it is important to note that unique solutions are only possible due to radial resolution. A 0D-spectrum will allow for multiple solutions in terms of  $n_0(r)$  and  $D_\perp(r)$ .

The scope of this work clearly is the investigation of charge exchange effects in X-ray spectroscopy. The radial impurity transport therefore was not studied in full detail.

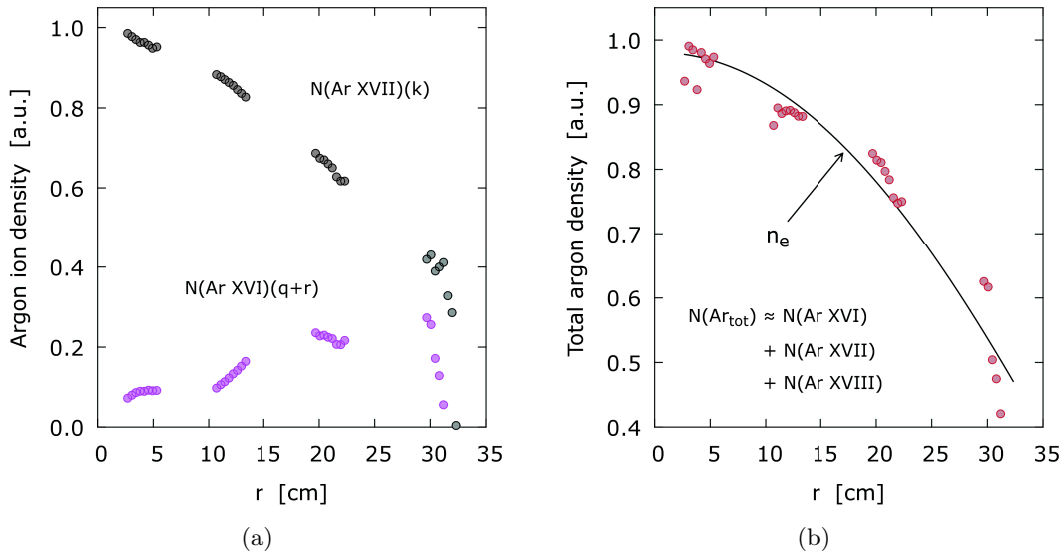


Figure 5.14: **(a)** Relative argon ion density profiles of  $\text{Ar XVI}$  and  $\text{Ar XVII}$  obtained from the brightness profiles of the satellites  $q+r$  and  $k$ , respectively. **(b)** The total argon density profile approximated from the individual ion density profiles shown in (a) and the ion ratio  $\text{Ar XVIII}/\text{Ar XVII}$ . The total argon density is found to be proportional to  $n_e(r)$ .

Still, the results suggest that  $K_\alpha$ -imaging is a powerful diagnostic for impurity transport analysis. The high radial resolution allows to distinguish between diffusive and convective processes based on geometrical considerations. Diffusion only reduces gradients or forms steps in the ion ratio profiles, while possible inversions can only be caused by convective transport.

There are several possibilities to improve the present state of the method. These first of all include a continuous radial coverage of the minor plasma radius by the spectrometer. This can be achieved by using a big one piece detector. Furthermore, the argon emission should be exploited towards the plasma edge as far as possible, like for example realized at ALCATOR [42]. This will significantly increase the accuracy in  $n_0(r)$  and  $D_\perp(r)$ .

The argon ion distribution was so far calculated within a 1D-transport model assuming poloidal and toroidal symmetry. A 2D-model would allow for respecting poloidal variations in the neutral particle density or the argon ion distribution. With respect to strong toroidal asymmetries in  $n_0(r)$ , as for example in neutral beam heated discharges, it should be sufficient to distinguish between the local neutral particle density  $n_0^l(r)$  present at the observed plasma volume and the toroidally averaged (global) neutral particle density  $n_0^g(r)$ . The local  $n_0^l(r)$  will then be relevant for CX-cascade contributions to the spectral lines, while the global  $n_0^g(r)$  will be relevant for the CX-impact on the ionization balance.

Finally,  $K_\alpha$ -spectroscopy could be combined with measurements of the Rydberg lines of

He-like argon. As discussed in section 7.1, the Rydberg series together with the  $4p - 1s$ -transition of H-like argon allow to determine the ion ratio  $Ar\ xVIII/Ar\ xVII$ . The Rydberg lines can usually be considered as pure excitation lines that are almost completely independent from local variations in  $n_0(r)$ . This might especially help in case of neutral beam heated discharges. However, the analysis of beam heated discharges is left for future investigations.

In the presented evaluation the sight-line integrated spectral data was handled within a forward integration over the argon emission profiles. Alternatively the emission profiles could be extracted from the spectra with the help of tomographic methods like an Abel inversion.

## 6 Plasma temperature profiles from X-ray imaging at TEXTOR

A basic application of  $K_\alpha$ -spectroscopy are plasma temperature measurements. As explained in section 3.3.1 the  $K_\alpha$ -spectrum allows to determine the electron temperature  $T_e$  from the intensity ratio of the dielectronic satellites and the reference line  $w$ . The ion temperature  $T_i$  can be deduced from the Doppler width of the spectral lines.

In this chapter radial profiles of the electron and the argon ion temperature obtained from  $K_\alpha$ -imaging are presented and shortly discussed. This includes a comparison to reference the data from the ECE diagnostic ( $T_e(r)$ ) and earlier CXRS measurements performed at the plasma edge ( $T_i(r)$ ). The advantage of  $X$ -ray-imaging over CXRS is, that no diagnostic or heating beam is needed. Therefore, also in purely ohmic discharges ion temperature measurements can be performed. The analyzed TEXTOR discharges include ohmic and beam heated plasma scenarios. All results are time averaged over the entire flat top phase of a discharge (see 4.2.3).

Figure 6.1 illustrates simultaneously measured  $T_e$ - and  $T_i$ -profiles from a sequence of ohmic TEXTOR discharges at different plasma densities ( $\bar{n}_e = 1.5 - 3.0 \cdot 10^{13} \text{ cm}^{-3}$ ) and a constant plasma current of 350 kA. The observed central electron temperature ranges between 1.3 keV at high density and 1.8 keV at low density. At the same time, the central ion temperature stays almost constant at ca. 1 keV for all analyzed densities. The ion temperature profile has a smooth shape along the entire radial field of view. On the outermost lines-of-sight ( $r \approx 30 \text{ cm}$ ), it has reduced by about 50% to 0.5 keV. The electron temperature is significantly stronger peaked than the ion temperature. At  $r \approx 20 \text{ cm}$   $T_e$  is reduced by about 40% relative to the central value. For  $r \geq 20 \text{ cm}$  it converges towards  $T_i$ .

The density dependence of the temperatures can quantitatively be understood from the ohmic heating mechanisms. The ohmic current drive mainly acts on the electrons, due to their higher mobility. With a constant current drive, but an increasing number of particles, the electron temperature reduces towards higher plasma densities. The ions, however, are primarily heated via thermal equilibration with the electrons. The degree of thermalization depends on the collision rates, which again are proportional to the particle densities. As a consequence,  $T_e$  and  $T_i$  approach towards higher  $n_e$ . For  $T_i$  this results in a weak, but non monotonous dependence on the plasma density, as the proceeding thermalization competes with the decrease of  $T_e(r)$ . The variation of  $T_i$  stays within  $\pm 10\%$ .

Figure 6.2 compares  $T_e(r)$  and  $T_i(r)$  measured during neutral beam heated TEXTOR discharges at a constant plasma density of  $\bar{n}_e = 2.5 \cdot 10^{13} \text{ cm}^{-3}$ . In green and blue the

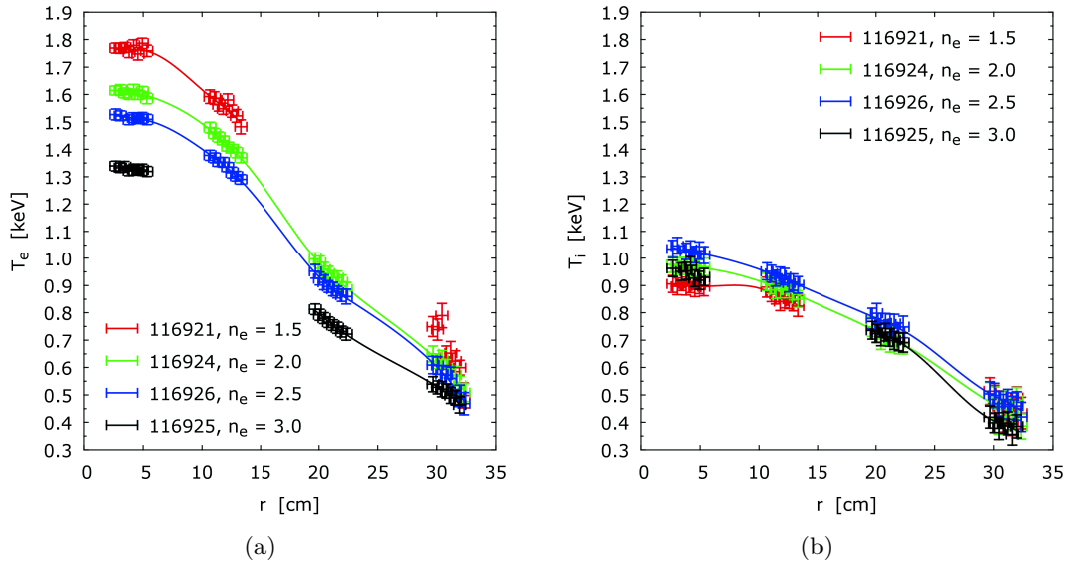


Figure 6.1: Electron temperature profiles (a) and ion temperature profiles (b) measured in subsequent ohmic TEXTOR discharges with increasing plasma density. Missing data points are due to technical reasons.

temperature profiles for two different beam power settings are shown, red indicates the ohmic reference. The beam energy is in both cases  $E_b = 50 \text{ keV}$ , while the beam aperture is maximal ( $VT = 50 \text{ cm}$ , blue) or reduced to  $VT = 15 \text{ cm}$  (green). In the beam heated cases, both  $T_e$  and  $T_i$  show a strong peaking in the plasma center ( $r < 10 \text{ cm}$ ), while for  $r \geq 10 \text{ cm}$  the profile shapes are similar to the ohmic case. For full beam power, the central electron temperature reaches  $2.2 \text{ keV}$ , but comes back to ohmic values for  $r \geq 10 \text{ cm}$ . Compared to this, the central ion temperature reaches  $1.9 \text{ keV}$ . For  $r \geq 10 \text{ cm}$ , it also follows the ohmic profile shape, but stays about 20 – 30% higher in absolute values. For the presented plasma density  $T_e \geq T_i$  holds at all times.

The observed temperature profiles can quantitatively be understood from the mechanisms of neutral beam heating. The neutral beam heating has strongest impact on the inner flux tubes, as here the interaction volume has the biggest fraction relative to the total volume of the flux tube. This explains the narrow peaking of the temperature profiles within  $r = 10 \text{ cm}$ . Furthermore, the power density profile of the neutral beams drops off quickly towards greater plasma radii. According to Uhlemann and Ongena [67], the full width at half maximum of the power density profile is  $10 \text{ cm}$  for fully open beam aperture and about  $6 \text{ cm}$  for the aperture reduced to  $15 \text{ cm}$ . The maximum lies in the plasma center at  $r = 0 \text{ cm}$ . The peaking of  $T_i$  stays within  $r = 10 \text{ cm}$  for both aperture settings, but a taper of the peaking for the smaller beam aperture is not visible in the data.

The argon ion temperature profile in ohmic discharges is found to be approximately proportional to the electron density profile  $n_e(r)$ . In order to illustrate this, figure 6.3(a)

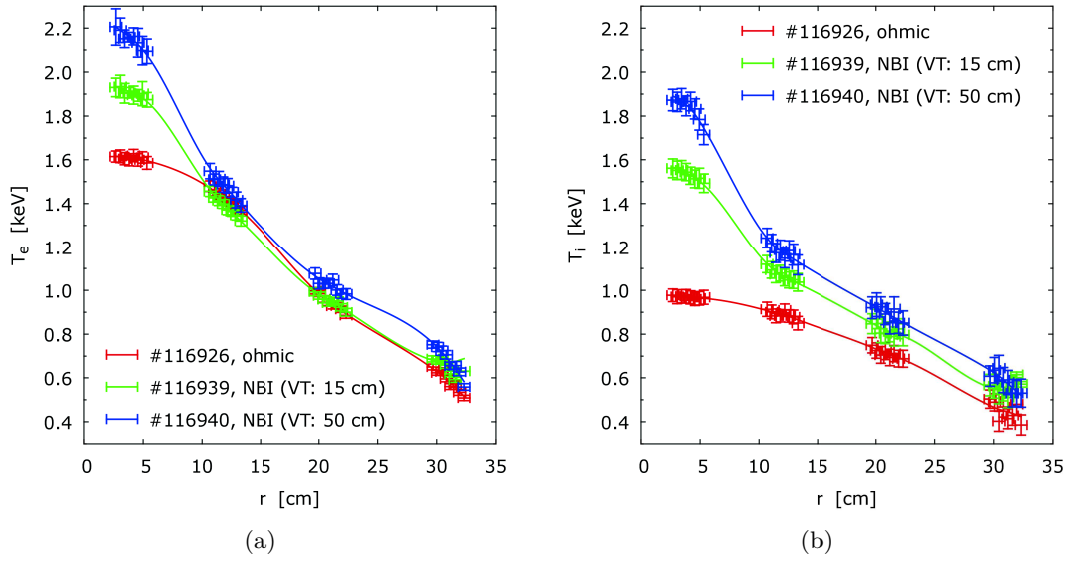


Figure 6.2: Electron temperature profiles (a) and ion temperature profiles (b) measured during ohmic and neutral beam heated TEXTOR discharges with a constant electron density of  $\bar{n}_e = 2.5 \cdot 10^{13} \text{ cm}^{-3}$ .

shows  $T_i(r)/T_i(r = 0 \text{ cm})$  plotted against  $n_e(r)/n_e(r = 0 \text{ cm})$  for several ohmic discharges.

As discussed in section 3.3.1, the focusing of the spectral lines depends on the wavelengths. According to figure 4.6(b) on page 46, the instrumental line broadening is expected to be minimal for the lines **x** and **y** ( $\Delta T_i(x, y) \approx 90 \text{ keV}$ ), while for the lines **w** and **z** a similar broadening of  $\Delta T_i(w, z) \approx 250 \text{ keV}$  is expected. The ion temperature profiles obtained from **w**, **x+y** and **z**, respectively, are illustrated in figure 6.3(b). The line specific temperature offset  $\Delta T_i(\lambda)$  is taken into account. The results show good agreement. Only on the outermost channels  $T_i(x, y)$  becomes unstable due to weak line intensities.

### The ion temperature compared to CXRS-measurements

The ion temperature profiles obtained from  $K_\alpha$ -imaging can be compared to earlier CXRS measurements that were performed at the plasma edge of TEXTOR. Schorn et al. [68] injected high energetic lithium atoms into the plasma boundary in order to study the spectral emission following charge exchange reactions with fully ionized carbon ions. The results for ohmic and beam heated discharges are plotted in figure 6.4. Obviously, CXRS and  $K_\alpha$ -imaging are consistent in both cases. However, although the lithium injector is considered as probing beam without relevant heating power, the pure ohmic character of the analyzed discharge is questionable.

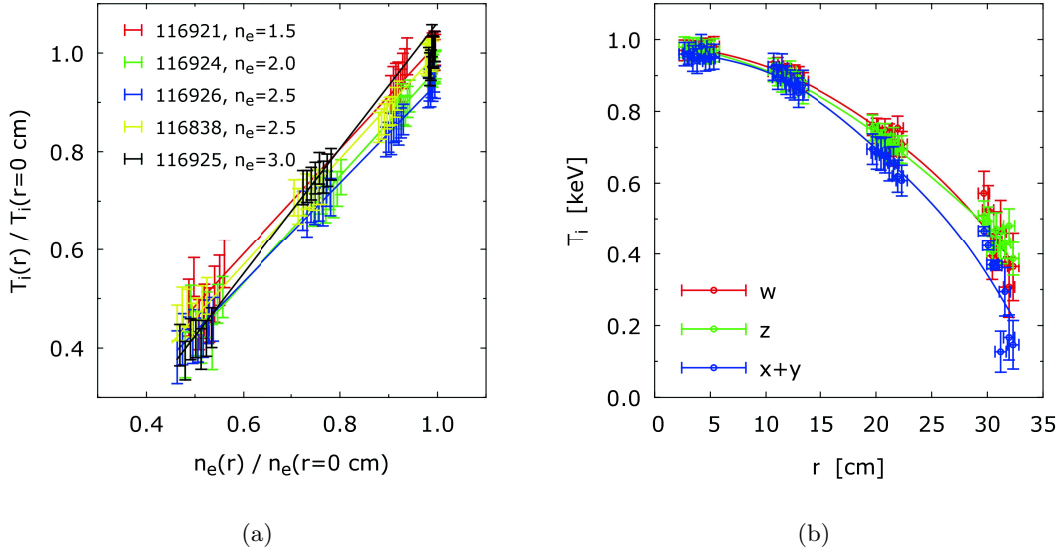


Figure 6.3: **a)** The ion temperature profiles  $T_i(r)$  plotted against the electron density profiles  $n_e(r)$ . In all analyzed ohmic discharges  $T_i(r)$  is found to be proportional to  $n_e(r)$ . **b)** Argon ion temperature determined from the lines **w**, **x+y** and **z**, respectively. The wavelength dependent line broadening is taken into account according to figure 4.8 on page 48.

### The electron temperature compared to ECE-results

The reference for electron temperature measurements at TEXTOR is the electron cyclotron emission diagnostic (ECE) [69]. The  $T_e$ -profile shapes obtained from the ECE diagnostic ( $T_e(ECE)$ ) and from X-ray imaging ( $T_e(K_\alpha)$ ) agree almost perfectly. This is illustrated in figure 6.5(a) in red and black, respectively. However, in all analyzed discharges  $T_e(K_\alpha)$  exceeds  $T_e(ECE)$  by an almost constant offset of ca. 200 eV. In the following, different potential sources of error in  $T_e(K_\alpha)$  are discussed.

The sight-line integrated X-ray signals, are taken into account by performing a forward integration along the emission profiles of the argon ions in TEXTOR (see section 3.3.1). Alternatively, the spectra can be interpreted assuming punctual radiation sources for each line-of-sight. Indeed, skipping the forward integration leads to a good agreement between ECE and X-ray imaging in the plasma center (figure 6.5(a), blue). But obviously, without integration the profile shape does no longer agree with that from ECE. On the other hand, the argon ion distribution used in the forward integration can be varied. The red curve is based on the argon ion profiles, that were deduced in chapter 5. For comparison the results based on the coronal argon ion balance are shown in green. Apparently, changes of the argon ion profiles have weak influence on the electron temperature and only in the plasma center minor deviations appear.

Furthermore, the sensitivity of the spectrometer might be wavelength dependent. This could for example be caused by shadowing of the low or the high energy end of the

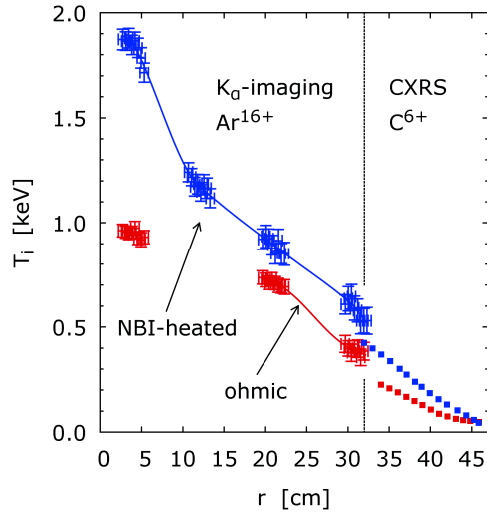


Figure 6.4: Ion temperature profiles in TEXTOR from CXRS measurements and  $K_{\alpha}$ -imaging. Results for ohmic discharges with  $\bar{n}_e = 3 \cdot 10^{13} \text{ cm}^{-3}$  are shown in red. Results for beam heated discharges at  $\bar{n}_e = 2.5 \cdot 10^{13} \text{ cm}^{-3}$  and full beam power are shown in blue. The CXRS measurements are performed during co-beam heating, while the  $K_{\alpha}$ -spectra are measured during counter-beam heating. The CXRS data is rearranged from Schorn et al. [68].

spectrum. In case of a shadowed  $\mathbf{k}$ -satellite the  $K_{\alpha}$ -spectra might give misleading high  $T_e$ -values. A possible shadowing can be investigated by comparing the electron temperatures obtained from the  $\mathbf{k}$ -satellite and the higher order dielectronic satellites  $\mathbf{n}_3$  (section 3.3.1). Both lines  $\mathbf{k}$  and  $\mathbf{n}_3$  are located at either ends of the spectral sketch, so that in case of shadowing discrepancies between  $T_e(\mathbf{k})$  and  $T_e(\mathbf{n}_3)$  should occur. As shown in figure 6.5(b), both  $T_e$ -profiles are in very good agreement. The deviations stay within 5%. Only on the outermost channels,  $T_e(\mathbf{n}_3)$  becomes unstable due to weak line intensities. A shadowed or saturated  $\mathbf{w}$ -line could only result in a too low electron temperature. This proves the homogeneous sensitivity of the spectrometer along the entire observed wavelength region. It further is evidence for consistency in the atomic data for the dielectronic satellites.

The discrepancy between the ECE diagnostic and  $K_{\alpha}$ -imaging cannot be resolved and is left for future investigations.

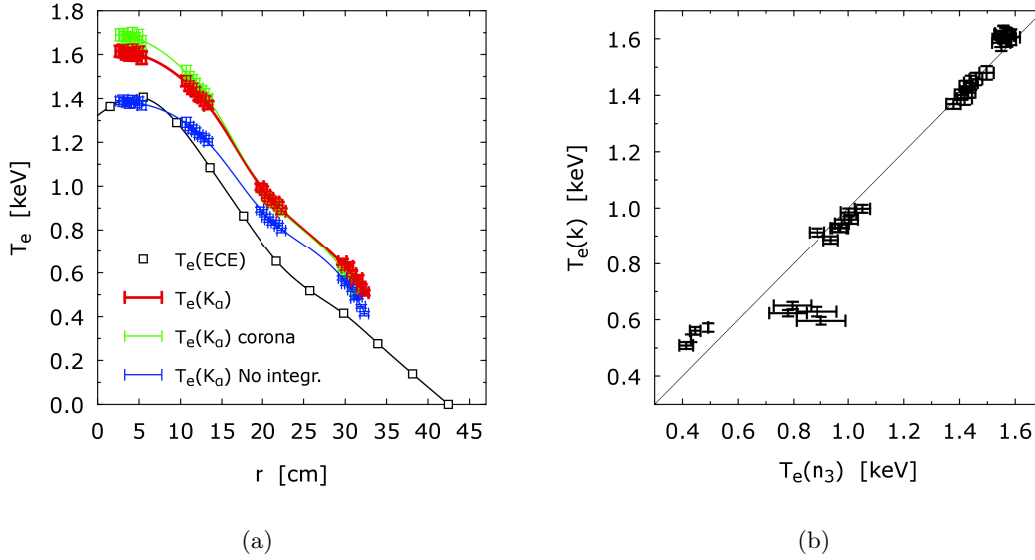


Figure 6.5: **a)** Comparison of the electron temperature profiles from ECE diagnostic (open squares) and from X-ray imaging (red). The profile shapes agree well, while the absolute values deviate by a constant offset of ca. 200 eV. Please note, that the ECE diagnostic scans the plasma horizontally, while the X-ray imaging device provides a vertical scan. The presented  $T_e(ECE)$  is corrected for the Shafranov shift. Without forward integration (blue) the central  $T_e(K_\alpha)$  confirms  $T_e(ECE)$ , but the profile shapes no longer agree. Variations in the argon profiles used in the forward integration have weak impact on  $T_e(r)$  (green). **b)** Comparison of the electron temperature obtained from the dielectronic satellites  $\mathbf{k}$  and  $\mathbf{n}_3$ , respectively (#116924). At the plasma edge the determination of  $T_e(\mathbf{n}_3)$  becomes unstable due to weak line intensities.

## 7 Charge exchange contributions to the Rydberg series of He-like argon

In chapter 5 the influence of charge exchange on the  $K_\alpha$ -spectrum of He-like argon was analyzed. Also other spectral transitions can be affected by charge exchange. In this chapter the influence of charge exchange on the Rydberg series of He-like argon ( $1snp - 1s^2$ ) is investigated. The unique experimental opportunities at TEXTOR are used to perform an experimental verification of the theoretical cross sections for charge exchange at high, CXRS relevant [70] collision energies (section 7.2). Prior to this, the measured spectral lines are shortly introduced, and section 7.1 deals with the determination of the argon ion ratio  $Ar\ xVIII / Ar\ xVII$  from the spectrum. This represents an independent verification of the argon ion ratios obtained in chapter 5.

The Rydberg series is measured along a radial, central chord in TEXTOR, using the vertical channel of the non imaging X-ray spectrometer (HRS, section 4.2.2). Therefore, in contrast to sections 5 and 6 the spectral information is not radially resolved. Simultaneously, the independent horizontal channel of the HRS unit is used to observe the  $K_\alpha$ -emission ( $1s2l - 1s^2$ ).

The wavelength region monitored by the vertical HRS channel extends from about 2.97 Å to 3.10 Å, covering the Rydberg transitions starting from  $n = 6$  up to the ionization limit of singly excited He-like argon at about 3.01 Å. Additionally the  $4p - 1s$  transition in H-like argon is observed at the high energy end. A representative spectrum measured during an ohmic discharge is shown in figure 7.1. Although no wavelength calibration was performed, the observed lines can readily be identified from their wavelength spacing ( $\Delta\lambda \propto 1/n^2 - 1/m^2$ ). The asymmetric deformation of the spectral lines - visible at the low energy sides - is due to depiction errors. Those errors do not affect the photon detection rate, so that apart from overlapping for higher  $n$  quantum numbers, the line intensities can be obtained correctly.

The relative intensities of the Rydberg lines are very well described by the cross sections for excitation from the ground state  $\sigma_{exc}(1snp - 1s^2) \propto 1/n^3$ , as shown in figure 7.2. This is in agreement with findings from Rice et al. [40], who measured equal spectra at ALCATOR. Based on this, the Rydberg transitions measured in the center of ohmic TEXTOR plasmas can be considered as pure excitation lines.

Finally, it shall be noted that the **w**-line ( $1s2p - 1s^2$ ) found in the  $K_\alpha$ -spectrum represents the low energy end ( $n = 2$ ) of the Rydberg series ( $1snp - 1s^2$ ). Therefore, in the following the **w**-line is also referred to as **w**<sub>2</sub>, while the higher Rydberg transitions are labeled **w**<sub>*n*</sub>, accordingly.

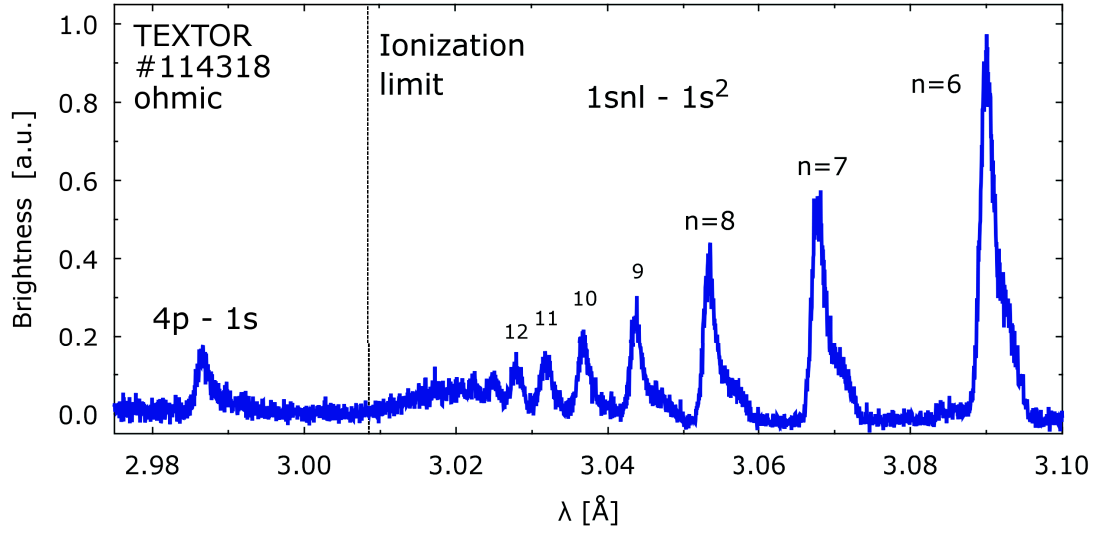


Figure 7.1: Rydberg series of H-like argon measured along a central chord in TEXTOR.

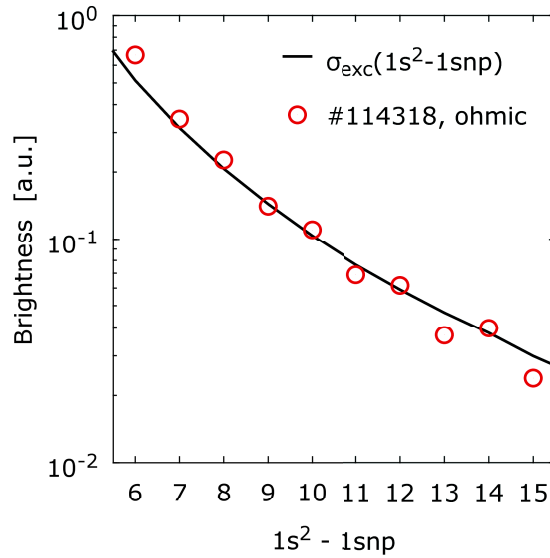


Figure 7.2: Relative brightness of the Rydberg transitions of He-like argon measured during an ohmic discharge in TEXTOR. The experimental line ratios are described well by cross sections for excitation from the ground state, indicating pure excitation lines and negligible cascade contributions from higher energy states.

## 7.1 Determination of the argon ion ratio $Ar\text{ XVIII}/Ar\text{ XVII}$

With the Rydberg series and the  $4p - 1s$  transition, the measured spectrum covers lines emitted from the He-like as well as from the H-like argon stage. This allows to determine the argon ion ratio  $Ar\text{ XVIII}/Ar\text{ XVII}$ .

For the analysis all lines are considered as pure excitation lines. Furthermore, cascade contributions from higher energy levels are neglected. With respect to the Rydberg series, this approximation is supported by figure 7.2. For  $4p - 1s$  the same conditions are assumed. In this picture the intensity ratio  $I_{4p}/I_w$  of the  $4p - 1s$  transition and any of the Rydberg lines  $\mathbf{w}_n$  is given by:

$$\begin{aligned} \frac{I_{4p}}{I_w} &= \frac{\int_0^1 d\rho \langle \sigma \cdot v \rangle_{4p}(\rho) \cdot N(Ar\text{ XVIII})(\rho) \cdot n_e(\rho)}{\int_0^1 d\rho \langle \sigma \cdot v \rangle_w(\rho) \cdot N(Ar\text{ XVII})(\rho) \cdot n_e(\rho)} \\ &= \frac{\hat{N}(Ar\text{ XVIII})}{\hat{N}(Ar\text{ XVII})} \cdot \frac{\int_0^1 d\rho \langle \sigma \cdot v \rangle_{4p}(\rho) \cdot \tilde{N}(Ar\text{ XVIII})(\rho) \cdot n_e(\rho)}{\int_0^1 d\rho \langle \sigma \cdot v \rangle_w(\rho) \cdot \tilde{N}(Ar\text{ XVII})(\rho) \cdot n_e(\rho)} \\ \Leftrightarrow \frac{\hat{N}(Ar\text{ XVIII})}{\hat{N}(Ar\text{ XVII})} &= \frac{I_{4p}}{I_w} \cdot \frac{\int_0^1 d\rho \langle \sigma \cdot v \rangle_w(\rho) \cdot \tilde{N}(Ar\text{ XVII})(\rho) \cdot n_e(\rho)}{\int_0^1 d\rho \langle \sigma \cdot v \rangle_{4p}(\rho) \cdot \tilde{N}(Ar\text{ XVIII})(\rho) \cdot n_e(\rho)}. \end{aligned} \quad (7.1)$$

Here the absolute argon ion density profiles  $N(Ar)(\rho)$  were factorized into the central values  $\hat{N}(Ar)$  and the normalized argon density profiles  $\tilde{N}(Ar)(\rho)$ :

$$\begin{aligned} N(Ar\text{ XVII})(\rho) &= \hat{N}(Ar\text{ XVII}) \cdot \tilde{N}(Ar\text{ XVII})(\rho) \\ N(Ar\text{ XVIII})(\rho) &= \hat{N}(Ar\text{ XVIII}) \cdot \tilde{N}(Ar\text{ XVIII})(\rho), \end{aligned}$$

while the  $\tilde{N}(Ar)(\rho)$  are used as found in chapter 5 for ohmic discharges. The rate coefficients for excitation from the ground state  $\langle \sigma \cdot v \rangle$  are based on cross sections produced with the **F**lexible **A**tomistic **C**ode (FAC, [13]). They are shown in figure 7.3(a) for selected transitions.

Several ohmic and beam heated discharges with different plasma densities are analyzed. For each discharge the intensity ratio  $I_{4p}/I_w$  is evaluated for all Rydberg lines ( $6 \leq n \leq 14$ ). The results for different  $\mathbf{w}_n$  agree well and are averaged over  $n$ . The obtained argon ion ratios are shown in figure 7.3(b). For ohmic and beam heated discharges  $Ar\text{ XVIII}/Ar\text{ XVII}$  is found between 15% and 25% in all cases. This is in good agreement with the findings from  $K_\alpha$ -imaging, where values between 10% and 20% are observed. Neither of the methods reveal a monotonic density dependence of  $Ar\text{ XVIII}/Ar\text{ XVII}$ . The evaluation of the Rydberg series represents an independent verification of the results from  $K_\alpha$ -imaging, as here only excitation lines are involved. In contrast the  $Ar\text{ XVIII}/Ar\text{ XVII}$  values from  $K_\alpha$ -imaging are based on the recombination parts of the spectral lines.

## 7.2 Charge exchange on the Rydberg states of He-like argon

Contributions from charge exchange recombination to the Rydberg series of highly ionized plasma impurities have been observed at different tokamaks. Rice et al. [40] found

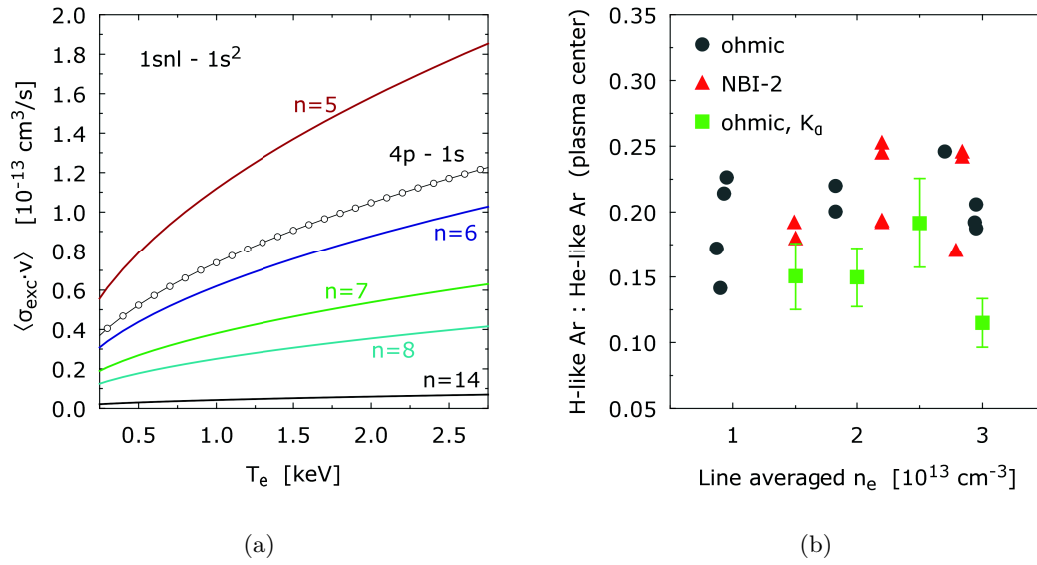


Figure 7.3: **a)** Rate coefficients for excitation from the ground state for He-like and H-like argon. The cross sections are calculated with FAC [13]. **b)** Argon ion ratios  $Ar\ XVIII/Ar\ XVII$  obtained from the relative intensities of the He-like Rydberg series ( $1snp - 1s^2$ ) and the H-like  $4p - 1s$  line. For comparison the values obtained from  $K_\alpha$ -imaging are shown in green.

a selective peaking of  $w_9$  and  $w_{10}$  in the Rydberg series of He-like argon measured along an off center chord in ALCATOR (figure 7.4). The effect was only found at the plasma edge, where due to low temperatures the excitation rates are weak and the neutral particle background is stronger than in the plasma center. Furthermore, the effect could clearly be assigned to charge exchange with thermal atomic hydrogen by comparing independent measurements in hydrogen and helium plasmas. In helium plasma, where the neutral particle abundance is generally strongly reduced, the effect did not occur. A similar finding was reported by Hedqvist et al. [34] for the Rydberg series of H-like chlorine measured in JET plasmas.

The characteristic impact on  $w_9$  and  $w_{10}$  is in qualitative agreement with the theory of charge exchange, which predicts a resonance in the cross sections for  $n \approx 10$  (compare equation 3.9 on page 17). However, the effects seen at ALCATOR and JET are related to charge exchange with thermal background neutrals. This means the CX-reactions take place at collision energies in the order of  $2 \text{ keV}$  or below. For higher collision energies an experimental verification of the charge exchange cross sections has up to now not been performed. This is especially important for the energy region of  $20 - 100 \text{ keV}$ , where the neutral diagnostic beams for CXRS operate in order to penetrate deeply into the plasma. For these energies no experimental data exist and the available theoretical cross sections show significant deviations (see figure 3.1(b) on page 18). The uncertainties in the CX-cross sections currently restrict the accuracy of absolute impurity density measurements based on CXRS.

The unique diagnostic opportunities at TEXTOR allow to observe the Rydberg series of He-like argon under the influence of charge exchange with high energy hydrogen atoms that are injected by a  $50 \text{ keV}$  heating beam. The observed enhancement of the Rydberg lines allows attribution of the effective rate coefficients for charge exchange  $Q_{cx}(1snp - 1s^2)$ . This enables the first experimental verification of the fine-structure resolved cross sections for charge exchange at CXRS relevant energies. The observed spectral region allows to investigate the charge exchange effects on  $w_{\geq 6}$ . With the simultaneously measured  $K_\alpha$  spectrum additionally  $w_2$  can be analyzed.

**Experimental Setup** TEXTOR is equipped with two tangential neutral heating beams NBI-1 and NBI-2 that operate at a maximal energy of  $E_b = 50 \text{ keV}$  (see section 4.1 for details). While the beam line of NBI-1 intersects the sight-line of the HRS spectrometer, NBI-2 is located at the far side of the torus (compare figure 4.1(a) on page 39). Operating only one injector at a time, allows to realize identical plasma scenarios, while only in NBI-1-mode the X-ray spectrometer observes the active beam zone. From the differences in the line intensities measured in the two plasma scenarios, the charge exchange contributions on the spectral lines can be quantified. The setup is illustrated in figure 7.5. As NBI-1 and NBI-2 are designed as co- and counter-beams, respectively, the plasma current has to be inverted to match the beam direction in both cases. With identical beam settings, NBI-1 and NBI-2 will affect the global plasma parameters equally. This especially includes the argon ion balance, ensuring comparability of the two cases. Yet for a correct interpretation of the charge exchange contributions from NBI-1 it is

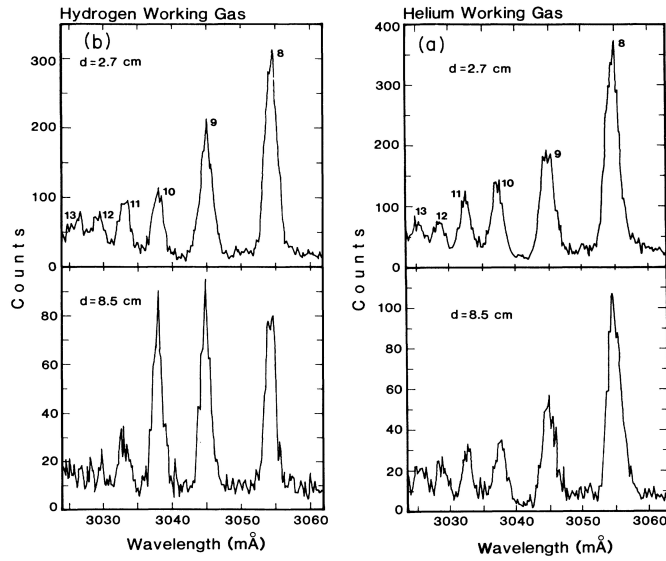


Figure 7.4: Contributions from charge exchange with thermal background neutrals to the Rydberg series of  $Ar^{16+}$  measured at ALCATOR. Reprinted figure with permission from Rice et al., Phys. Rev. A: At., Mol., Opt. Phys. 35, 7, 3033 (1987). Copyright (2014) by the American Physical Society.

important, that the direct CX-impact on the Rydberg lines is a local effect, that only occurs close to the active beam zones. This precondition is well fulfilled, as the life-times of the excited argon states are in the order of  $\tau \approx 10^{-12}$  s, while the toroidal time of rotation is in the order of  $T_\phi \approx 10^{-5}$  s. This ensures that the measured spectra are not affected by direct CX-contributions from NBI-2.

**Experimental Data** Figure 7.6 shows the  $K_\alpha$ -spectrum and the Rydberg series of He-like argon measured at two different plasma densities. The spectra measured during NBI-1 operation are shown in red, the reference spectra measured in NBI-2 mode are shown in blue. Both, the  $K_\alpha$ -spectrum as well as the Rydberg series show significant CX-impact during NBI-1 operation. Within the  $K_\alpha$ -spectrum only the He-like lines **w**, **x**, **y** and **z** are increased, while the triplet (**x**, **y**, **z**) is stronger affected than the singlet **w**. The Li-like satellites stay unchanged, as their doubly excited upper states cannot be populated by charge exchange. Furthermore, their constant intensities indicate equal plasma parameters. Towards higher plasma densities, the CX-impact on the  $K_\alpha$ -spectrum clearly decreases.

The enhancement of the Rydberg series is generally weaker than observed in the measurements at ALCATOR and JET, but is not as sharply restricted to certain lines. While in figure 7.4 an exclusive peaking of **w**<sub>9</sub> and **w**<sub>10</sub> is visible, the CX-impact in figure 7.6(b) has a maximum around **w**<sub>8,9</sub>, which decreases smoothly towards higher and lower  $n$ . This difference is in agreement with the theory of charge exchange, that

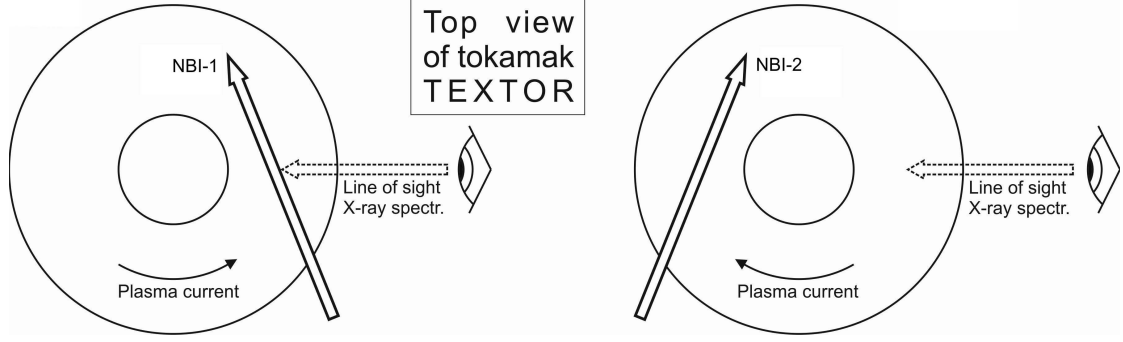


Figure 7.5: The experimental setup for measuring the charge exchange effects in the high Rydberg series of He-like argon at high collision energies ( $E_b = 16.7, 25, 50 \text{ keV}$ ). By inverting the plasma current, two identical neutral beam heated plasma scenarios are realized using NBI-1 and NBI-2, respectively. Only during NBI-1 operation the spectrometer observes the active beam zone, while NBI-2 operation is used for reference measurements.

predicts a broadening of the  $n$ -resonance in the cross sections towards higher collision energies (compare figure 3.3 on page 19). For  $12 \leq n \leq 14$  the CX-impact is weak and falls below the detection limit. The high energy tail of the Rydberg series starting from  $n = 15..∞$  is again strongly increased.

In contrast to the  $K_\alpha$ -spectrum, the CX-impact on the Rydberg series does not decrease towards higher plasma densities. Furthermore, the maximum at  $n = 8, 9$  appears to smear out towards lower  $n$ .

For a safe comparison of NBI-1 mode and NBI-2 mode, the spectra need to be normalized in order to eliminate eventual differences in the total amount of argon in the plasma. In case of the  $K_\alpha$ -spectrum the normalization factor is chosen to be

$$\Lambda = I_k \cdot \frac{Q_{exc,w}(T_e) + Q_{exc,x}(T_e) + Q_{exc,y}(T_e) + Q_{exc,z}(T_e)}{Q_{dr,k}(T_e)}, \quad (7.2)$$

where  $I_k$  is the intensity of the  $\mathbf{k}$ -satellite and  $Q_{exc}$  and  $Q_{dr}$  are the effective rate coefficients for excitation from the ground state and dielectronic recombination, respectively. The  $\mathbf{k}$ -satellite stays unaffected by charge exchange recombination and therefore represents a reference line. As the intensity of  $\mathbf{k}$  relative to the  $K_\alpha$ -lines is temperature dependent,  $\Lambda$  further includes the ratio of  $Q_{exc}$  and  $Q_{dr}$  to correct for minor temperature differences between the discharges.

In case of the Rydberg series no such reference line is available. The  $4p - 1s$ -line is a critical option, as interference by charge exchange with bare argon cannot be excluded in NBI-1 operation. Therefore, the Rydberg series is normalized on the total count rates registered by the data acquisition during the entire integration time.

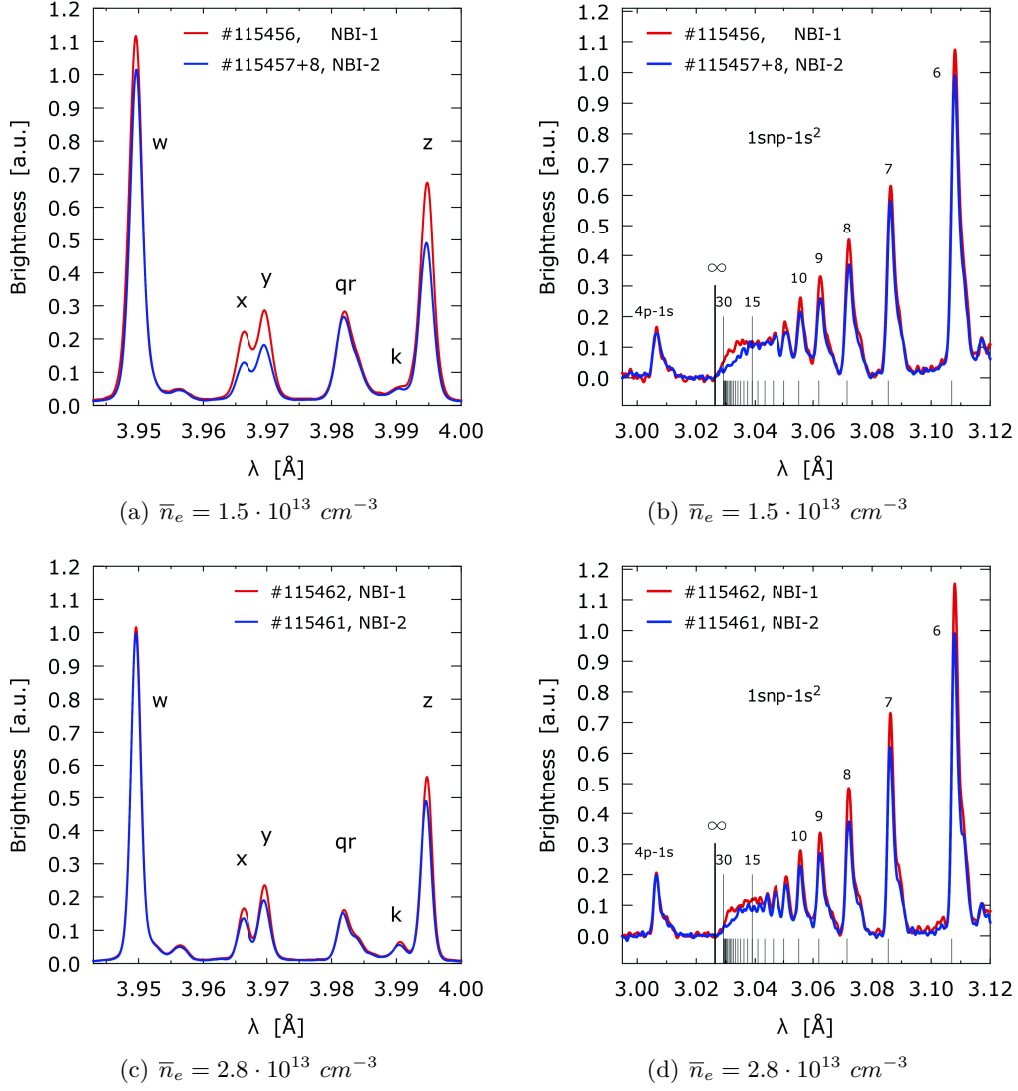


Figure 7.6: Charge exchange impact on the  $K_\alpha$ -spectrum and the Rydberg series of He-like argon for two different plasma densities. The displayed Rydberg spectra are smoothed using splines.

**Charge exchange impact on the  $K_\alpha$ -spectrum** As visible in figure 7.6, the contributions from charge exchange with the beam neutrals decrease towards higher plasma densities. In the following this density dependence is analyzed quantitatively.

Figure 7.7(a) shows the summed up intensities of the  $K_\alpha$ -lines ( $\mathbf{w}, \mathbf{x}, \mathbf{y}, \mathbf{z}$ ) as a function of the plasma density. Superposed satellites were subtracted by fitting the spectra as described in section 3.3.1.

During NBI-1 operation the measured line intensities are generally higher than those measured in NBI-2 mode. The difference decreases towards higher plasma densities, which is in qualitative agreement with a decreasing  $n_0/n_e$  ratio due to stronger beam attenuation and constant beam power.

Yet, also in NBI-2 operation the normalized line intensities slightly increase instead of staying constant, as it would be expected for pure excitation lines. This is most likely due to passive charge exchange with thermal atomic hydrogen, which can easier penetrate into the plasma center at lower plasma densities. This is in agreement with the results from chapter 5, where the amount of recycling neutrals relative to  $n_e$  was found to increase towards lower plasma densities. However, this effect must appear in both beam scenarios and therefore has no further meaning for the interpretation of the experimental data.

For a more detailed analysis we consider the intensity ratio between measurements in NBI-1 mode ( $I_1$ ) and NBI-2 mode ( $I_2$ ). Apart from the CX-contributions we assume pure excitation lines. Hence, the intensity ratio of a given transition can be described by the following term:

$$\begin{aligned} \frac{I_1}{I_2} &= \frac{Q_{exc} \cdot n_e \cdot N(Ar\ XVII) + Q_{cx} \cdot n_b \cdot N(Ar\ XVIII)}{Q_{exc} \cdot n_e \cdot N(Ar\ XVII)} \\ \Leftrightarrow \frac{I_1}{I_2} - 1 &= \frac{Q_{cx}}{Q_{exc}} \cdot \frac{n_b}{n_e} \cdot \frac{N(Ar\ XVIII)}{N(Ar\ XVII)}, \end{aligned} \quad (7.3)$$

where  $Q_{exc}$  and  $Q_{cx}$  are the effective rate coefficients for excitation from the ground state and charge exchange, respectively, and  $n_b$  is the density of the beam neutrals. The ion ratio  $Ar\ XVIII/Ar\ XVII$  was found to be approximately constant at 20% (compare figure 7.3(b)). Also  $Q_{cx}/Q_{exc}$  for the  $K_\alpha$ -lines is almost constant within the relevant density range (see section 8). Therefore, according to 7.3, the measured line enhancement should be proportional to the density ratio of beam particles and electrons  $n_b/n_e$ . The quantity  $n_b/n_e$  is estimated using a simple beam attenuation model [25]:

$$n_b(x, n_e, E_b) = N_b \cdot e^{-x \cdot \lambda(E_b) \cdot n_e}, \quad \lambda(E_b) = \frac{1}{\sigma_{ion}(E_b) + \sigma_{cx}(E_b)}. \quad (7.4)$$

After traveling the distance  $x = 180 \pm 20\ cm$  from entering the plasma to the observed volume, the initial beam density  $N_b$  has reduced to  $n_b(x = 180\ cm, n_e)$ . The total cross section for beam attenuation  $\lambda$  is dominated by proton ionization and charge exchange with protons. Both  $\sigma_{ion}$  and  $\sigma_{cx}$  depend on the beam energy  $E_b$ , so that all three beam energy components have to be taken into account. During the experiments the beam was operated with  $E_b = 50\ keV$  at all times, corresponding to the three energy components

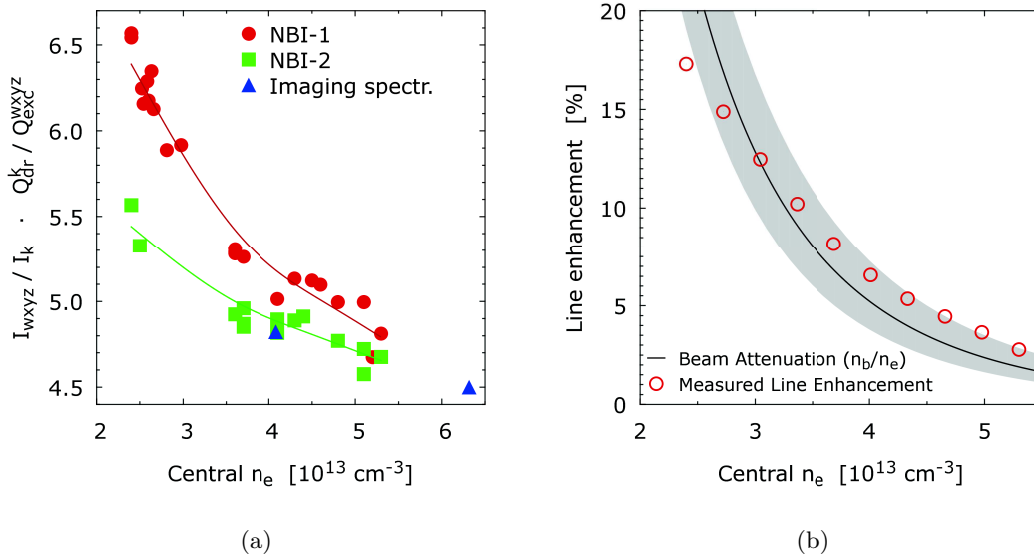


Figure 7.7: **a)** Charge exchange impact on the  $K_\alpha$ -spectrum of He-like argon as a function of the plasma density. Integrated line intensities (**w**, **x**, **y**, **z**) observed under direct influence of neutral heating beam NBI-1 (red) compared to reference measurements (NBI-2, green). Data points obtained with the center most channels of the W7-X imaging spectrometer (blue) are consistent with the NBI-2 measurements. In all cases the neutral beam injectors were operated at 50 keV with full beam diameter. **b)** Relative enhancement of the lines **w**, **x**, **y** and **z** caused to charge exchange compared to the calculated density ratio of beam particles and electrons. The observed density dependence is reasonably well described by the estimated beam attenuation.

$E_1 = 50 \text{ keV}$ ,  $E_2 = 25 \text{ keV}$  and  $E_3 = 16.7 \text{ keV}$ . According to experimental results from Marchuk et al. [71], the total beam density in TEXTOR is composed as

$$n_b(\text{tot}) \approx 0.25 \cdot n_b(E_1) + 0.50 \cdot n_b(E_2) + 0.25 \cdot n_b(E_3). \quad (7.5)$$

Taking into account this beam energy mix, one obtains an effective attenuation cross section of

$$\lambda_{eff} = 4.475 \cdot 10^{-16} \text{ cm}^2.$$

Here total ionization and charge exchange cross sections from [17] were used. Figure 7.7(b) compares the observed decay of the CX-impact on the  $K_\alpha$ -lines to the calculated beam attenuation  $(n_b(x, n_e)/n_e)$ . For simplicity the electron density profile along the beam path  $x$  is assumed to be constant. This simple estimate describes the experimental observation reasonably well.

**Charge exchange impact on the Rydberg series** The Rydberg transitions  $1snp - 1s^2$  for  $n \geq 6$  are not superposed by any satellites (as in case of  $K_\alpha$ -spectrum) and their intensities can readily be integrated for a quantitative analysis. The red dots in figure 7.8(a) show the relative line enhancement caused by charge exchange with fast NBI-1 neutrals as obtained from figure 7.6(b) (low plasma density,  $\hat{n}_e = 2.5 \cdot 10^{13} \text{ cm}^{-3}$ ). The line intensities are evaluated individually up to  $n = 14$ . The high energy tail starting from  $n = 15$  up to the ionization limit is considered as a whole. Figure 7.8(a) additionally shows the CX-impact on the  $K_\alpha$   $\mathbf{w}$ -line ( $\mathbf{w}_2$ ). The measurement shows a clear peaking of  $\mathbf{w}_8$  and  $\mathbf{w}_9$ . Towards higher  $n$  the CX-impact decreases and falls below the detection limit for  $n \approx 13$ . The high energy tail is again strongly increased.

According to equation 7.3, the CX-impact is determined by the ratio  $Q_{cx}/Q_{exc}$ . This ratio is illustrated in figure 7.8(b) for  $H(1s)$  and  $H(2l)$  donor atoms. The  $Q_{cx}$  are based on cross sections from Schultz et al. [9, 10]. See chapter 8 for details concerning the calculation of  $Q_{cx}$ . The observed peaking of  $\mathbf{w}_{8,9}$  is in good agreement with CX-theory, though the latter predicts a maximum at  $\mathbf{w}_{7,8}$ . The strong increase of the Rydberg tail cannot be explained by CX from ground state atoms alone. Actually, the influence of charge exchange can roughly be separated into the regions  $n \leq 15$  for  $H(1s)$  donor atoms and  $n \geq 15$  for  $H(2l)$  donor atoms. In order to include charge exchange from excited donor atoms, equation 7.3 needs to be extended to:

$$\begin{aligned} \frac{I_1}{I_2}(n) &= \left[ Q_{exc}(n) \cdot n_e \cdot N(Ar\text{ XVII}) \right. \\ &\quad \left. + \left( Q_{cx}^{1s}(n) \cdot n_b(1s) + Q_{cx}^{2l}(n) \cdot n_b(2l) \right) \cdot N(Ar\text{ XVIII}) \right] \\ &\quad \cdot \left( Q_{exc} \cdot n_e \cdot N(Ar\text{ XVII}) \right)^{-1} \end{aligned} \quad (7.6)$$

$$\begin{aligned} \Leftrightarrow \frac{I_1}{I_2}(n) - 1 &= \frac{Q_{cx}^{1s}(n) + Q_{cx}^{2l}(n) \cdot \frac{n_b(2l)}{n_b(1s)}}{Q_{exc}(n)} \cdot \frac{n_b(1s)}{n_e} \cdot \frac{N(Ar\text{ XVIII})}{N(Ar\text{ XVII})} \\ &= \frac{Q_{cx}^{1s}(n) + Q_{cx}^{2l}(n) \cdot \frac{n_b(2l)}{n_b(1s)}}{Q_{exc}(n)} \cdot \frac{N_b(1s) \cdot e^{-x \cdot \lambda \cdot n_e}}{n_e} \cdot \frac{N(Ar\text{ XVIII})}{N(Ar\text{ XVII})}. \end{aligned}$$

Here  $n_b(1s)$  and  $n_b(2l)$  are the densities of  $H(1s)$  and  $H(2l)$  beam atoms in the observed plasma volume and  $Q_{cx}^{1s}(n)$  and  $Q_{cx}^{2l}(n)$  are the corresponding effective rate coefficients for charge exchange. Furthermore,  $N_b$  is the initial beam density at the LCFS according to equation 7.4.

Equation 7.6 can be fitted to the experimental data, using only the initial beam density  $N_b$  and the fraction of excited beam particles  $n_b(2l)/n_b(1s)$  as free parameters. For  $n < 15$  only CX from  $H(1s)$  is relevant, and best agreement is achieved for  $N_b = 1.5 \cdot 10^8 \text{ cm}^{-3}$ , as plotted in black in figure 7.8(a). This compares well to results from efficiency modeling for the neutral particle injectors at TEXTOR [67], which predict an initial beam intensity of  $N_b = 1.0 \cdot 10^8 \text{ cm}^{-3}$  for the energy composition given in equation 7.5. For the above evaluation the argon ion ratio was assumed to be  $N(Ar\text{ XVIII})/N(Ar\text{ XVII}) \approx 0.2$ , according to the experimental results shown in figure 7.3(b).

At this point the good agreement between  $\mathbf{w}_2$  and  $\mathbf{w}_{\geq 6}$  shall be emphasized. While the

CX impact on  $\mathbf{w}_{\geq 6}$  is mainly caused by direct population ( $\sigma_{cx}(np)$ ),  $\mathbf{w}_2$  is only affected by cascade contributions from higher  $n$ . These cascade contributions mainly come from higher  $l$ -states, so that by comparing the CX-impacts on  $\mathbf{w}_2$  and  $\mathbf{w}_{\geq 6}$ , the cross sections  $\sigma_{cx}(np)$  and  $\sigma_{cx}(n, l > 1)$  are related.

To reproduce the observed enhancement of the Rydberg tail based on charge exchange with  $H(2l)$  donor atoms, an excited beam fraction of  $n_b(2l)/n_b(1s) \approx 5\%$  is needed. This value is about a factor of 20 higher than predicted by recent beam population models [72, 73]. Yet these models also predict relevant population densities for higher excited beam states. The cross sections for charge exchange from excited donor atoms  $\sigma_{cx}[H(n)]$  scale with  $n^4$  [17]. Therefore, the total effective rate coefficients for charge exchange from excited beam atoms strongly increase, when higher excited states are included. When the excited beam states up to  $H(n = 10)$  are taken into account according to population densities from [73], the total excited beam fraction needed to describe the spectra reduces to  $\sum_{n=2}^6 n_b(n)/n_b(1s) \approx 0.4\%$ . This is in good agreement with the theoretical reference value of ca. 0.5% given by [73]. The effective rate coefficients for charge exchange from  $H(n > 2)$  atoms were estimated from the  $Q_{cx}^{2l}(1snp - 1s^2)$  using the scaling law for the  $\sigma_{cx}[H(n)]$  mentioned above. A detailed calculation is not possible, as fine-structure resolved cross section data for  $H(n > 2)$  donor atoms is so far not available. Further details are discussed in section 8.

For low plasma density the CX-impact on the Rydberg series can be described well on basis of the calculated effective rate coefficients. However, the agreement for higher plasma densities is less good. In contrast to the  $K_\alpha$ -spectrum, the Rydberg lines do not show a clear reduction of the CX-impact towards higher plasma densities. Instead, the relative line enhancement for  $n < 15$  stays approximately constant, while the resonance at  $\mathbf{w}_{8,9}$  seems to broaden towards lower  $n$  (figure 7.9). At the same time, the impact on the Rydberg tail reduces. This density dependence cannot be reproduced within the applied model. The observed broadening of the resonance at  $\mathbf{w}_{8,9}$  is in qualitative agreement with an increase of the  $Q_{cx}^{2l}(1snl - 1s^2)$  towards higher plasma densities. Although this is indeed predicted by the collisional radiative modeling (see chapter 8), quantitative agreement is not achieved. This might be due to the CX-contributions from  $H(n > 2)$  donor atoms that could only be estimated on basis of the  $Q_{cx}$  for  $H(n = 2)$ . A more detailed interpretation of the measurements at high plasma density requires new CX-cross section data and is left for future investigations.

**Conclusion** The unique experimental possibilities at TEXTOR have been used to directly measure the charge exchange impact from high energetic neutral particles on the X-ray spectra of He-like argon.

The observed effect is in good agreement with the effective rate coefficients for charge exchange that were calculated using the theoretical cross sections from Schultz et al. [9, 10]. The absolute values of the  $Q_{cx}(1snp - 1s^2)$  are consistent with the density of the neutral beam particles predicted by [67]. Also the  $n$ -dependence of the cross sections is well reproduced. Furthermore, the consistency between  $\mathbf{w}_2$  ( $K_\alpha$ -spectrum) and

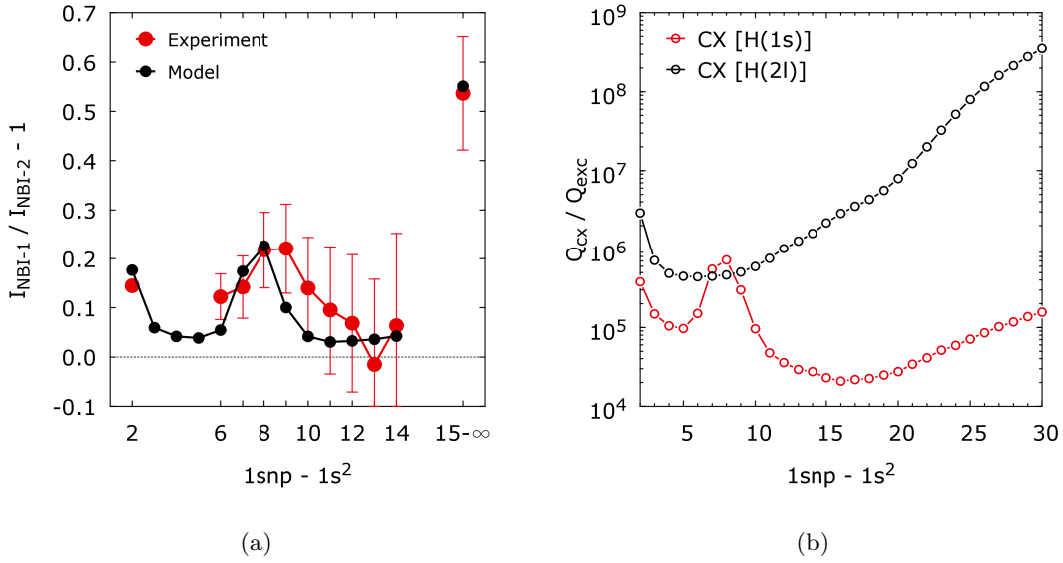


Figure 7.8: **a)** Measured and modeled charge exchange impact on the Rydberg series of He-like argon. The experimental values were obtained from the spectra shown in figure 7.6(a) and 7.6(b). The error bars indicate statistical errors. The modeling results represent the best fit of equation 7.6. **b)** Ratios of the effective rate coefficients for charge exchange and excitation from the ground state for the Rydberg series of He-like argon. The plot shows calculations for  $H(1s)$  (red) and  $H(2l)$  (black) donor atoms. A plasma density of  $n_e = 2.5 \cdot 10^{13} \text{ cm}^{-3}$  and a beam energy composition according to equation 7.5 is assumed. Furthermore, in case of  $H(2l)$  donor atoms statistical population of the fine-structure levels of  $n = 2$  is assumed.

the higher Rydberg lines  $w_{\geq 6}$  confirms the  $l$ -dependence in the theoretical data. This represents the first experimental verification of fine structure resolved CX-cross sections at CXRS relevant collision energies.

The CX-impact on the high Rydberg tail finally allows to estimate the fraction of excited beam atoms revealing good agreement with recent beam models [72, 73]. The obtained excited beam fraction of roughly 0.4% proofs the absence of meta stable states in atomic hydrogen beams that are often mentioned in literature.

For reproducing the experimental findings, significant CX-contributions from  $H(n > 2)$  donor atoms are required. This rises the question, whether contributions from  $H(n \geq 2)$  might as well be relevant for transitions typically used in CXRS (e.g.  $n = 16 \rightarrow n = 15$  in H-like argon). On the one hand, this would necessitate fine-structure resolved cross sections for CX from  $H(n \geq 2)$ . On the other hand, it would complicate impurity density measurements via CXRS, as the results would depend on the population distribution of the excited beam states.

The charge exchange contributions to the Rydberg series show a significant dependence

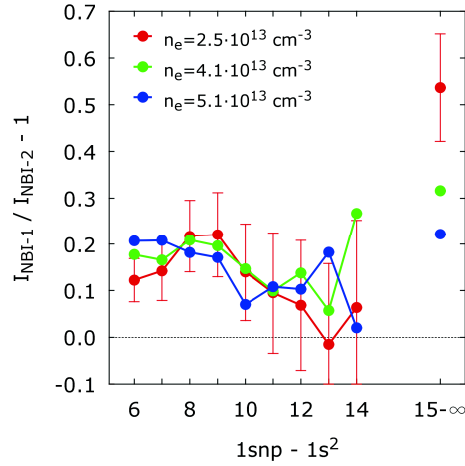


Figure 7.9: The charge exchange impact on the Rydberg series measured at three different plasma densities. In contrast to the  $K_\alpha$ -spectrum no clear decay of the CX-contributions towards higher densities is observed. Instead the CX-resonance at  $n = 8, 9$  shows a broadening towards lower  $n$ . The CX-impact on the high energy tail of the Rydberg series ( $n \geq 15$ ) reduces relative to the impact on  $n < 15$ .

on the plasma density. This dependence is in qualitative agreement with the modeled effective rate coefficients  $Q_{cx}(1snp - 1s^2)$ . Still, the experimental spectra measured at higher densities could not be reproduced quantitatively.

Lastly, the argon ion ratio  $Ar\ XVIII/Ar\ XVII$  was determined from the  $1s - 4p$  transition in H-like argon and the Rydberg transitions in He-like argon. The results confirm the findings from chapter 5. This represents an independent verification of the interpretation of the radially resolved  $K_\alpha$ -spectra and gives further confidence in the presented neutral particle density measurement.

## 8 The effective rate coefficients for charge exchange on the Rydberg series of He-like argon

In chapter 7 an experimental verification of the charge exchange cross sections for high collision energies was presented. The Rydberg series of He-like argon was observed within the beam zone of a neutral particle injector, in order to analyze the line enhancement caused by charge exchange with the beam neutrals. For the evaluation of the experiment, the corresponding effective rate coefficients for charge exchange  $Q_{cx}(1snp - 1s^2)$  are required. These are produced within a hydrogenic approximation of the singly excited He-like argon states, using the collisional radiative model NOMAD. In this chapter the calculation of the effective rate coefficients is discussed in detail.

### 8.1 Hydrogenic approximation of the Rydberg series of He-like argon

The Rydberg series is part of the para helium system (singlet system), as the ground state  $1s^2(^1S_0)$  and all upper levels  $1snp(^1P_1)$  are singlet states. Para helium is almost completely decoupled from ortho-helium (triplet system). Furthermore, for highly excited He-like states the inner electron can in good approximation be considered as part of the atomic core. This allows to describe singly excited para helium in a H-like system with an effective core charge  $\bar{z} = z - 1$ .

In theory charge exchange cross sections are handled in semi classical models (e.g. CTMC), and the CX-cross sections are not spin-sensitive. Therefore, the CX-cross sections need to be statistically distributed over the triplet and the singlet system of He-like argon. According to the statistical weights of the singlet and triplet states ( $g_s/g_t = 1/3$ ), only one fourth of the  $nl$ -resolved CX-cross sections falls upon the singlet system. The  $nl$ -resolved CX-cross sections [10] used in the calculations therefore are divided by four.

In the hydrogenic approximation the effective rate coefficients for charge exchange on the Rydberg series of He-like argon are defined as:

$$Q_{cx} = \frac{N_{\bar{z},np} \cdot A_{np-1s}}{N_{\bar{z}+1} \cdot n_b} \quad , \quad \bar{z} = 16, \quad (8.1)$$

where  $n_b$  is the density of the neutral beam particles and  $N_{\bar{z}}$  and  $N_{\bar{z}+1}$  represent the densities of the hydrogenic and the bare ion, respectively.

## 8.2 The collisional radiative model NOMAD

The effective rate coefficients presented in this chapter are calculated in a quasi-steady state model of a H-like ion system. The H-like ions are handled in fine structure resolution, while only the principle quantum numbers  $n$  and the angular momentum  $l$  are considered individually. For the  $j$ -levels statistical population according to  $g_j = 2 \cdot j + 1$  is assumed.

To calculate the population densities  $N_z(nl)$  the NOMAD code [74, 75] is used. NOMAD is an established collisional-radiative code that allows to model the population distribution of multiple ion stages and their excited states for one trace impurity element in an homogeneous plasma environment (0-dimensional). For the problem at hand NOMAD takes into account only the H-like ion stage ( $z$ ) and the bare ion stage ( $z+1$ ) of the trace impurity. Within the H-like stage the fine-structure levels are considered up to  $n = 30$ , while radiative or collision induced transitions among the energy levels are restricted to dipole allowed processes. Collisions between impurity ions are neglected. The cross sections for de-/excitation by electron collisions are based on the semi empirical formula proposed by van Regemorter [15]. The cross sections for de-/excitation by proton collisions are based on the impact parameter method [18, 76]. The required oscillator strengths are produced with the **F**lexible **A**tomic **C**ode (FAC) [13]. Furthermore, collisional ionization is accounted for on basis of recommended data by Lennon et al. [77]. The cross sections for high energetic charge exchange collisions are taken from Schultz et al. [10]. According to results from recent beam-into-gas experiments at TEXTOR [71], the neutral particle beam is assumed to have the following energy composition:

$$n_b(tot) = 0.25 \cdot n_b(50 \text{ keV}) + 0.50 \cdot n_b(25 \text{ keV}) + 0.25 \cdot n_b(15 \text{ keV}), \quad (8.2)$$

where  $n_b(tot)$  is the total beam density. The CX-rate coefficients for this energy mix are shown in figure 8.2 for ground state ( $H(1s)$ ) and excited ( $H(2l)$ ) beam particles.

NOMAD solves the following system of coupled rate equations in steady state:

$$\begin{aligned} \frac{dN_{z,i}}{dt} = 0 &= R_{in} - R_{out} \\ &= \sum_{j>i} A_{j \rightarrow i} \cdot N_{z,j} - \sum_{j<i} A_{i \rightarrow j} \cdot N_{z,i} \\ &+ \sum_{j \neq i} \langle \sigma \cdot \nu \rangle_{de/ex}^{j \rightarrow i} \cdot N_{z,j} \cdot n_e - \sum_{j \neq i} \langle \sigma \cdot \nu \rangle_{de/ex}^{i \rightarrow j} \cdot N_{z,i} \cdot n_e \\ &+ \langle \sigma \cdot \nu \rangle_{cx}^{\rightarrow i} \cdot N_{z+1} \cdot n_0 - \langle \sigma \cdot \nu \rangle_{ion}^{i \rightarrow} \cdot N_z \cdot n_e. \end{aligned} \quad (8.3)$$

For simulating the population distribution caused by charge exchange, all other populating sources like excitation from the ground state or radiative recombination are artificially suppressed in the model. This does not include the collisional redistribution and the cascade contributions among the excited states (compare section 3.1.3). The effective rate coefficients for excitation from the ground state  $Q_{exc}$  are calculated in an analogous manner.

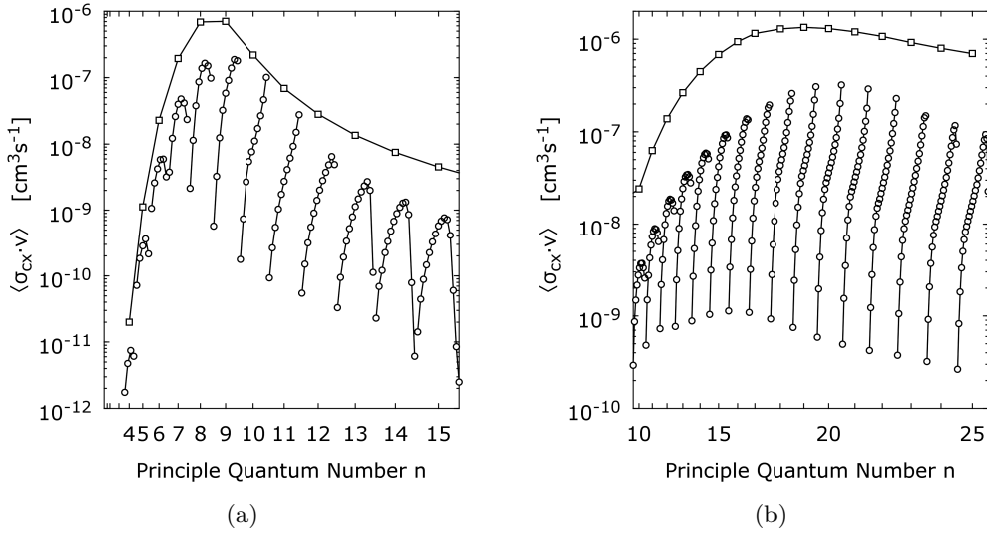


Figure 8.1: Rate coefficients for charge exchange  $[Ar^{17+} \rightarrow Ar^{16+}]$  for a neutral particle energy composition according to equation 8.2. The CX-cross section data is taken from [10]. **a)**  $\langle \sigma_{cx} \cdot v \rangle$  for  $H(1s)$  donor atoms, **b)**  $\langle \sigma_{cx} \cdot v \rangle$  for  $H(2l)$  donor atoms with statistical population of  $n = 2$ .

### 8.3 Results

In this section the effective rate coefficients for the Rydberg series of He-like argon are presented and discussed in detail. The  $Q_{cx}(1snp - 1s^2)$  were calculated for ground state donor atoms ( $H(1s)$ ) as well as for excited donor atoms ( $H(2l)$ ). The case of charge exchange from higher excited donor atoms ( $H(n > 2)$ ) is also considered. The chapter closes with a short paragraph about the effective rate coefficients for excitation from the ground state  $Q_{exc}(1snp - 1s^2)$ .

**Charge exchange from ground state donor atoms H(1s)** Figure 8.2(a) shows the effective rate coefficients  $Q_{cx}(1snp - 1s^2)$  for charge exchange with  $H(1s)$  donor atoms. Calculations for four different plasma densities are plotted. These include a very low density of  $n_e = 10^{10} \text{ cm}^{-3}$ , a very high density of  $n_e = 10^{17} \text{ cm}^{-3}$  and two plasma densities that are realistic for tokamak plasmas ( $n_e = 10^{13} \text{ cm}^{-3}$ ,  $n_e = 10^{14} \text{ cm}^{-3}$ ). In the low density case the corona limit is well fulfilled for all principle quantum numbers up to  $n = 30$ . The high density case illustrates the situation for fine-structure LTE, though for lower  $n$  LTE is still not fully achieved. In all four cases the  $Q_{cx}(1snp - 1s^2)$  have a local maximum at  $n \approx 8$ . This mirrors the  $n$ -resonance in the CX-cross sections (compare figure 8.1(a)). In low density limit the  $Q_{cx}(1snp - 1s^2)$  are dominated by the contributions from the  $np$ -cross sections. This is because on the one hand, collision induced redistribution among the fine-structure levels is negligible, and on the other hand, cascade contributions on the  $p$ -levels with  $n \geq 6$  are

weak. Therefore, the local maximum is exactly located at  $n = 7, 8$ , where the  $\sigma_{cx}(np)$  are maximal (compare figure 8.1(a)). In LTE the  $Q_{cx}(1snp - 1s^2)$  are dominated by the contributions from the  $n$ -cross sections, due to the  $nl$ -statistical redistribution. The local maximum is therefore slightly shifted to  $n = 8, 9$ .

Towards higher  $n$ , the  $Q_{cx}(1snp - 1s^2)$  smoothly decay according to the behavior of the CX-cross sections. However, towards lower  $n$  the  $Q_{cx}(1snp - 1s^2)$  strongly increase, while the CX-cross sections quickly drop off to zero for  $n \leq 6$ . At these low  $n$  the  $Q_{cx}(1snp - 1s^2)$  are mainly supplied by cascade contributions from higher energy levels. It can generally be said that the cascade contributions gain importance towards the lower  $n$ -stages.

Furthermore, figure 8.1(a) shows that the  $Q_{cx}(1snp - 1s^2)$  calculated under LTE conditions are significantly higher than the equivalents calculated under corona conditions. This can also be understood from the collisional redistribution among the fine-structure levels. In corona limit the population density of the  $p$ -levels is approximately determined by the ratio of the rate coefficients  $\langle \sigma_{cx}(np) \cdot v \rangle$  and the lifetime  $A_{np}$ :

$$N_{np}^{cor} \propto \frac{\langle \sigma_{cx}(np) \cdot v \rangle}{A_{np}}.$$

Here cascade contributions are neglected. When the fine-structure levels approach  $(2 \cdot l + 1)$ -statistical distribution, the population density of the  $p$ -levels is constantly kept at  $N_{np} = 3/n^2 \cdot N_n$ . In LTE the population densities of the  $p$ -levels therefore are given by:

$$N_{np}^{lte} \propto \frac{\langle \sigma_{cx}(n) \cdot v \rangle}{A_n} \cdot \frac{3}{n^2}.$$

Due to the strong  $1snp - 1s^2$  dipole transition the total lifetime of any  $n$ -level is dominated by the lifetime of the  $np$ -level. It holds  $A_n \approx A_{np}$ . At the same time, the fine-structure resolved charge exchange cross sections strongly prefer high orbital quantum numbers, so that  $\sigma_{cx}(np) \ll \sigma_{cx}(n)$ . As a consequence, it holds  $N_{np}^{cor} \ll N_{np}^{lte}$  and  $Q_{cx}(1snp - 1s^2)$  increases as soon as collisional redistribution becomes relevant. However, in figure 8.2(a) the difference between low and high density limit obviously reduces towards lower  $n$ . On the one hand, this is because LTE is not fully achieved for the lower  $n$ -states. On the other hand, the population of the lower  $n$ -states mainly arise from cascade contributions, so that the population characteristics in corona limit are not dominated by the strong  $l$ -gradient in the CX-cross sections. The population densities within lower  $n$ -states therefore are not as far from statistical values as in case of higher  $n$ .

The central plasma density in TEXTOR ranges in between the two realistic  $n_e$ -values shown in figure 8.1(a). It is therefore important to mention, that already for  $n_e = 10^{13} \text{ cm}^{-3}$  the corona approximation is violated for high  $n$ -level. On the other hand, even at  $n_e = 10^{14} \text{ cm}^{-3}$  corona conditions are well fulfilled for  $n \leq 15$ .

As mentioned above, the  $np$ -cross sections  $\sigma_{cx}(np)$  represent only a tiny fraction of the  $n$ -cross sections  $\sigma_{cx}(n) = \sum_{l=0}^{n-1} \sigma_{cx}(nl)$ . Still, according to the above argumentation, the  $Q_{cx}(1snp - 1s^2)$  are dominated by the  $\sigma_{cx}(np)$  at all fusion relevant plasma densities.

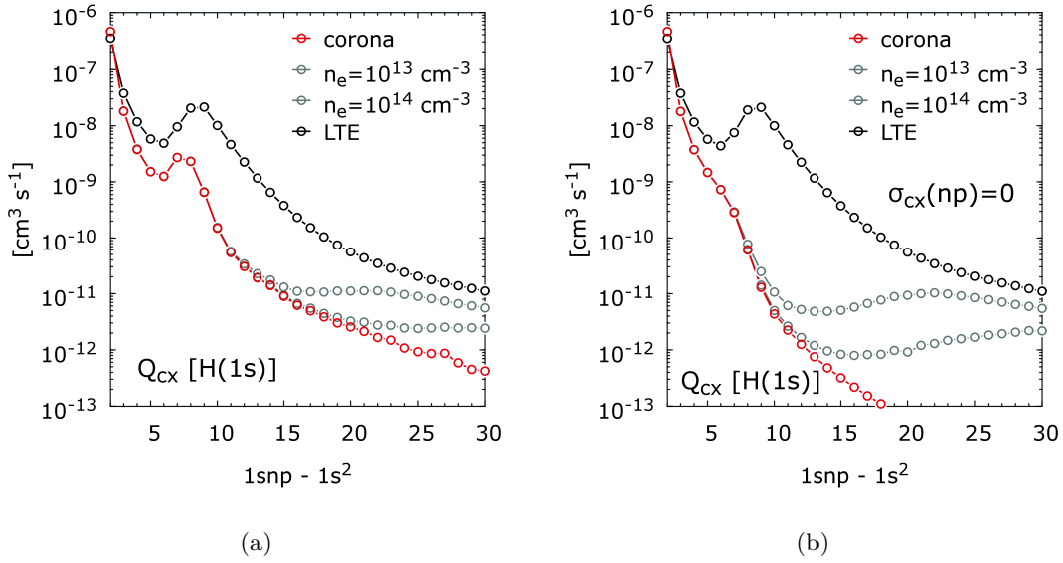


Figure 8.2: **a)** Effective rate coefficients for charge exchange from  $H(1s)$  donor atoms for the Rydberg series of He-like argon. The data is calculated for neutral particle energies according to 8.2. **b)** Effective rate coefficients for charge exchange as shown in (a), but with all  $\sigma_{cx}(np)$  set to zero.

This means, small changes in the  $\sigma_{cx}(np)$  will have strong impact on the characteristics of the effective rate coefficients without significantly changing the  $n$ -cross sections  $\sigma_{cx}(n)$ . To illustrate this, figure 8.2(b) shows the  $Q_{cx}(1snp - 1s^2)$  calculated just as before, but with all  $\sigma_{cx}(np)$  set to zero. In corona limit the  $n$ -resonance around  $n = 8$  disappears, but reappears as soon as collisional redistribution sets in and the  $\sigma_{cx}(n)$  become dominating. This illustrates the high sensitivity of the measured Rydberg lines to the fine-structure resolved CX-cross sections.

**Charge exchange from  $H(2l)$  excited donor atoms** As discussed in section 3.1.1, the charge exchange cross sections crucially depend on the energy state of the donor atoms. While CX from  $H(1s)$  donor atoms mainly influences the Rydberg lines with  $n \leq 15$ , CX from  $H(2l)$  donor atoms is more relevant for higher  $n$ -levels. The resonance in the cross sections occurs here at  $n \approx 20$  (compare figure 8.1(b)). Hence, to describe the charge exchange impact on the high energy tail of the Rydberg series ( $1snp - 1s^2$ ,  $n \rightarrow \infty$ ), contributions from  $H(2l)$  have to be taken into account.

Schultz et al. [10] provide the fine-structure resolved cross sections for charge exchange from  $H(2s)$  and  $H(2p)$  excited donor atoms. Based on this cross section data, the  $Q_{cx}(1snp - 1s^2)$  are calculated in an analogous manner as for  $H(1s)$  donor atoms. The beam energy mix is again given by equation 8.2. Furthermore, the excited beam atoms  $H(2s)$  and  $H(2p)$  are assumed to be populated statistically according to  $(g_l = 2 \cdot l + 1)$ . The results are plotted in figure 8.3(a), showing a similar behavior as in case of  $H(1s)$

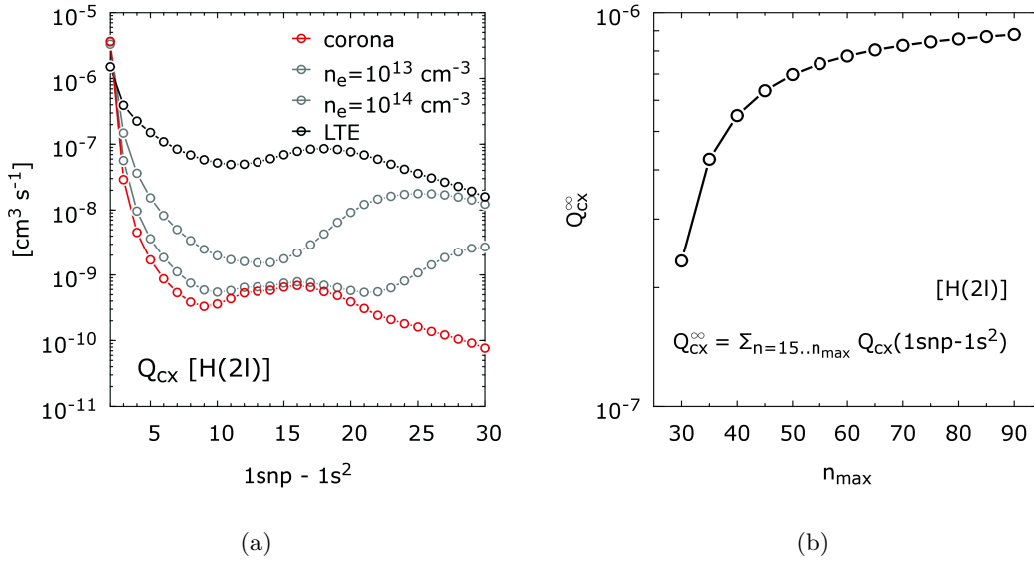


Figure 8.3: **(a)** Effective rate coefficients for charge exchange from  $H(2l)$  donor atoms for the Rydberg series of He-like argon. The data is calculated for neutral particle energies according to equation 8.2 and for statistical distribution of the  $H(2l)$  donor atoms. **(b)** The effective rate coefficient for charge exchange from  $H(2l)$  donor atoms for the high energy tail ( $n \geq 15$ ) of the Rydberg series of He-like argon as a function of the maximal principle quantum number considered in the model. As the CRM is limit to  $n = 30$ , contributions from  $n \geq 31$  are taken into account assuming LTE.

donor atoms. The local maximum due to the  $n$ -resonance in the cross sections is broader than in figure 8.2(a) and occurs around  $n \approx 15$ . In LTE it is shifted towards  $n \approx 20$ . The difference in absolute values of the  $Q_{cx}(1snp-1s^2)$  between the corona and the LTE calculations is slightly bigger than in the case of  $H(1s)$  donor atoms. This is because for  $H(2l)$  donor atoms the ratio  $\sigma_{cx}(np)/\sigma_{cx}(n)$  is smaller, as can be seen from the  $l$ -gradients of the CX-cross sections in figure 8.1.

From figure 8.3(a) it further becomes clear that the limitation of the argon model to  $n_{max} = 30$  might neglect relevant amounts of charge exchange contributions on  $n > 30$ . However, the measured Rydberg spectra do not show relevant line intensities from levels above  $1s30p$  (compare figure 7.6(b) and 7.6(d) on page 86). Therefore, an extension of the model is abandoned.

**Charge exchange from  $H(n > 2)$  excited donor atoms** Different publications [72, 73] propose relevant population densities of the excited beam states with  $n > 2$ . In table 8.1 the population densities of  $H(n)$  given by [73] are listed up to  $n = 10$ . They smoothly decay for  $n < 10$  and then quickly drop off to zero due to field ionization. At the same time, the cross sections for charge exchange from  $H(n)$  excited donor atoms scale with  $n^4$  [17].

$H(n)$	$N_i$ [ $cm^{-3}$ ]	$Q_{cx}^\infty[H(n)]$ [ $cm^3s^{-1}$ ]	$\sum_{m=2}^n \frac{N_m}{N_{1s}} \cdot Q_{cx}^\infty[H(m)]$ [ $cm^3s^{-1}$ ]
2	2.88E-03	2.34E-07	6.76E-10
3	1.21E-03	1.18E-06	2.11E-09
4	5.01E-04	3.74E-06	4.00E-09
5	2.36E-04	9.14E-06	6.17E-09
6	1.19E-04	1.90E-05	8.43E-09
7	5.85E-05	3.51E-05	1.05E-08
8	2.30E-05	5.99E-05	1.19E-08
9	4.93E-06	9.60E-05	1.24E-08
10	1.32E-07	1.46E-04	1.24E-08

Table 8.1: Population of excited beam states according to [73] and estimated  $Q_{cx}^\infty$  for charge exchange from  $H(n)$ . The population densities are calculated for a beam energy of 50 keV, a plasma density of  $n_e = 3 \cdot 10^{13} cm^{-3}$  and a magnetic field of 3 T. The effective rate coefficients for  $H(n > 2)$  were estimated by scaling  $Q_{cx}(1snp - 1s^2)$  for  $H(2)$  donor atoms according to  $\sigma_{cx}[H(n)] \propto n^4$ .

This indicates that for the interpretation of charge exchange effects on the Rydberg series also contributions from  $H(n > 2)$  beam atoms have to be considered. However, detailed cross section data for charge exchange from  $H(n > 2)$  is so far not available. Therefore, the effective rate coefficients for  $H(n > 2)$  donor atoms are estimated by scaling the  $Q_{cx}(1snp - 1s^2)[H(n = 2)]$  with  $n^4$ . This approximation ignores possible changes in the  $nl$ -dependence of the charge exchange cross sections. As in case of  $H(n = 2)$  beam atoms, the contributions are most relevant for the Rydberg tail ( $n \geq 15$ ). We define the effective rate coefficient for charge exchange from  $H(n)$  on the Rydberg tail as:

$$Q_{cx}^\infty[H(n)] = \sum_{k=15.. \infty} Q_{cx}(1skp - 1s^2)[H(n)]. \quad (8.4)$$

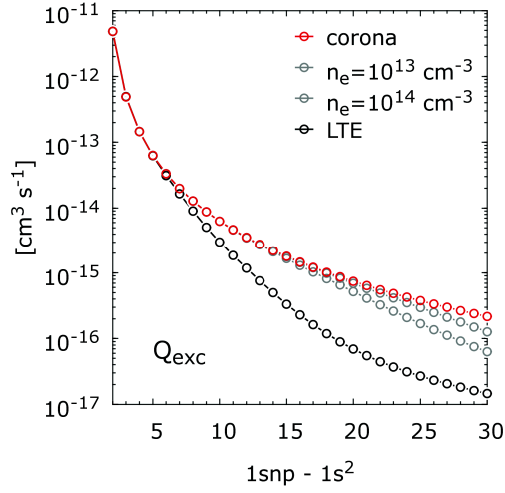
The overall effective rate coefficient for charge exchange from excited donor atoms is then obtained by summarizing equation 8.4 over  $n = 2..10$ :

$$Q_{cx}^\infty[H(n \geq 2)] = \sum_{n=2..10} \frac{N_n}{N_{1s}} \cdot Q_{cx}^\infty[H(n)], \quad (8.5)$$

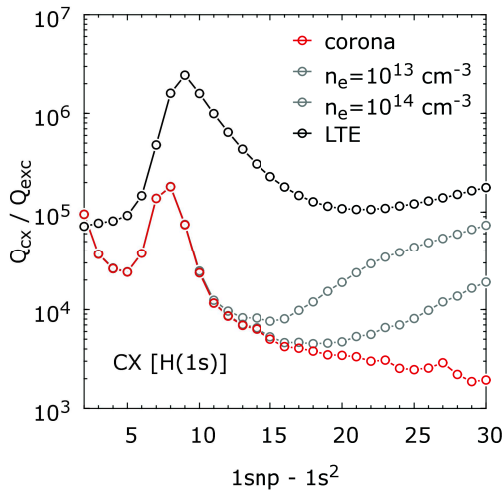
where  $N_n$  and  $N_{1s}$  are the population densities of the  $H(n)$  and  $H(1s)$ , respectively. The weights  $N_n/N_{1s}$  in equation 8.5 allow to handle the excited beam fraction as a whole relative to the ground state density. The results for  $Q_{cx}^\infty[H(n)]$  and  $Q_{cx}^\infty[H(n \geq 2)]$  are listed in table 8.1. The values for  $Q_{cx}^\infty[H(n \geq 2)]$  clearly converge for  $n = 10$ , indicating that no relevant charge exchange contributions will arise from  $H(n > 10)$  beam atoms.

**Excitation from the ground state** The relative enhancement of the Rydberg lines due to charge exchange depends on the ratio of the effective rate coefficients for charge exchange and excitation from the ground state  $Q_{cx}/Q_{exc}$  (compare equation 7.3 on page

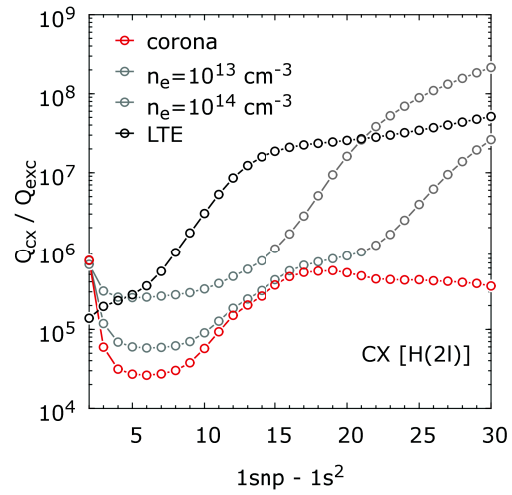
87). Therefore, also the  $Q_{exc}(1snp - 1s^2)$  are required. The results are shown in figure 8.4(a) in the same way as before for charge exchange. Additionally, figure 8.4(b) and 8.4(c) illustrate  $Q_{cx}(1snp - 1s^2)/Q_{exc}(1snp - 1s^2)$  for  $H(1s)$  and  $H(2l)$  donor atoms, respectively.



(a)



(b)



(c)

Figure 8.4: **a)** Effective rate coefficients for excitation from the ground state for the Rydberg series of He-like argon. The data is calculated for an electron temperature of  $T_e = 2 \text{ keV}$ . **b)** Ratio of the effective rate coefficients for charge exchange from  $H(1s)$  donor atoms and excitation from the ground state. **c)** Ratio of the effective rate coefficients for charge exchange from  $H(2l)$  donor atoms and excitation from the ground state.

# Conclusion

This work was intended to further the understanding of the influence of charge exchange recombination on X-ray spectra measured in hot fusion plasmas. The results presented here resolve the long-standing question as to the mechanisms behind the observed line intensity ratios within the radially resolved  $K_\alpha$ -spectra of He-like impurity ions. At the same time, the applied method extends the capabilities of imaging  $K_\alpha$ -spectroscopy. Additionally, the first experimental verification of the partial cross sections for charge exchange at high collision energies was achieved. The analysis of the cross section data contributes to increasing the reliability of impurity density measurements via charge exchange recombination spectroscopy.

The first radial scans of the  $K_\alpha$ -spectrum of He-like argon including the associated satellites were measured at TEXTOR using a new imaging X-ray spectrometer developed for future use at W7-X. The observed line ratios show significant deviations from the corona values that become more pronounced towards the plasma edge. Interpreted in terms of the argon ion ratios, the experimental line ratios correspond to an increase in  $Ar\ XVI / Ar\ XVII$  by up to a factor of five relative to the corona values. The observed argon ion ratio  $Ar\ XVIII / Ar\ XVII$  is increased by up to a factor of one thousand at the outermost lines-of-sight.

The discrepancies between the experimental findings and the corona model could be explained quantitatively on the basis of charge exchange with the neutral particle background and radial impurity transport. Both argon ion ratios could be reproduced consistently over the entire radial field of view within a 1D transport model of the argon ionization balance in TEXTOR. In an iterative procedure, self-consistency between the modeled ion balance and the interpretation of the sight-line-integrated spectra was achieved.

The  $K_\alpha$ -spectra allow a clear separation of charge exchange and impurity transport effects, so that radial profiles of the neutral particle density  $n_0(r)$  and the diffusion coefficient  $D_\perp(r)$  can be derived. Within the accuracy the measured  $n_0$ -profiles agree well with modeled  $n_0$ -profile shapes from Monte Carlo (EIRENE) and diffusion (RITM) codes. Moreover, the absolute neutral particle densities are consistent with earlier results from LIF measurements at the plasma edge of TEXTOR.

Impurity transport is found to be the main mechanism behind the strong deviations from the corona values. The deduced time averaged diffusion coefficients  $D_\perp(r)$  have clearly anomalous values and show a sharply bounded region of high diffusivity for  $15\text{ cm} \leq r \leq 30\text{ cm}$ , where  $D_\perp$  reaches up to  $5\text{ m}^2/\text{s}$ . The obtained  $D_\perp(r)$  are in very good agreement with results from earlier experiments at TEXTOR that were based on the temporal evolution of signals emitted from different argon ion stages. The con-

sistency between the diffusion coefficients independently obtained from temporal and spatial information is evidence for the correct interpretation of the data.

Furthermore, the central values for the argon ion ratio  $Ar\text{ XVIII} / Ar\text{ XVII}$  could be confirmed independently using the Rydberg series of He-like argon ( $1snp - 1s^2$ ) and the  $4p - 1s$ -transition in H-like argon.

$K_\alpha$ -spectroscopy on mid  $z$  impurity elements is an established diagnostic for plasma temperature and velocity measurements. The results presented here confirm that  $K_\alpha$  imaging is also a suitable diagnostic for neutral particle density and impurity transport behavior in controlled fusion plasmas. Radial profiles of  $T_e$ ,  $T_i$ ,  $v_p$ ,  $n_0$  and  $D_\perp$  can be measured simultaneously.

In order to refine the method for future applications several improvements can be made. First of all a continuous monitoring of the entire radial emission profile - as for example realized at ALCATOR - is highly recommended. This will significantly increase the accuracy of the results for  $D_\perp(r)$  and  $n_0(r)$ . Apart from this, the method discussed here has to date only been applied to  $K_\alpha$ -spectra measured in ohmic discharges. For evaluation of neutral beam heated discharges a distinction between the thermal background neutrals and the fast beam neutrals should be included in the model. Finally, with respect to future impurity transport studies, an uncoupled consideration of the convective and the diffusive components is recommended to fully exploit the capabilities of  $K_\alpha$ -imaging spectroscopy.

The influence of charge exchange recombination with high energetic neutral particles on the Rydberg series of He-like argon was investigated. With the aid of the unique diagnostic opportunities at TEXTOR, the X-ray spectra of argon could be observed under the direct influence of a 50 keV neutral heating beam. The observed charge exchange impact on the Rydberg series shows a maximum around  $n = 8, 9$  - in good agreement with theoretical predictions. For a quantitative analysis the effective rate coefficients for charge exchange on the Rydberg series were calculated using the CX cross sections of Schultz et al. [9, 10] and the collisional radiative model NOMAD [74]. Based on these effective rate coefficients the CX-impact on the Rydberg lines could be described accurately at low plasma density. Both the absolute values as well as the dependence on the principle quantum number  $n$  could be reproduced. This represents the first experimental verification of the fine structure resolved cross sections for charge exchange at high, CXRS-relevant collision energies. The good agreement with the experiment gives high confidence in the theoretical data.

The strong CX-impact on the high Rydberg tail ( $1snp - 1s^2$ ,  $n \geq 15$ ) could clearly be assigned to charge exchange contributions from excited beam atoms. The fraction of excited beam atoms needed to describe the experimental observations is in good agreement with predictions made by recent beam population models.

The behavior of the CX-impact at higher plasma densities is not fully understood and is subject of future investigations, while a detailed analysis will require fine-structure resolved cross sections for charge exchange from highly excited beam atoms.

Finally, the electron and ion temperature profiles were derived from the radially resolved

$K_\alpha$ -spectra measured during ohmic and neutral beam heated discharges. The obtained  $T_e(r)$  agree very well with the profile shapes given by the ECE diagnostic. However, a constant offset of ca. +200 eV compared to the ECE data is observed. The reason for this discrepancy remains unresolved and is subject of future investigations. For the first time the new imaging X-ray spectrometer allowed measurement of radial ion temperature profiles in the plasma core region of TEXTOR during ohmic discharges. The obtained  $T_i(r)$  are consistent with results from CXRS measurements that were previously performed at the plasma boundary of TEXTOR. In ohmic discharges the  $T_i(r)$  are found to be proportional to the electron density  $n_e(r)$ .

# Danksagung

Zunächst danke ich Herrn Prof. Dr. Detlev Reiter und Herrn Prof. Dr. Georg Pretzler für die Begutachtung meiner Dissertation und ihre Unterstützung im Vorfeld.

Besonderer Dank gilt Dr. Oleksandre Marchuk für seine engagierte Betreuung, seine ständige Gesprächsbereitschaft und die zahllosen hilfreichen Diskussionen während meiner Zeit in Jülich.

Darüber hinaus danke ich Dr. Günter Bertschinger und Hubert Jägers für ihre Hilfe bei den Mess- und Kalibrierungsarbeiten.

Für Unterstützung verschiedenster Art bedanke ich mich außerdem bei Jochen Assmann, Dr. Wolfgang Biel, Petra Börner, Dr. Sebastijan Bredsinsek, Dr. Rémy Guirlet, Marlene Hoffmann, Dr. Hans-Rudolf Koslowski, Prof. Dr. Christian Linsmeier, Prof. Dr. Ulrich Samm, Judith Schönbrenner und natürlich dem TEXTOR-Team.

Nicht zuletzt danke ich meiner Freundin Katharina und meiner Familie für ihre Unterstützung während der letzten Jahre.

# Bibliography

- [1] T. Krakor, Untersuchungen der radialen Verteilung der leichten Verunreinigung Neon im Kern von TEXTOR-94 mittels röntgenspektroskopischer Methoden, PhD thesis, Ruhr-Universität Bochum, 1998.
- [2] J. Wesson, Tokamaks, Third ed. (Clarendon Press, Oxford, 2004).
- [3] H. Kunze, Introduction to Plasma Spectroscopy, First ed. (Springer, 2009).
- [4] I. Sobel'man, L. Vainshtein and E. Yukov, Excitation of Atoms and Broadening of Spectral Lines, Second ed. (Springer, 1995).
- [5] T. Fujimoto, Plasma Spectroscopy, First ed. (Oxford University Press, 2004).
- [6] H. Griem, Plasma spectroscopy, First ed. (McGraw-Hill, New York, 1964).
- [7] A. Pradhant and M. Seaton, *J. Phys. B: At. Mol. Phys.* 18 (1985) 1631.
- [8] A. Gabriel and C. Jordan, *Nature* 221 (1969) 947.
- [9] D. Schultz, T.G. Lee and S. Loch, *J. Phys. B: At. Mol. Opt. Phys.* 43 (2010) 11.
- [10] Atomic data for fusion, <http://www-cfadc.phy.ornl.gov>.
- [11] L. Errea et al., *J. Phys. B: At. Mol. Opt. Phys.* 39 (2006) 91.
- [12] O. Marchuk, Modeling of He-like spectra measured at the tokamaks TEXTOR and TORE SUPRA, PhD thesis, Ruhr-Universität Bochum, 2004.
- [13] M. Gu, *Can. J. Phys.* 86 (2008) 675.
- [14] N. Badnell, Autostructure-code.
- [15] H.v. Regemorter, *Astrophys. J.* 132 (1962) 906.
- [16] S. Younger and W. Wiese, *J. Quant. Spectrosc. Radiat. Transfer* 22 (1979) 161.
- [17] R. Janev and J. Smith, Atomic data plasma-material interaction data for fusion (International Atomic Energy Agency, Vienna, 1993).
- [18] D. Sampson, *J. Phys. B: At. Mol. Opt. Phys.* 10, 4 (1977) 749.
- [19] H. Griem, *Phys. Rev.* 131, 3 (1963) 1170.
- [20] T. Fujimoto and M.R.W. P., *Phys. Rev. A* 42, 11 (1990) 6588.

- [21] T. Schlummer, Effektive Ratenkoeffizienten für die Ladungsaustauschspektroskopie an H-ähnlichem Argon, Master's thesis, Universität zu Köln, 2010.
- [22] M. Tokar, Plasma Phys. Control. Fusion 36 (1994) 1819.
- [23] R. Guirlet et al., 33rd EPS Conf. on Contr. Fusion and Plasma Physics (2006).
- [24] R. Guirlet et al., Plasma Phys. Control. Fusion 48 (2006) 63.
- [25] J. Freidberg, Plasma Physics and Fusion Energy, First ed. (Cambridge University Press, 2007).
- [26] G. Giannella et al., Nucl. Fusion 34 (1994) 1185.
- [27] M. Mattioli et al., Nucl. Fusion 38 (1998) 189.
- [28] M. Mattioli, C. De Michelis and P. A.L., Nucl. Fusion 38, 11 (1998) 1629.
- [29] M. Puiatti et al., Phys. Plasmas 13 (2006) 042501.
- [30] W. Biel et al., 26th EPS Conf. on Contr. Fusion and Plasma Physics 23 J (1999) 657.
- [31] W. Biel et al., 28th EPS Conf. on Contr. Fusion and Plasma Physics 25 A (2001) 1389.
- [32] Y. Liang et al., Phys. Plasmas 9 (2002) 4179.
- [33] H. Takenaga et al., Nucl. Fusion 43 (2003) 1235.
- [34] A. Hedqvist et al., J. Phys. B: At. Mol. Opt. Phys. 33 (2000) 375.
- [35] M. Bitter et al., Phys. Rev. Lett. 43 (1979) 129.
- [36] T. Group, J. Dubau and M. Loulergue, J. Phys. B: At. Mol. Phys. 15 (1981) 1007.
- [37] P. Platz et al., Rev. Sci. Instrum. 70 (1999) 308.
- [38] G. Bertschinger et al., Phys. Scr. T83 (1999) 132.
- [39] G. Bertschinger and O. Marchuk, Nuclear Fusion Research, Understanding Plasma-Surface Interaction: High-temperature plasma diagnostics by X-ray Spectroscopy in the low density limit (Springer, 2004).
- [40] J. Rice et al., Phys. Rev. A: At., Mol., Opt. Phys. 35, 7 (1987) 3033 .
- [41] A. Urnov, J. Phys. B: At. Mol. Opt. Phys. 28 (1995) 1.
- [42] A. Ince-Cushman et al., Rev. Sci. Instrum. 79 (2008).
- [43] T. Schlummer et al., 40th EPS Conf. on Contr. Fusion and Plasma Physics (2013).

- [44] A.H. Gabriel, *Mon. Not. R. astr. Soc.* 160 (1972) 99.
- [45] F. Bely-Dubau et al., *Mon. Not. R. astr. Soc.* 198 (1982) 239.
- [46] O. Marchuk, private communications.
- [47] F. Rosmej et al., *Plasma Phys. Control. Fusion* 41 (1999) 191.
- [48] O. Neubauer et al., *Fusion Science and Technology* 47 (2005) 76.
- [49] O. Neubauer, Internal report, Institute for Energy and Climate Research, Plasma Physics, Forschungszentrum Jülich.
- [50] M. Bitter et al., *J. Phys. B: At. Mol. Opt. Phys.* 43 (2010) 144011.
- [51] M. Bitter et al., *Rev. Sci. Instrum.* 66 (1995) 530.
- [52] M. Bitter et al., *Rev. Sci. Instrum.* 70 (1999) 292.
- [53] S. Stepanov, <http://sergey.gmca.aps.anl.gov>.
- [54] J. Weinheimer et al., *Rev. Sci. Instrum.* 72, 6 (2001) 2566.
- [55] G. Bertschinger et al., *Rev. Sci. Instrum.* 75, 10 (2004) 3727.
- [56] G. Bertschinger, private communications.
- [57] E. Le Bigot et al., *Phys. Scr.* 134 (2009) 014015.
- [58] T. Kato et al., *Phys. Rev. A* 44 (1991) 6776.
- [59] O. Marchuk et al., *Plasma Phys. Contr. Fusion* 48 (2004) 1633.
- [60] O. Marchuk and M. Tokar, *Contrib. Plasma Phys.* 48 (2008) 194.
- [61] G. Hogewey et al., *Nucl. Fusion* 38 (1998) 1881.
- [62] H. Koslowski, private communications.
- [63] P. Mertens and M. Silz, *J. Nucl. Mater.* 241-243 (1997) 842.
- [64] D. Reiter, *Journal of Nuclear Materials* 196-198 (1992) 80.
- [65] I. Beniaminy and M. Deutsch, *Comput. Phys. Commun.* 27 (1982) 415.
- [66] A. Kappatou et al., *Rev. Sci. Instrum.* 83 (2012) 10D519.
- [67] R. Uhlemann and J. Ongena, *Fusion Techol.* 35 (1999) 42.
- [68] R. Schorn et al., *Nucl. Fusion* 32 (1992) 351.
- [69] A. Donné et al., *Fusion Sci. Technol.* 47 (2005) 220.

- [70] M. von Hellermann et al., 29th EPS Conf. on Contr. Fusion and Plasma Physics (2002).
- [71] O. Marchuk et al., AIP Conf. Proc. Vol. 1545 (1), 2013.
- [72] I. Bespamyatnov, Nucl. Fusion 53 (2013) 123010.
- [73] O. Marchuk, Y. Ralchenko and D. Schultz, Plasma Phys. Control. Fusion 54 (2012) 095010.
- [74] Y. Ralchenko and Y. Maron, J. of Quant. Spec. & Rad. Transf. 71 (2001) 609.
- [75] O. Marchuk et al., J. Phys. B: At. Mol. Opt. Phys. 42 (2009) 165701.
- [76] M. Seaton, Proc. Phys. Soc. 79 (1962) 1105.
- [77] M. Lennon et al., J. Phys. Chem. Ref. Data 17 (1988) 1285.